

Interannual to Decadal Sea-Level Variability in the Indo-Pacific Region:

Development and Application of a High-Resolution Ocean Model

Dissertation for the degree Doctor of Natural Sciences

submitted by

Patrick Wagner

Christian-Albrechts-Universität zu Kiel

Faculty of Mathematics and Natural Sciences

Kiel, 2021

1. *Reviewer* Prof. Dr. Claus W. Böning

2. *Reviewer* Prof. Dr. Martin Visbeck

Supervisors Prof. Dr. Claus W. Böning
 Prof. Dr. Arne Biastoch
 Dr. Johannes Karstensen

Patrick Wagner

Interannual to Decadal Sea-Level Variability in the Indo-Pacific Region: Development and Application of a High-Resolution Ocean Model

Dissertation for the degree Doctor of Natural Sciences, September 2021

Christian-Albrechts-Universität zu Kiel

Faculty of Mathematics and Natural Sciences

Christian-Albrechts-Platz 4

24118 Kiel

Date of submission: 21 September 2021

Date of oral exam: 10 November 2021

Approved for publication: 10 November 2021

Abstract

Strong sea-level trends that exceeded the global mean signal several times over, have been observed in the western parts of the tropical Pacific between the early 1990s and early 2010s. These trends can be attributed to decadal and multidecadal variability and are mainly due to steric variations driven by wind-stress anomalies. This doctoral thesis aims to broaden our knowledge about these trends. Specifically, the role of ocean–atmosphere heat and freshwater fluxes and the linkage between sea-level variability in the western tropical Pacific and the densely populated region of the Australasian Mediterranean Sea (AMS) is investigated. These issues are addressed using a framework of ocean-sea-ice models that includes a newly developed high-resolution configuration named NUSA20 to resolve the fine-scale bathymetry of the AMS. To facilitate sensitivity experiments where the realistic atmospheric forcing is replaced by a repeated annual cycle, the recently introduced repeated-year-forcing approach (RYF) is evaluated. Three RYF-experiments using different annual cycles are conducted. Although the specific choice might be subject to the research question, it is shown that the experiments based on the periods from 1st May to 1st April of the years 1984/85 and 1990/91 show only minor differences and are able to characterize the model drift and transients of the hindcast simulation. Using a series of sensitivity experiments to disentangle the impacts of momentum fluxes on one side and heat and freshwater fluxes on the other side on sea-level variability, it is shown that anomalous buoyancy fluxes amplify interannual sea-level variability in the eastern tropical Pacific and that both heat and freshwater flux anomalies trigger westward propagating sea-level anomalies in the central Pacific that dampen variability on interannual and decadal timescales in the western part of the basin. In the AMS decadal fluctuations of the large-scale climate modes of the Pacific are found to account the majority of the low-frequency sea-level variability in almost all deep basins of the region. Intrinsic variability is negligible except in the South China Sea, where it accounts for up to 25 % of the total decadal sea-level variability. Overall, this thesis provides an assessment and a practical application of the RYF-approach. Building on sensitivity experiments, corresponding reference simulations and a high-resolution configuration the importance of ocean–atmosphere buoyancy fluxes for sea-level variability and the close dependence of decadal sea-level variability in the AMS on low-frequency fluctuations of Pacific climate modes is demonstrated.

Zusammenfassung

Im westlichen tropischen Pazifik konnte zwischen den frühen neunziger und frühen zehner Jahren ein Anstieg des Meeresspiegels beobachtet werden, der den globalen Mittelwert um ein vielfaches übertraf. Dieser Anstieg ist Teil der dekadischen bis multi-dekadischen Variabilität und hauptsächlich auf sterische Anomalien, verursacht durch eine geänderte Windschubspannung, zurückzuführen. Die vorliegende Dissertation soll unser Verständnis dieser Trends erweitern. Insbesondere soll untersucht werden, welche Rolle Wärme- und Frischwasserflüsse zwischen Ozean und Atmosphäre spielen. Auch soll der Zusammenhang zwischen Meeresspiegelschwankungen im westlichen tropischen Pazifik und im Australasiatischen Mittelmeer betrachtet werden. Dazu werden eine Reihe von Ozean-Meereis-Modellen genutzt, darunter die neu entwickelte, hochaufgelöste Konfiguration NUSA20. Um Sensitivitätsstudien zu ermöglichen, in denen der realistische, atmosphärische Antrieb durch einen gleichbleibenden, sich wiederholenden Jahresgang ersetzt wird, wird zunächst die sogenannte "repeated-year-forcing" Methodik (RYF) evaluiert. Drei verschiedene RYF-Experimente werden herangezogen. Die Wahl eines spezifischen Jahres kann letztlich von der wissenschaftlichen Fragestellung abhängig sein. Allerdings weisen die Experimente, die auf den Perioden zwischen dem 1. Mai und dem 1. April der Jahre 1984/85 und 1990/91 basieren, nur geringe Unterschiede auf und sind geeignet, die Modelldriften und initialen Anpassungsprozesse des Referenzexperiments abzubilden. Basierend auf einer Reihe von Sensitivitätsstudien wird weiterhin dargestellt, wie im östlichen Teil des tropischen Pazifiks die zwischenjährliche Variabilität des Meeresspiegels durch Wärme flüsse verstärkt wird. Im westlichen Teil dagegen werden durch Impulsflüsse erzeugte Abweichungen des Meeresspiegels durch Wärme- und Frischwasserflüsse gedämpft, indem diese im zentralen tropischen Pazifik westwärts propagierende Meeresspiegelanomalien auslösen. Im Australasiatischen Mittelmeer ist ein Großteil der dekadischen Meeresspiegelvariabilität auf tieffrequente Änderung der relevanten, großskaligen Klimamoden des Pazifiks zurückzuführen. Intrinsische Variabilität ist, außer im Südchinesischen Meer, vernachlässigbar. Dort ist sie jedoch für bis zu 25 % der Variabilität verantwortlich. Die vorliegende Arbeit präsentiert eine spezifische Bewertung sowie eine praktische Anwendung der RYF-Methodik. Basierend auf Sensitivitätsstudien, Referenzexperimenten und einer hochaufgelösten Modellkonfiguration kann die Bedeutung von Wärme- und Frischwasserflüssen zwischen Ozean und Atmosphäre für Änderungen des Meeresspiegels im tropischen Pazifik gezeigt werden. Darüber hinaus zeigen die Ergebnisse die große Bedeutung tieffrequenter Zyklen der pazifischen Klimamoden für dekadischen Änderungen des Meeresspiegels im Australasiatischen Mittelmeer.

Contents

1	Introduction	1
1.1	Sea level	1
1.1.1	Global mean sea level	2
1.1.2	Regional sea level	2
1.1.3	Regional sea level in the tropical Pacific	4
1.1.4	Measuring sea level	8
1.1.5	Diagnosing sea level	11
1.2	Turbulent energy fluxes in ocean models	13
1.3	The importance of atmospheric forcing for sea-level studies with ocean models	15
1.4	Aims and structure of this thesis	17
2	Methods: Ocean General Circulation Models	19
2.1	Model design	19
2.2	OGCM experiments	22
2.3	Model validation	25
2.3.1	Sea surface height	25
2.3.2	Western tropical Pacific stratification	30
2.3.3	Makassar Strait	31
3	Assessment of a repeated year forcing	39
3.1	Abstract	39
3.2	Introduction	40
3.3	Ocean models	45
3.4	Results	45
3.4.1	Atlantic Meridional Overturning Circulation	52
3.4.2	Antarctic Circumpolar Current	52
3.4.3	Indonesian Throughflow	56
3.5	Estimation of spurious trends in hindcast experiments	59
3.6	Summary and conclusion	60
3.6.1	Recommendation for a single RYF-period	62

3.6.2	Future RYF-experiments	63
4	Contribution of buoyancy fluxes to tropical Pacific sea-level variability	65
4.1	Abstract	65
4.2	Introduction	66
4.3	Model experiments	68
4.4	Results	71
4.5	Case study – 1997/98 El Niño	78
4.6	Summary and conclusion	81
5	Decadal sea-level variability in the Australasian Mediterranean Sea	85
5.1	Abstract	85
5.2	Introduction	86
5.3	Methods	90
5.3.1	Ocean general circulation model experiments	90
5.3.2	Observational datasets	92
5.3.3	Steric sea level	92
5.4	Results	93
5.4.1	Impact of buoyancy fluxes on SSH	93
5.4.2	Linear regression of SSH on ENSO and PDO indices	96
5.4.3	Decomposition of SSH variability into thermosteric and halosteric contributions	99
5.5	Summary and conclusion	104
5.5.1	Summary	104
5.5.2	Discussion	106
6	Summary and conclusion	109
6.1	Open questions	111
6.1.1	Small-scale limit of sensitivity experiments	111
6.1.2	Effect of different El Niño types on tropical Pacific sea level	112
6.1.3	The mechanism behind the ITF transport reduction	112
	Bibliography	115
A	Appendix Chapter 3	133
B	Appendix Chapter 5	135
	Erklärung	139

Introduction

This thesis investigates regional sea-level variability in the tropical Pacific and the adjacent Australasian Mediterranean Sea (AMS) that connects the Pacific and the Indian Ocean. Sea-level trends that exceeded the global mean signal several times over have been observed in the western parts of the tropical Pacific since the early 90s. These trends can be considered the main motivation for this thesis. The aim of the studies compiled here is to further our understanding of the variability in the region and shed light on the driving mechanism by developing and using state-of-the-art modelling tools. This first chapter gives an introduction into the variability of sea level from an oceanographic perspective. The mechanism that determine its variability in general and in the tropical Pacific specifically are discussed. A brief introduction about measuring and diagnosing sea level and regarding the challenges in modeling is also provided.

1.1 Sea level

Sea level describes the height of the ocean surface and is either given relative to the surface of the solid earth (relative sea level), which can change either due to actual sea-level variability or due to vertical displacement of the solid earth, or as "absolute" sea level relative to a fixed frame of reference. Both can differ substantially at a single location. The former is highly relevant to local stakeholders, but only the latter is directly linked to the thermodynamic properties and geostrophic currents of the ocean and therefore of interest in oceanography. Sea level is affected by a wide range of processes driving variability on timescales from seconds to millennia. This thesis focuses on processes that are relevant for contemporary sea-level changes on interannual to multi-decadal timescales.

1.1.1 Global mean sea level

Absolute sea-level change always expresses a change in the volume of the underlying water column and it is common practice to separate this change into density and mass-related effects as they are often dominated by different forcing mechanism. The volume of seawater increases with decreasing density and vice versa and this effect causes so-called steric sea-level anomalies. Because the density of seawater is a function of temperature, salinity and pressure, changes of the oceans' total heat and freshwater content affect the steric part of the global mean sea level (GMSL). With respect to observed GMSL, steric changes during the last century are almost exclusively driven by an oceanic uptake of atmospheric heat. Thermal expansion currently contributes about 1 mm yr^{-1} to the GMSL rise (Stocker et al., 2013).

The total mass of the oceans can change due to redistribution of water between the ocean, the atmosphere, the terrestrial hydrosphere and the cryosphere. The melting of land ice in Greenland and Antarctica and of glaciers are dominant contributors to the observed changes, while contributions from land-water storage changes are smaller but not negligible (Stocker et al., 2013). The addition of fresh water does also modify the oceans' density, however in the context of GMSL rise, this effect is negligible (Stocker et al., 2013).

Overall, between 1993 and 2010, a GMSL trend of 3.2 mm yr^{-1} has been observed. This trend is dominated by mass changes that contribute about 2/3, while thermal expansion accounts for the remaining third (Stocker et al., 2013). Although the linear increase is the dominate signal of the GMSL timeseries, it also includes significant variability on interannual to decadal timescales. This variability is highly correlated with El Niño-Southern Oscillation (ENSO; Nerem et al. 2010), as the changes in the terrestrial water cycle associated with ENSO affect the ocean's mass balance (Llovel et al., 2011; Cazenave et al., 2012).

1.1.2 Regional sea level

Regional sea-level variability is affected by more processes than GMSL and is highly non-uniform (e.g. Stammer et al., 2013). Consequently, local sea-level trends can deviate substantially from the GMSL rise. In particular, redistribution of mass and density anomalies due to ocean dynamics shape the regional pattern of sea-level variability (e.g. Zanna et al., 2019). In many cases, these regional effects are driven by changes of the wind fields that determine sea-level patterns through Ekman

pumping, waves dynamics or coastal upwelling. As the large-scale changes of the wind field are often linked to natural climate modes like the North Atlantic Oscillation (NAO), the Pacific Decadal Oscillation (PDO) or ENSO, so is regional sea-level variability (Han et al., 2017).

Similar to the GMSL, regional sea-level changes can be separated into changes of the total mass of the water column and steric signals due to density changes. Since the barotropic adjustment redistributes local mass anomalies around the globe in a matter of days (Greatbatch, 1994; Lorbacher et al., 2012), regional pattern of mass changes are mostly due to changes of the earth gravitational field. For example, as the gravitational pull of land ice is reduced due to its loss of mass, sea level tends to drop close to the poles but rises at the equator (e.g. Mitrovica et al., 2001; Milne et al., 2009). However, this effect is small in comparison with steric changes, which account for a large fraction of regional sea-level changes (Carton et al., 2005; Köhl and Stammer, 2008; Forget and Ponte, 2015; Stammer et al., 2013). These steric changes are primarily due to heat content changes, but halosteric sea-level anomalies can be important regionally, for example in the Arctic, the North Atlantic, the Bay of Bengal or the southwestern tropical Pacific (Köhl and Stammer, 2008; Lombard et al., 2009; Forget and Ponte, 2015). Because steric sea-level changes depend on the vertical extent of the water column that is able to expand, the signal is reduced as the water depth decreases. This can introduce across-slope sea-level gradients that in turn can drive mass exchanges between the shelf region and the deep ocean making mass effects non-negligible on a local scale (e.g. Bingham and Hughes, 2012).

Surface fluxes of heat and fresh water have an impact on the local ocean density and can therefore produce steric sea-level anomalies. However, the importance of these buoyancy fluxes is not yet fully determined. Only few publications quantify their impact from a global perspective (e.g. Piecuch and Ponte, 2011; Forget and Ponte, 2015; Meyssignac et al., 2017), but in conjunction with regional studies (Piecuch and Ponte, 2012; Fukumori and Wang, 2013; Piecuch et al., 2019), the tropical Pacific emerged as one of very few regions, where buoyancy fluxes are an important driver of sea-level variability. This is the subject of chapter 4.

The response of the ocean to atmospheric loading contributes another source of variability. On timescales of a few days, the ocean adjusts to surface pressure anomalies according to the inverted barometer effect. A sea-level pressure anomaly of

1 hPa changes the local sea level by 10 mm. On interannual timescales, associated variability ranges from 0.5 cm in the tropics to 3 cm at high latitudes (Ponte, 2006).

In addition to the aforementioned effects, relative sea level includes changes resulting from vertical land motion. The effect is small in most coastal areas but can be a relevant process in some regions. For example, areas that were covered by continental ice during the last Ice Age are still affected by glacial isostatic adjustment (GIA), i.e. the earth crust rebounds after the collapse of the ice sheets (see Tamisiea, 2011 for a discussion from an oceanographic perspective). The Gulf of Bothnia, for example, does still uplift with up to 10 mm yr^{-1} (Lidberg et al., 2007), causing negative sea-level trends that easily compensate the GMSL rise. Vertical land motion may also be non-GIA-related. Relevant processes include tectonic motion on very long timescales (e.g. Hammond et al., 2018) or seismic events (e.g. Smith-Konter et al., 2014). Relative sea level in Jakarta, Indonesia rose with 23.1 mm yr^{-1} between 1993 and 2009 due to land subsidence as a consequence of groundwater extraction (Fenoglio-Marc et al., 2012), rendering the rates of GMSL rise negligible. Most river deltas are also affected by vertical land motion. Groundwater and oil extraction that causes sediment compaction and reduced aggradation often results in subsidence that exceeds the global mean sea-level rise rates (Syvitski et al., 2009). Apart from very localized effects, vertical land motion is negligible in the region that is of interest in this thesis. On the temporal and spatial scales considered here, sea-level variability is instead dominated by absolute changes. For the rest of this thesis, sea-level changes will therefore always refer to absolute sea-level changes.

1.1.3 Regional sea level in the tropical Pacific

Sea-level trends of up to 10 mm yr^{-1} were observed in the western tropical Pacific over the last three decades. Because these trends exceeded the global mean rates by a factor three and had severe consequences for the population of the low-lying islands in the region, they received a lot of attention from the scientific community (e.g. Timmermann et al., 2010; Merrifield, 2011; Merrifield and Maltrud, 2011; McGregor et al., 2012a; Merrifield et al., 2012; Moon and Song, 2013; Moon et al., 2013; Qiu and Chen, 2012). The fundamental mechanisms that drive these trends are understood. Nevertheless, open questions remain and two of them will be discussed in this thesis. Namely, the importance of heat and freshwater fluxes for sea-level variability (chapter 4) and the impact of low-frequency sea-level variability in the Pacific on the adjacent region of the AMS (chapter 5). The following section

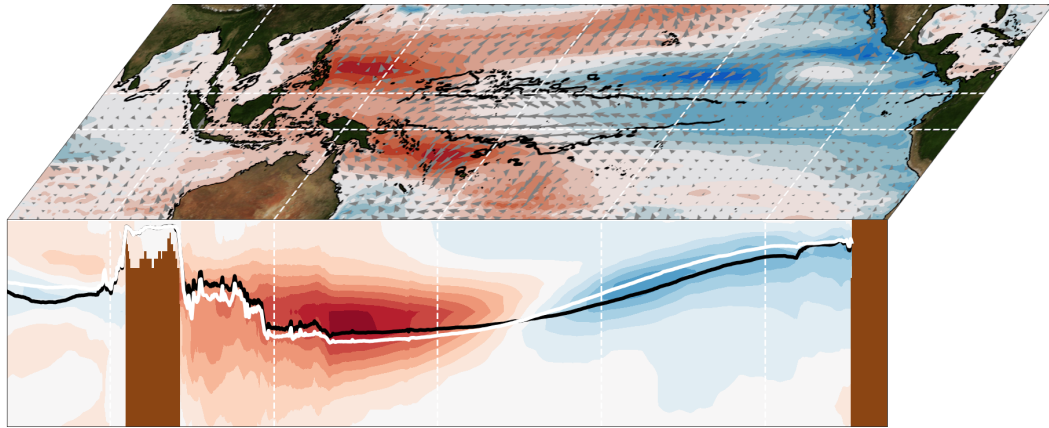


Fig. 1.1.: Sea-level changes in the tropical Pacific between 1990 and 2009 from the global ocean model configuration HC-JRA introduced in section 2. Map: trends of sea-level (shading; red/blue indicates positive/negative trends between $\pm 10 \text{ cm year}^{-1}$) and wind stress (arrows). The black contours indicate regions with strong increases in Ekman pumping velocities ($10^{-7} \text{ m s}^{-1} \text{ year}^{-1}$). Section (averaged over 5°S – 5°N ; marked by zonal, dashed lines): temperature trends (shading; red/blue indicates positive/negative trends between $\pm 0.2 \text{ K year}^{-1}$) and thermocline depth (thick contours) over the periods 1990 to 1993 (black contour) and 2007 to 2009 (white contour).

therefore provides a brief introduction into the mechanisms that shape the variability in the region.

The tropical Pacific is characterized by the trade wind regime, where easterlies from both hemispheres converge on the equator to form the "Intertropical Convergence Zone" (ITCZ). Sea-level variability is closely linked to variability of this wind field on interannual (Delcroix, 1998; Forget and Ponte, 2015; Han et al., 2017) to decadal timescales (Timmermann et al., 2010; Merrifield, 2011; Merrifield and Maltrud, 2011; McGregor et al., 2012a; Merrifield et al., 2012; Moon and Song, 2013; Moon et al., 2013; Qiu and Chen, 2012; Han et al., 2017) and on first order, sea-level anomalies can be understood as an adiabatic advection (Piecuch and Ponte, 2011). Westward wind anomalies pile up warm surface waters in the western tropical Pacific and thereby deepen the thermocline in the west and shoal it in the east. This leads to a very distinct spatial pattern, where the western and central to eastern parts of the equatorial basin show opposing tendencies. To illustrate this effect, Fig. 1.1 shows sea-level trends over the period 1990 to 2009.

As detailed in Lu et al. (2013), two mechanisms are important, by which wind-stress anomalies drive sea-level changes. Sea-level anomalies are a response to anomalous wind-stress curl that drives Ekman pumping or suction and thereby deepens or shoals

the thermocline and produces corresponding sea-level anomalies. In addition to sea-level trends, Fig. 1.1 shows linear wind-stress trends and indicates regions where Ekman pumping velocities increased the most. Subsurface temperature anomalies and the corresponding deepening of the thermocline are well pronounced. However, it is also apparent that areas of increased Ekman pumping are not perfectly aligned with spatial patterns of sea-level trends. Instead, as a second mechanism, wind-stress anomalies also trigger baroclinic Rossby waves that propagate westward along the equator and also drive thermocline-depth variations and sea-level anomalies (Lu et al., 2013). A series of studies using shallow water models showed that in particular the first two baroclinic mode Rossby waves are able to reproduce the observed pattern as a response to low-frequency wind-forcing (Clarke, 2010; Zhu et al., 2017; Greatbatch et al., 2018). Clarke (2010) coined the term "Tilt-mode" for the dominate mode, which describes a balance between zonal wind-stress forcing and the pressure gradient due to the sloping thermocline and which is able to reproduce the distinct zonal-dipole pattern.

As already mentioned above, ocean–atmosphere heat and freshwater fluxes can also contribute to regional sea level in the region. However, a detailed picture, in particular regarding decadal variability, is currently missing as existing studies focus on the altimetry era. The relative importance of freshwater fluxes and heat fluxes, remains also unclear. Chapter 4 aims to elucidate this issue.

Strong sea-level trends in the western tropical Pacific prompt the question if similar trends are to be expected for the adjacent and highly populated area of the AMS. This is of particular relevance because the area forms a connection between the Pacific and the Indian Ocean, through which anomalies from both basins may reach the region. This is the subject of chapter 5 and a detailed introduction is given there. The unique feature of the region, a low-latitude connection of two oceans, shall be introduced in the next paragraph.

Tide gauge stations along the west coast of Australia, for example in Fremantle and Port Headland (Fig. 2.4), are among the stations with the longest service record and it has been noted early that sea level along the west coast of Australia, i.e. in the Indian Ocean, is highly correlated to anomalies in the western Tropical Pacific (Clarke and Liu, 1994; Feng et al., 2004; Lee and McPhaden, 2008; Merrifield et al., 2012). Clarke and Liu (1994) concluded, from tide-gauge data and an equatorial wave model alone, that an equatorial waveguide, which crosses the marginal basins of the AMS, connects the regions and allows for the zonal propagation of sea-level

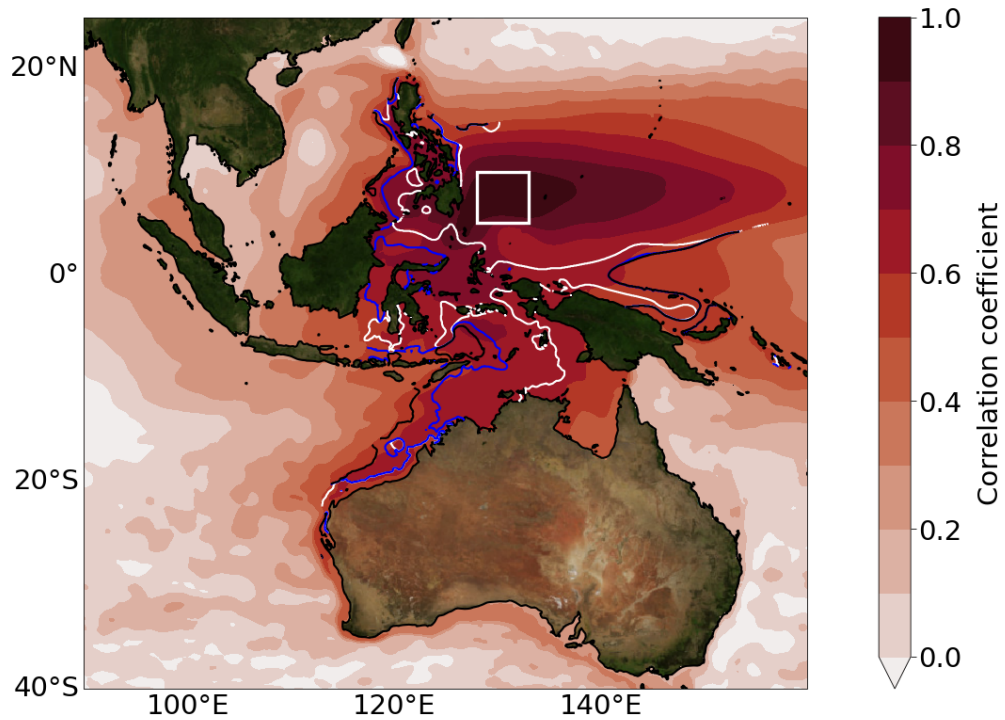


Fig. 1.2.: *Equatorial waveguide connecting the western tropical Pacific and the eastern Indian Ocean: coefficient of a lagged correlation between sea surface height (SSH) averaged over an area in the western tropical Pacific, indicated by the white box, and local SSH timeseries. Coloured contour lines indicate the lag of the maximum correlation at ten days (white), 20 days (blue) and 30 days (black). The linear trend and the seasonal cycle have been removed prior to all calculations.*

anomalies. The pathways along which sea-level anomalies from the western tropical Pacific penetrate the AMS are visualized in Fig 1.2. High correlations between local western tropical Pacific sea level indicate the location of a waveguide from the Pacific southeastward through the Makassar Strait and the Banda Sea and along the Australian shelf break into the Indian Ocean (see Fig. 5.1 for an overview map of the region). Another northward pathway is visible along the west coast of the Philippines Islands into the South China Sea (SCS). The coloured contour lines in Fig. 1.2 indicate the involved timescales. Anomalies reach the eastern part of the AMS in a matter of days (white line indicates ten days) but take about one month to reach the westcoast of Australia (blue and black lines indicate 20 and 30 days, respectively).

1.1.4 Measuring sea level

This modelling study aims to reproduce observed sea-level variability and therefore relies on observations to validate the results. The following section gives an introduction to sea-level measurements and discusses availability of observations, as well as the advantages and shortcomings of satellite altimetry and tide gauges¹.

Tide gauges

Traditionally, relative sea level is measured by tide gauges. Early installations were stilling-well gauges that consist of a sheltered well with a float that is connected to an (analogue) data recorder that stores the vertical position of the float every six minutes. Since the early 1990s acoustics gauges became common. The fundamental setup of a well or a vertical pipe is the same, but instead of using a float, the travel time of a sound pulse, emitted at a fixed position at the top of the well and reflected at the sea surface, is used to measure the vertical displacement of the sea surface. Because of the limited connection of the well to the sea, both type of gauges filter out high-frequency motion due to surface waves. The most common type of gauges today are radar reflecting gauges that use an electromagnetic signal instead of a sound pulse. They can be mounted at an elevated position above the sea surface without the need for shelter or a well. They are therefore easy and cheap to install and operate. Even though modern gauges operate at sampling frequencies of 1 Hz or higher, the traditional 6-minute interval is still common today. Tide gauges are coastal instruments. Apart from satellite altimetry, the only feasible way of measuring open-ocean sea level is by using bottom pressure gauges. Assuming the density of the water column and the atmospheric pressure are known, the bottom pressure measurement can be converted to a sea-level estimate using the hydrostatic balance. The device itself is rather cheap and easy to operate, but the deployment usually requires a ship mission. The use of bottom pressure gauges for measuring sea level is therefore very limited, and only done where satellite altimetry is unable to provide sufficient spatial or temporal coverage (for example at high latitudes).

All tide gauges measure relative sea level. In order to convert this into absolute sea level, the tide gauge datum needs to be monitored, as arbitrary changes of the datum

¹The name "tide gauge" reflects the initial intent of the first instruments deployed, even though their measurements were always influenced by more than just tides. A more appropriate term would be "sea level gauges" but since the former term is prevalent, even within the scientific community, it is also used here.

due to vertical land motion would result in spurious shifts or trends. Modern tide gauges, in particular those installed for scientific purposes, are therefore equipped with GPS receivers and/or an absolute gravimeter (Pugh and Woodworth, 2014). However, historical tide gauge measurements are often contaminated by vertical land motion. Another disadvantage concerns the spatial distribution of stations, which is not equal across the globe. This needs to be taken into account when computing global mean sea level from tide-gauge data (e.g. Church and White, 2011; Ray and Douglas, 2011; Jevrejeva et al., 2014; Dangendorf et al., 2017). Long-term measurements in particular are sparse and mostly available from stations in Europe and North America. The Permanent Service for Mean Sea Level (PSMSL; Holgate et al. 2012) collects and distributes data with a complete datum history from a global network of over 1000 tide-gauge station operated by local authorities. They reduce the measurements to a common datum to form a "Revised Local Reference" (RLR) dataset².

Satellite altimetry

Since the early 1990, satellite altimetry has revolutionized the field of oceanography because, for the first time, a near-global picture of sea-level variability was available. The physical principle of altimeter measurements is the same as for the radar gauges: the distance between the satellite and the surface, called "range", is calculated from the round trip time of an electromagnetic signal that is emitted from a satellite that orbits earth and is reflected at the sea surface. The exact knowledge of the satellite's distance to a reference ellipsoid and the speed of the signal allows to calculate the sea surface height, defined as the distance between the sea surface and the reference ellipsoid. In oceanography, the dynamic topography is usually of interest because it defines the geostrophic currents. It describes the difference between the earth geoid, i.e. a geopotential surface, and the sea surface. While the "Mean Dynamic Topography" (MDT) usually refers to a temporal average over a reference period, the "Absolute Dynamic Topography" (ADT) denotes the instantaneous deviation from the geoid. The anomaly with respect to the MDT is called "Sea Level Anomaly" (SLA). Figure 1.3 provides an overview of the altimetric principle. In order to reduce the error of the measurements, various corrections need to be applied to account for the dry gas components and water content of the troposphere, as well as for the atmosphere's electron content that affects the speed of the electromagnetic signal. Current altimeter missions are able to measure sea-level trends with an uncertainty

²<https://psmsl.org/data/obtaining>, last access: 16 December 2020

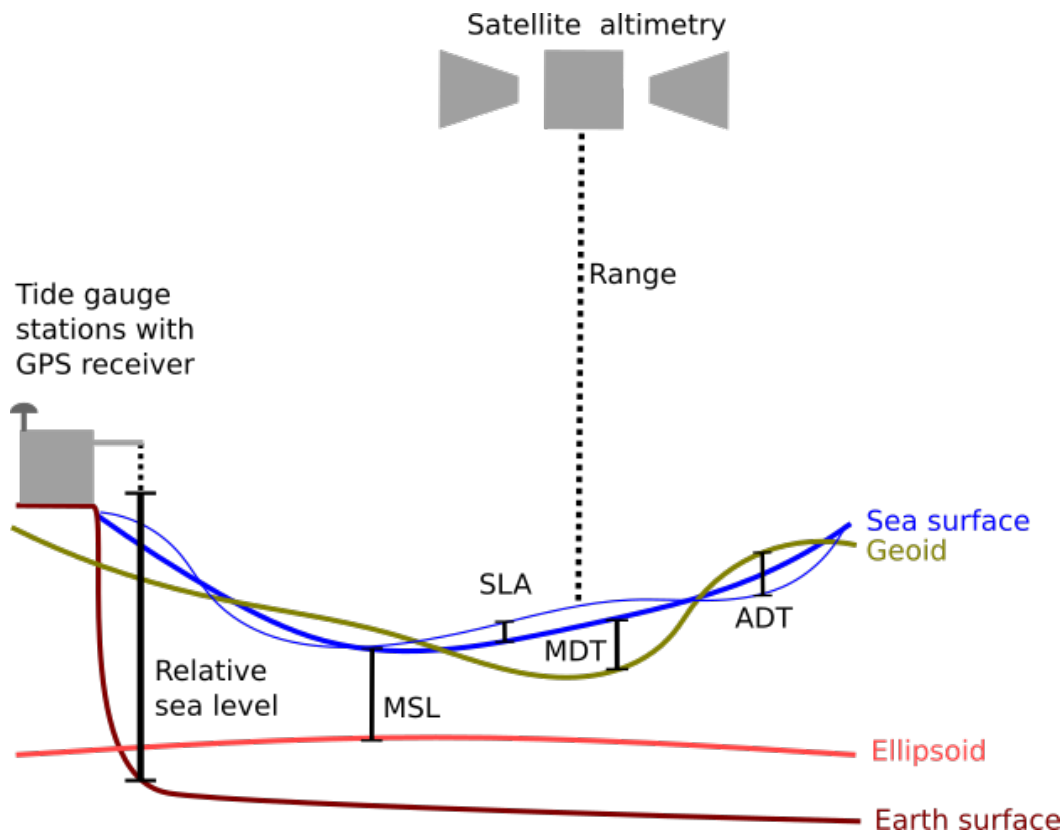


Fig. 1.3.: *Measuring sea level: dotted lines show distances measured by tide gauges and satellite altimetry. Vertical black lines denote commonly derived quantities mentioned in the text. The thin blue line depicts instantaneous deviation of the sea-level anomaly from its long term mean (bold blue line).*

of 0.5 mm yr^{-1} for global estimates and $1\text{--}2 \text{ mm yr}^{-1}$ on the regional scale (Ablain et al., 2015).

In contrast to tide gauges, satellite altimetry measures absolute sea level. Since 1992 a series of reference missions (TOPEX/Poseidon, Jason 1-3, Sentinel-6) provide near global coverage at an inclination of 66° with a repeat-cycle of 10 days. These reference missions are supplemented by several support and opportunity missions that are used to increase the spatio-temporal resolution. The altimetry data is routinely processed by the Copernicus Marine Environment Monitoring Service (CMEMS)³ that provides a range of along-track and gridded datasets. The RLR dataset from PSMSL as well as a gridded product⁴ from CMEMS is used complementary in several chapters of this thesis.

³<http://marine.copernicus.eu>

⁴https://resources.marine.copernicus.eu/?option=com_csw&view=details&product_id=SEALEVEL_GLO_PHY_L4_REP_OBSERVATIONS_008_047, last access: 12 June 2018

1.1.5 Diagnosing sea level

If not measured directly, sea-level variations can also be diagnosed from volume changes of the water column, due to density, mass or pressure changes. In order to diagnose the temporal evolution of sea level (η), we start from the continuity equation:

$$\nabla \cdot \rho \mathbf{v} = -\frac{\partial \rho}{\partial t} \quad (1.1)$$

where \mathbf{v} is the velocity vector and ρ is the density. Considering the vertical boundary conditions at the sea surface ($z = \eta$) and the bottom ($z = -H$):

$$\frac{\partial \eta}{\partial t} + \mathbf{u} \cdot \nabla \eta = \frac{Q_m}{\rho} + w \quad \text{at } z = \eta \quad (1.2a)$$

$$w = -\mathbf{u} \cdot \nabla H \quad \text{at } z = -H, \quad (1.2b)$$

where \mathbf{u} is the horizontal velocity vector, Q_m is the surface mass flux and w is the vertical velocity and integrating vertically from the bottom to the surface yields:

$$\frac{\partial \eta}{\partial t} = - \int_{-H}^{\eta} \frac{1}{\rho} \frac{\partial \rho}{\partial t} dz - \nabla \cdot \mathbf{U} + \frac{Q_m}{\rho}, \quad (1.3)$$

where $\mathbf{U} = \int_{-H}^{\eta} \mathbf{u} dz$. The first term on the right side represents steric changes that are due to changes of the vertically averaged in-situ density. The second term describes the convergence of vertically integrated horizontal flow, i.e. the redistribution of mass. Integrating globally eliminates this term. The last term accounts for mass fluxes across the ocean surface.

Steric changes can be further separated into changes due to temperature or salinity changes. We can modify the term for the steric effect in Eq. 1.3 to describe sea-level changes due to temperature variations:

$$\frac{\partial \eta^{thermosteric}}{\partial t} = - \int_{-H}^{\eta} \left(\frac{1}{\rho} \frac{\partial \rho}{\partial \Theta} \frac{\partial \Theta}{\partial t} \right) dz = \int_{-H}^{\eta} \left(\alpha \frac{\partial \Theta}{\partial t} \right) dz, \quad (1.4)$$

where $\alpha = -\frac{1}{\rho} \frac{\partial \rho}{\partial \Theta}$ is the thermal expansion coefficient and Θ is potential temperature. In the same way, halosteric sea-level variations can be expressed. We write:

$$\frac{\partial \eta^{halosteric}}{\partial t} = - \int_{-H}^{\eta} \left(\frac{1}{\rho} \frac{\partial \rho}{\partial S} \frac{\partial S}{\partial t} \right) dz = \int_{-H}^{\eta} \left(\beta \frac{\partial S}{\partial t} \right) dz, \quad (1.5)$$

where $\beta = \frac{1}{\rho} \frac{\partial \rho}{\partial S}$ is the haline contraction coefficient and S is salinity.

As pointed out by Griffies et al. (2014), α has large spatial gradients and varies by one order of magnitude between polar regions and the equator (see their Fig. 1). As a consequence, heating in the tropics produces a much larger sea-level signal than the same heating would at high latitudes. For the same reason, redistribution of heat can have an impact on global mean sea level when heat is moved along gradients of α , even if the total heat content is constant. In contrast, β has small spatial variations, on the order of 5 % (Griffies et al., 2014).

Boussinesq approximation

Ocean models provide a valuable tool to understand the mechanisms that shape sea-level variability, and Eq. 1.3 may be used to diagnose sea level from the output of an ocean model. However, a common approximation in ocean modelling is based on the assumption that, due to the near-incompressibility of ocean water, density variations are generally small and vary only on the order of 2-3 % (oceanic density typically ranges from 1025–1050 kg m⁻³). The density ρ can therefore be replaced by a mean density ρ_0 , except where it is associated with buoyancy forces, i.e. where density is multiplied with the gravitational acceleration. The continuity equations (Eq. 1.1) reduces to:

$$\nabla \cdot \mathbf{v} = 0. \quad (1.6)$$

In other words: conservation of mass is replaced by conservation of volume. With constant density, the sea-level tendency equation (Eq. 1.3) reduces to:

$$\frac{\partial \eta}{\partial t} = -\nabla \cdot \mathbf{U} + \frac{Q_m}{\rho_0}. \quad (1.7)$$

This approximation is referred to as the Boussinesq approximation (named after the French mathematician Joseph Valentin Boussinesq). Equation 1.7 illustrates that the sea level of a Boussinesq fluid is only affected by convergent velocities (first term on r.h.s.) and surface boundary fluxes of volume (second term on the r.h.s.). Because it is very accurate but reduces the non-linearity of the system and thereby the computational costs, it is frequently used in ocean modelling. Models that are based on the Boussinesq approximation also support larger timesteps during their integration because they filter out soundwaves, which propagate very fast but rely on a compressible fluid.

The use of the Boussinesq approximation has consequence, in particular for sea-level diagnostics. The total volume of a Boussinesq model can only be changed by volume fluxes, but it remains constant even if the global mean density changes. As a consequence, Boussinesq models are unable to diagnose steric global mean sea-level changes, for example due to global warming. They also suffer from spurious mass fluxes which can cause spurious pressure fields.

As pointed out in Griffies et al. (2014), it is important to note that sea-level patterns in Boussinesq models are affected by regional density changes, i.e. a local steric sea-level signal is included. We start from the hydrostatic balance to illustrate this:

$$p(z) = p_a + g \int_z^\eta \rho dz', \quad (1.8)$$

where p denotes the pressure at depth z or at the surface (p_a) and g is the gravitational acceleration. Note that ρ is not replaced by p_0 because it is multiplied by g . The bottom pressure is then given by:

$$p_b = p_a + g \int_H^\eta \rho dz. \quad (1.9)$$

Taking the time derivative yields an alternative expression for the sea-level tendency:

$$\frac{\partial \eta}{\partial t} = \frac{1}{g\rho(\eta)} \frac{\partial(p_b - p_a)}{\partial t} - \frac{1}{\rho(\eta)} \int_H^\eta \frac{\partial \rho}{\partial t} dz. \quad (1.10)$$

The first term on the right-hand side describes sea-level variations due to variations in mass of the water column. The last term accounts for local density changes, i.e. a local steric effect.

1.2 Turbulent energy fluxes in ocean models

The ocean is mainly forced at the surface through exchange of momentum, heat and fresh water with the atmosphere. Because several chapters of this thesis make use of sensitivity experiments that introduce specific perturbations to these fluxes, the following section provides a brief introduction to how they are typically computed

in ocean models.

The heat budget of the ocean is determined in approximately equal shares by radiative and turbulent fluxes. The former consists of incoming solar (i.e. short wave) radiation and terrestrial long wave radiation emitted from the atmosphere and the ocean. The net radiative forcing amounts to about 177 Wm^{-2} (Wild et al., 2015). The budget is closed by turbulent processes, namely latent and sensible heat fluxes, that are driven by evaporation and the temperature difference between the sea surface and the atmosphere, respectively.

The exchange of momentum is the result of vertical wind shear close to the ocean surface and the associated turbulence that drives the vertical flux of horizontal momentum. The shear stress exerted by the wind is called wind stress and depends not only on the relative velocity between the ocean currents and the surface winds, but also on the atmospheric stratification and the roughness of the sea surface. The wind stress drives ocean currents either directly or by exciting surface waves of different wavelengths, which transfer their energy to the mean currents when they break.

Measuring radiative energy transfer is rather easy and done routinely, but quantifying turbulent fluxes involves intricate measurements, which are therefore sparse. A global climatology of directly measured turbulent fluxes is unavailable (e.g. Brunke et al., 2011). Instead, these fluxes are related by bulk formulae to mean parameters of the atmosphere that are more easy to observe (Siedler et al., 2001):

$$\tau = \rho C_d (v - v_o) \quad (1.11)$$

$$SH = \rho C_h (T - T_o) \quad (1.12)$$

$$LH = \rho C_e u (q - q_o) \quad (1.13)$$

where τ is the wind stress, SH and LH are sensible and latent heat fluxes, respectively, ρ is the air density, v , T , and q are velocity, temperature and specific humidity and the subscript o denotes respective quantities of the ocean. C denotes the so called transfer (C_h, C_e) and drag (C_d) coefficients, which are determined empirically using direct flux measurements. They are functions of wind speed and atmospheric stability. Due to the fine scale nature of turbulent processes, ocean models are unable to simulate them directly but also make use of bulk formulae.

1.3 The importance of atmospheric forcing for sea-level studies with ocean models

Regional sea-level variability is primarily wind-forced (e.g. Forget and Ponte, 2015 or review by Stammer et al., 2013). Sea-level anomalies result directly from (Rossby) wave propagation, Ekman dynamics and upwelling, but also as a consequence of the changes of the wind-driven circulation. Consequently, the fidelity of the wind product used to drive an ocean model is of high importance for a realistic representation of sea-level variability.

In particular in recent decades, since the advent of space born altimetry and scatterometry in the early 1990s, most atmospheric reanalysis products enable a good representation of the dominant pattern of interannual sea-level variability when used as atmospheric forcing of ocean models. McGregor et al. (2012a) tested eight wind products with a linear shallow water model. They found that all datasets allow a reproduction of the major modes of tropical sea-level variability, with spatial correlation coefficients above 0.9 in the Indian and Pacific Oceans and only slightly below in the tropical Atlantic for all analysed products. However, they suggest an overestimation of the amplitude of variability for most datasets in all tropical basins. Carson et al. (2017) compared sea-level reconstructions, including three ocean reanalyses that are also based on an atmospheric forcing, with respect to low-frequency variability and long-term trends. Their results suggest that the dominant patterns of variability are in agreement between all reanalyses for most regions, although they find distinct regional differences in the extratropical Indian and Atlantic Oceans and differences with respect to the amplitude of tropical variability. Long-term trend estimates, on the other hand, appear to have a much larger uncertainty and estimates are very sensitive to the forcing. In their comparison, McGregor et al. (2012a) report a spatial correlation between simulated and observed trends below 0.6 for most datasets in the case of the Indian and the Atlantic Oceans and only slightly better results in the case of the Pacific. Most products fail to accurately capture the amplitude of the trends in all tropical basins, which range from 0.5 to 2.5 times the observed values. A large sensitivity of trend estimates to the applied wind forcing is confirmed by many studies (e.g. Han et al., 2010; Timmermann et al., 2010; Merrifield and Maltrud, 2011; Tokinaga et al., 2012) and the discrepancy between the products increases when considering the pre-altimetry era (Carson et al., 2017).

Several reasons for these uncertainties in sea-level trends are discussed in the literature. From a comparison of 16 ocean models, Storto et al. (2017) claims that the uncertainty during the altimetry era is mainly due to the halosteric trend estimates that reflect the uncertainty of the global freshwater budget rather than in the wind estimates. However, most studies emphasize spurious zonal wind-stress trends as the main reason for unrealistic sea-level variability in ocean models. McGregor et al. (2012a) point to a relation of inadequately captured meridional gradients of zonal wind stress (and the associated curl) and unrealistic regional sea-level trend estimates in the tropical Indian and Pacific Oceans. Hsu et al. (2021) supports this reasoning for the Pacific for two reanalysis products (CORE.v2 and JRA55-do) commonly used to drive ocean models.

The atmospheric reanalysis from the National Center for Environmental Prediction/National Center for Atmospheric Research (NCEP/NCAR; Kalnay et al. 1996) is a prominent example of spurious wind-stress trends in atmospheric reanalysis. (Pohlmann et al., 2017; Greatbatch et al., 2018) identify a long-term weakening of Pacific trade winds since the early 1960s that impact the thermocline and sea level throughout the tropical basin. For the altimeter period (specifically 1993-2007), on the other hand, McGregor et al. (2012a) point to an unrealistic trade-wind strengthening in the eastern tropical Pacific in the NCEP/NCAR reanalysis. They also identify an associated bias in sea level trends. Spurious trends in the NCEP/NCAR reanalysis are of special importance to the ocean modelling community because this reanalysis is the foundation of the widely used atmospheric forcing dataset of the Coordinated Ocean-ice Reference Experiments II (CORE.v2; Large and Yeager, 2004, 2009). Even though the CORE.v2 forcing is adjusted to agree with observations, spurious wind-stress trends and associated sea-level anomalies are still present, as Griffies et al. (2014) illustrate in a comprehensive inter-model comparison study. A comparison between the CORE.v2 forcing and observations for the period 1999 to 2009 reveals a negative bias of zonally averaged zonal wind speed at all latitudes between $\pm 60^\circ$ latitude, which is especially pronounced in the tropical Pacific (Tsuji no et al., 2018) and which supports the conclusion of an unrealistic strengthening of zonal winds in the CORE.v2 dataset since the early 90s. Among other reasons, these biases lead to the replacement of the forcing dataset of the CORE.v2 protocol by the aforementioned JRA55-do (Tsuji no et al., 2018), which is also used in this thesis. However, unlike the original CORE.v2 dataset, JRA55-do does not provide a climatological forcing that can be used to suppress variability on interannual and longer timescales. Because many research groups rely on such a forcing to conduct a range of sensitivity experiments, not only for sea-level studies, Stewart et al. (2020)

suggested a repeated-year-forcing (RYF) approach as a simple way to construct a climatological forcing from the interannually varying dataset. Chapter 3 will provide an assessment of this approach.

1.4 Aims and structure of this thesis

This thesis addresses three specific research questions and is structured as follows.

Chapter 2 provides an introduction to the ocean model framework and an overview over all numerical experiments used in the following chapters. It also contains a validation of the hindcast experiments with respect to observations.

Chapter 3 provides an assessment of the "repeated-year-forcing" approach. The analyses are focused on the model drift of different quantities over a typical hindcast period of several decades. The chapter presents three RYF-experiments conducted with the specific model setup used in this thesis. The first question addressed in this thesis is:

Q1: Is the repeated-year-forcing methodology with JRA55-do suited to force climatological experiments meant to characterize model drifts and transients over a typical hindcast period of several decades?

Based on the evaluation in chapter 3, the RYF approach is used to design experiments where the interannual variability of only momentum or of only buoyancy fluxes (i.e. heat and freshwater fluxes) are suppressed. Chapter 4 makes use of these runs to analyse how buoyancy fluxes, and in particular freshwater fluxes, modify the primarily wind-stress-driven interannual to decadal sea-level variability in the tropical Pacific. The second question of this thesis therefore is:

Q2: How do ocean–atmosphere buoyancy fluxes modify sea-level variability on interannual to decadal timescales in the tropical Pacific?

The analysis is extended into the AMS in chapter 5 and the focus is shifted to low-frequency variability. The importance of momentum and buoyancy fluxes as well as intrinsic processes for sea-level variability is discussed. Furthermore, the

specific impact of large-scale climate modes, which are known to characterize the wind-stress-driven variability in the tropical Pacific, is explored. To account for the fine-scale topography of the region, the analyses in chapter 5 are supported by a newly developed high-resolution model configuration to address the following question:

Q3: What is the nature of regional low-frequency sea-level variability in the Australasian Mediterranean Seas on decadal to multi-decadal time scales?

The final synthesis in chapter 6 summarizes the results of all chapters and provides a discussion of open questions.

Methods: Ocean General Circulation Models

The analyses in this thesis are based on a series of Ocean General Circulation Model (OGCM) experiments. A general introduction of the underlying model architecture, an overview over all experiments used in this thesis as well as a basic validation of the simulations in the region of interest is presented in this chapter. To avoid repetitions, specifics regarding individual experiments will be given in the following chapters.

2.1 Model design

The model used here is the "Nucleus for European Modelling of the Ocean" (NEMO) at version 3.6 (Madec and NEMO-team, 2016). NEMO combines several model components of which the Océan PARallélisé 8.2 (OPA; Madec et al. 1998), for the ocean dynamics and thermodynamics and the Louvain-La-Neuve sea-ice Model version 2 (LIM2-VP; Fichefet and Maqueda 1997) for sea-ice dynamics and thermodynamics are relevant here. OPA is based on the Navier-Stokes equations and the non-linear equations of state, i.e. the primitive equations, that are simplified by several approximations and assumptions (Madec and NEMO-team, 2016):

- Spherical earth: Surfaces of constant geopotential height are assumed to be fixed spheres and perpendicular to the earth radius.
- Thin shell: The depth of the ocean is small and negligible compared to the earth radius.
- Turbulence closure hypothesis: subgrid-scale, i.e. unresolved, effects are expressed as functions of the mean flow.
- Boussinesq approximations: density is replaced by a mean density except where it is associated with buoyancy forces (also see section 1.1.5).

- Hydrostatic approximation: the vertical momentum equation describes a balance between vertical pressure gradient and buoyancy forces.
- Incompressibility: Seawater is assumed to be incompressible so that the three-dimensional velocity becomes non-divergent.

The equations of the primitive equations are discretized on a staggered Arakawa-C grid (Arakawa and Lamb, 1977), that is meant to minimize the averaging and interpolations needed to derive the required terms. Laplacian and biaplacian operators are used to parameterize horizontal diffusion of tracer and momentum, respectively.

The horizontal and vertical grids of all models in this thesis are based on the global ORCA configuration of the DRAKKAR collaboration (Barnier et al., 2007) and employ a tri-polar, curvilinear, horizontal grid that avoids a singularity at the geographical North Pole by replacing it by two poles over Canada and Russia (Barnier et al., 2006). The vertical grid consists of 46 z-levels with varying layer thickness from 6 m at the surface to 250 m in the deepest levels and includes partial steps (Barnier et al., 2006). Bottom topography is interpolated from gridded global relief datasets.

Experiments with two different configurations are used in the context of this work. ORCA025.L46 is a global configuration with a horizontal resolution of $\frac{1}{4}^\circ$ and the basis for several hindcast and sensitivity experiments described below. The high-resolution configuration NUSA20 has been developed for this study. It makes use of the "adaptive grid refinement" (AGRIF; Debreu et al. 2008) to incorporate a regional high-resolution nest into a global base model. A two-way communication between the nest and the base model is established in a way that the base model provides the boundary conditions for the regional nest and is itself updated by the nest solution. As a consequence, the impact of the nest is also present in the solution of the base model and not only in the region of the nest. This approach is well established and the reader is referred to Schwarzkopf et al. (2019) for a detailed description of the procedure. The high-resolution nest of NUSA20 increases the horizontal resolution to $\frac{1}{20}^\circ$ in the area from 50°S to 25°N and 75°E to 180°E , i.e. covering the region of the AMS and Australia.

The majority of experiments are forced with the JRA55-do forcing (Tsujino et al., 2018) which builds on the JRA55 reanalysis product (Kobayashi et al., 2015) but merges satellite-based radiation and precipitation. Additional experiments build on the CORE.v2 atmospheric data set (Large and Yeager, 2004, 2009). All experiments

use the CORE.v2 bulk formulae (Large and Yeager, 2009).

The model employs a series of approximation and corrections that also affect sea-level diagnostics. As mentioned above the model makes use of the Boussinesq approximation introduced in chapter 1.1.5. This limits the ability to diagnose global mean sea level because the global mean steric effect is not included. However, this thesis is concerned with regional sea level variability, in particular with local steric changes. So this is not a serious limitation. The freshwater budget of an OGCM simulation is not in equilibrium. Freshwater fluxes (evaporation, precipitation, run-off), are still subject to large uncertainties. Additionally, freshwater fluxes in an OGCM do not only depend on the prescribed atmospheric state but also on the simulated ocean's state (specifically the sea surface temperature) and the specific choice of parameterizations and bulk formulae. As a consequence, even datasets specifically designed to drive OGCMs and to provide balanced freshwater fluxes fail to achieve this. As a consequence, freshwater fluxes of an OGCM are usually not in equilibrium which does also result in spurious drifts of sea surface height (SSH¹), as can be seen immediately from Eq. 1.7. Again, this limits the use of the model for GMSL studies, but the dynamical adjustment following a spurious freshwater signal occurs on the order of days (Greatbatch, 1994; Lorbacher et al., 2012) and the signal can be assumed to be globally uniform. The effect on regional diagnostic is therefore small. Nevertheless, in order to close the freshwater budget, the model allows to adjust the freshwater flux every few model time step and thereby to enforce a constant global mean sea level. Such a freshwater budget correction (FWBC) is used for several but not all experiments (Tab. 2.1). To avoid unrealistic sea surface salinity (SSS) fields from these spurious freshwater fluxes, all models employ a SSS-restoring. Freshwater fluxes are corrected by an additional term that acts to relax the SSS-field towards an observed climatology (WOA13; Boyer et al. 2013). The timescale of this relaxation differs for the experiments and ranges from 300 to 1250 days over the upper 50 m (Tab. 2.1). All experiments allow the sea surface to evolve freely but make use of a linearized and filtered free surface formulation (Roullet and Madec, 2000). An unfiltered free surface would allow the propagation of very fast external gravity waves (EGW; e.g. tides). Although, this would of course be desirable in terms of a realistic representation, their fast phase speed would demand a model integration time step on the order of seconds rather than minutes. In order to reduce the computational costs of the model, a filter is applied by introducing an additional force in the momentum equation that cancels the propagation of very fast EGW but leaves the dynamics on longer

¹I will refer to the sea-level estimate of the OGCMs, which gives height above the geoid, as SSH.

timescales unaffected. The linearization of the kinematic sea level equation (Eq. 1.7) is achieved by assuming $\eta \ll H \ll L$, where H and L are vertical and horizontal length scales, which reduces the surface boundary condition (Eq. 1.2a) to a linearized form of the kinematic sea level equation:

$$\frac{\partial \eta}{\partial t} = w|_{z=0} + \frac{Q_m}{\rho_0}. \quad (2.1)$$

Note that the exact conservation of heat and salt requires a non-linear free surface and is therefore lost with such a linear free surface. However, the error is expected to be small (Roullet and Madec, 2000).

Furthermore, the distribution of land and sea is constant over time, and tides are not included.

2.2 OGCM experiments

Throughout this thesis, nine experiments are used. Three hindcast simulations with JRA55-do (Tsujino et al., 2018) or CORE.v2 (Large and Yeager, 2009) forcing that are meant to reproduce observed conditions and six sensitivity experiments are conducted. Five sensitivity experiments use a "repeated-year-forcing" approach (RYF; Stewart et al. 2020), where the same 12-month period is used repeatedly, either for all ocean-atmosphere flux calculations or only for the calculation of either buoyancy or momentum fluxes. One climatological experiment uses the CORE Normal Year Forcing (CNYF; Large and Yeager 2004). The RYF-approach is introduced in detail in chapter 3.

Experiments under the CORE.v2 forcing are integrated from 1948 to 2009 or 62 years in case of the CNYF experiment, and experiments using the JRA55-do forcing run from 1958 to 2016 or 59 years in case of the RYF-runs. All experiments were preceded by a spin-up that provided the initial conditions. The procedure of a spin-up is meant to alleviate initial shocks and allow an initial adjustment to the forcing. Figure 2.1 summarizes the integration strategy of all experiments, and Tab. 2.1 provides relevant model parameter. Note that only six of these nine experiments were conducted in the course of this thesis.

Pre-existing experiments:

- HC-JRA: hindcast run with $\frac{1}{4}^\circ$ horizontal resolution, forced with interannually varying JRA55-do forcing (chapters 3,4,5).
- HC-CORE: hindcast run with $\frac{1}{4}^\circ$ horizontal resolution, forced with interannually varying CORE.v2 forcing (Patara et al., 2016; chapter 3).
- CNYF: sensitivity experiment with $\frac{1}{4}^\circ$ horizontal resolution, forced with climatological CNYF-forcing (Patara et al., 2016; chapter 3).

Experiments conducted for this thesis (all forced with JRA55-do):

- NUSA20: hindcast run, forced with interannually varying atmospheric forcing and including a high-resolution nest (chapter 5)
- RYF84, RYF90, RYF03: Three sensitivity experiment using three different periods as RYF-forcing (chapters 3,4,5).
- WIND: sensitivity experiment forced with RYF90 buoyancy fluxes (chapters 4,5).
- BUOY: sensitivity experiment forced with RYF90 momentum fluxes (chapters 4,5).

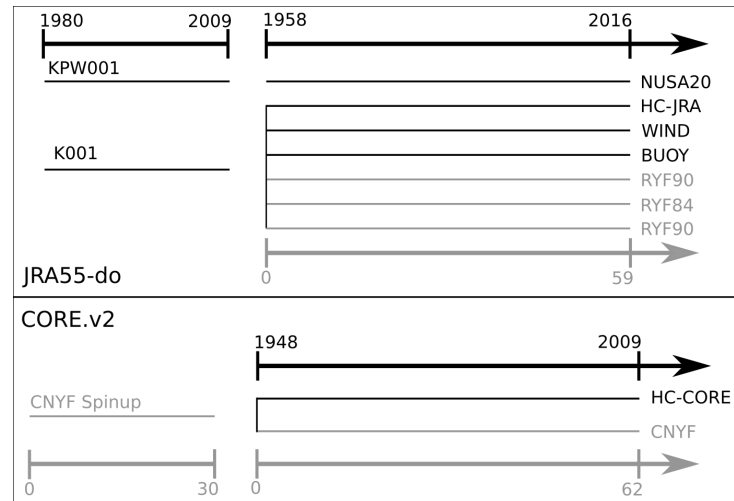


Fig. 2.1.: Schematic of OGCM-experiments forced with JRA55-do (upper box) and CORE.v2 (lower box). Black lines and labels indicate runs with interannually varying forcing while grey lines and labels indicate climatological/RYP-experiments.)

More details on the sensitivity experiments BUOY and WIND and caveats for the analysis will be provided in chapters 4 and 5.

	HC-JRA	NUSA20	RYF90	RYF84	RYF03
Resolution	0.25°	0.25° / 0.05°	0.25°	0.25°	0.25°
No. of gridpoints	67724972	67724972 / 162016416	67724972	67724972	67724972
Forcing	JRA55-do (v1.3)	JRA55-do (v1.4)	JRA55-do (v1.3)	JRA55-do (v1.3)	JRA55-do (v1.3)
Period	1958-2016	1958-2016	59 years	59 years	59 years
Output resolution	1 month	5 days / 5 days	1 month	1 month	1 month
Spinup period	1958-2009	1958-2009	1958-2009	1958-2009	1958-2009
FWB	Yes	No	Yes	Yes	Yes
SSS Restoring (Days 50 m ⁻¹)	365	365 / 1250	365	365	365
Hor. eddy diffusivity (m ² s ⁻¹)	300	300 / 60	300	300	300
Lateral boundary conditions	free slip	free slip / no slip	free slip	free slip	free slip
Internal Name	K003.hindcast	KPW002	KPW001.RYF90	KPW002.RYF84	KPW003.RYF03
	BUOY	WIND	HC-CORE	CNYF	
Resolution	0.25°	0.25°	0.25°	0.25°	
No. of gridpoints	67724972	67724972	67724972	67724972	
Forcing	JRA55-do (v1.3)	JRA55-do (v1.3)	CORE.v2	CORE.NYF	
Period	1958-2016	1958-2016	1948-2009	62 years	
Output resolution	1 month	1 month	1 month	1 month	
Spinup period	1980-2009	1980-2009	1980-2009	1980-2009	
FWB	Yes	Yes	No	No	
SSS Restoring (Days 50 m ⁻¹)	365	365	300	300	
Hor. eddy diffusivity (m ² s ⁻¹)	300	300	300	300	
Lateral boundary conditions	free slip	free slip	free slip	free slip	
Internal Name	K004.thermal90	K005.wind90	KLP228	KLP227	

Tab. 2.1.: Selection of model parameter of all experiments presented in this thesis. The first and second values given for NUSA20 represents values for the global base model and the high-resolution nest, respectively. FWB: freshwater budget; SSS: sea surface salinity.

2.3 Model validation

Chapters 4 and 5 of this thesis are concerned with sea level variability in the tropical Indo-Pacific. The remainder of this chapter therefore provide a comparison of the two hindcast experiments HC-JRA and NUSA20 to observations with a dedicated focus on this region. The CORE.v2-experiments are only used in chapter 3 to compare the RYF-approach to an established way of conducting climatological experiments. HC-CORE is therefore neglected in the following validation. A brief comparison of HC-CORE to observations is provided by Patara et al. (2016).

2.3.1 Sea surface height

Interannual SSH variability from the model hindcasts compares well with observations. Figure 2.2 compares standard deviations (SD) of annually averaged SSH timeseries from satellite altimetry data² to the model results. The domain is characterized by the prominent zonal dipole introduced in chapter 1, that appears here as spatial maxima in SD. Its eastern pole is centred on the equator in the central to eastern Pacific. The western pole is split in two maxima located north and south of the equator at around 10° latitude. Overall, this structure is well captured by the model experiments. However, the overall strength of the variability is slightly underestimated by the models. This is also illustrated by SSH anomalies averaged over three representative boxes in the northwestern (4°N - 14°N, 130°E - 150 °E), southwestern (15°S - 7°S, 159°E - 179 °E) and eastern (7°S - 3°N, 210°E - 240 °E) tropical Pacific. The out-of-phase variability of the eastern and western boxes is clearly visible here. Correlation coefficients of annually averaged timeseries from observations and model results are high and above 0.95 in all three boxes, but, compared to observations, standard deviations are lower by about 20 % for HC-JRA and 24 % for NUSA20 (Tab. 2.2).

Figure 2.2 also illustrates some first advantages of NUSA20 compared to the coarse-resolution configuration. In contrast to HC-JRA, NUSA20 is able to reproduce elevated levels of SSH variability, associated with increased mesoscale activity, off the east coast of Australia in the region of the East Australian Current and the Tasman front between 20° and 40°S. SSH variability in the southeastern Indian

²https://resources.marine.copernicus.eu/?option=com_csw&view=details&product_id=SEALEVEL_GLO_PHY_L4_REP_OBSERVATIONS_008_047, last access: 12 June 2018

Ocean is also underestimated by HC-JRA while the output of NUSA20 is close to observations.

Tide gauge measurements can be used to validate the model results for the pre-altimetry era. Timeseries from the RLR datasets distributed by the PSMSL (see chapter 1) are corrected for vertical land motion by subtracting a linear trend derived from the global GIA-model ICE-5G(VM2) (Peltier, 2004). Nevertheless, sea level at the tide gauge sites is not necessarily representative for open ocean variability. Local infrastructure or bathymetrie and localized vertical land motion unrelated to GIA might distort the signal. In order to identify stations that are representative of open variability, correlation coefficients between the tide gauge measurements and data from the closest altimetry grid cell are computed. Only stations that yield coefficients above 0.9 are used. Additionally, stations that provide data for less than 70 % of all month between January 1958 and December 2018 are discharged. As visualized in Fig. 2.4, in particular the later constraint reduces the number of stations, because most were deployed later. Only six sites within the region of interest (Fremantle, Port Hedland, Hawaii, Kwajalein, Guam and Palau) fulfil both criteria, of which five (excluding Hawaii) fall within the area of the high-resolution nest of NUSA20. These are used for a comparison with model data.

Correlations between models and observations are high at all six stations (Tab. 2.2). HC-JRA yields correlations that range from 0.58 at Kwajalein station to 0.89 at Port Headland. The high resolution output of NUSA20 does not cover Hawaii and produces slightly higher correlations at all other location that range from 0.72 at Kwajalein to 0.94 at Port Headleand. As for the comparison with satellite altimetry, the models underestimate the interannual variability. In case of the tide gauges, this is to be expected to some extent because they provide point-measurements in space, whereas the model output is an average over the grid cell. This is likely to be the reason for the improved performance in terms of amplitude of NUSA20. HC-JRA underestimates the variability by 31 % and NUSA20 by 22 %. Note that the satellite observations, which are provided as a gridded product with $\frac{1}{4}^\circ$ resolution, also yield lower amplitudes of variability (13 % on average; not shown).

Overall, both models are able to reproduce observed pattern of interannual sea-level variability but underestimate its magnitude. Differences between both configuration emerge in comparison with long-term tide gauge data, where the high-resolution configuration NUSA20 performs slightly better than HC-JRA.

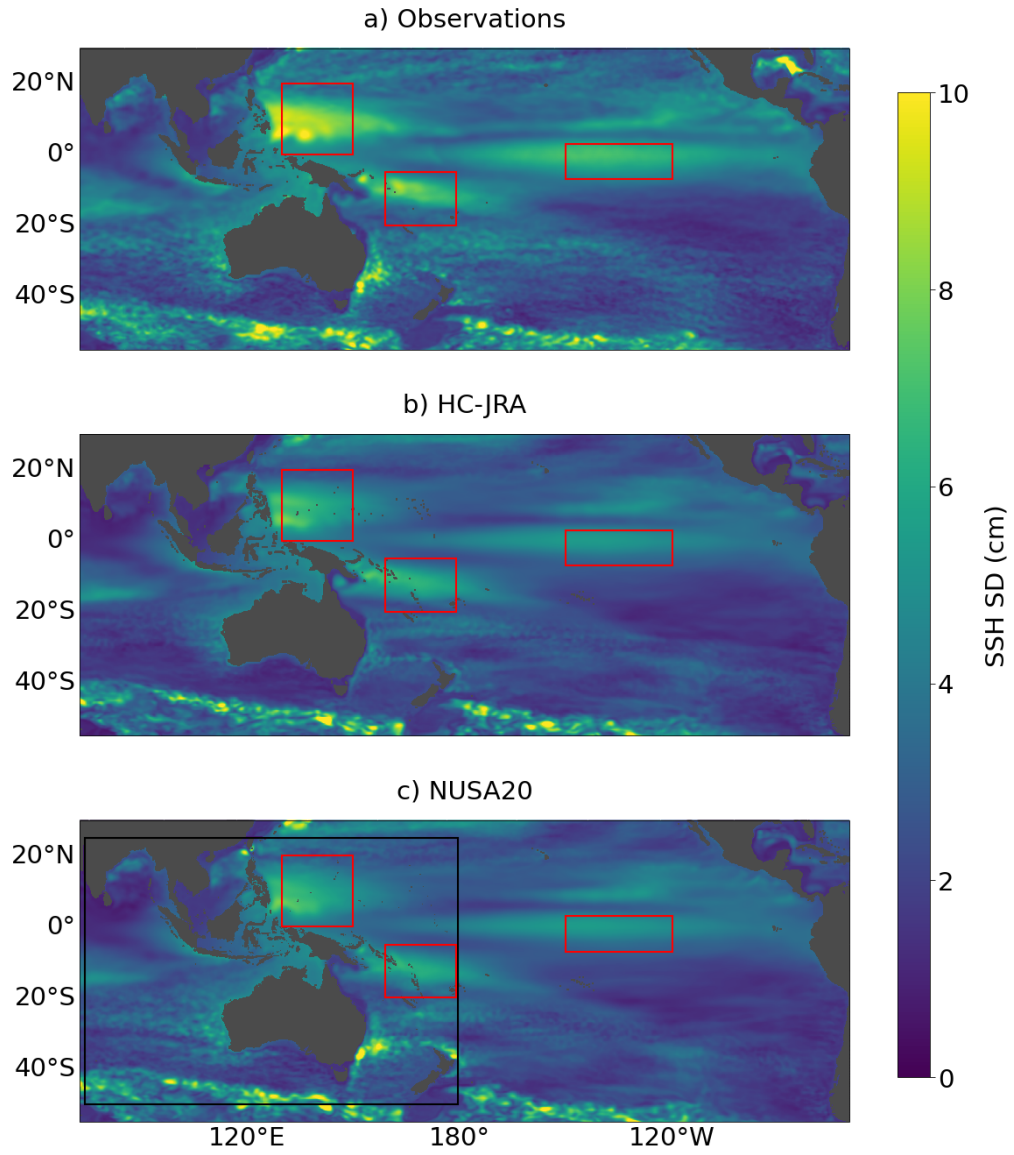


Fig. 2.2.: Standard deviation (SD) of annually averaged timeseries of sea surface height (SSH) from (a) altimetry, (b) HC-JRA and (c) NUSA20 for the altimetry period from 1993 to 2016. The black box indicates the region of the high-resolution nest of NUSA20. Red boxes indicate regions for spatial averages shown in Fig. 2.3.

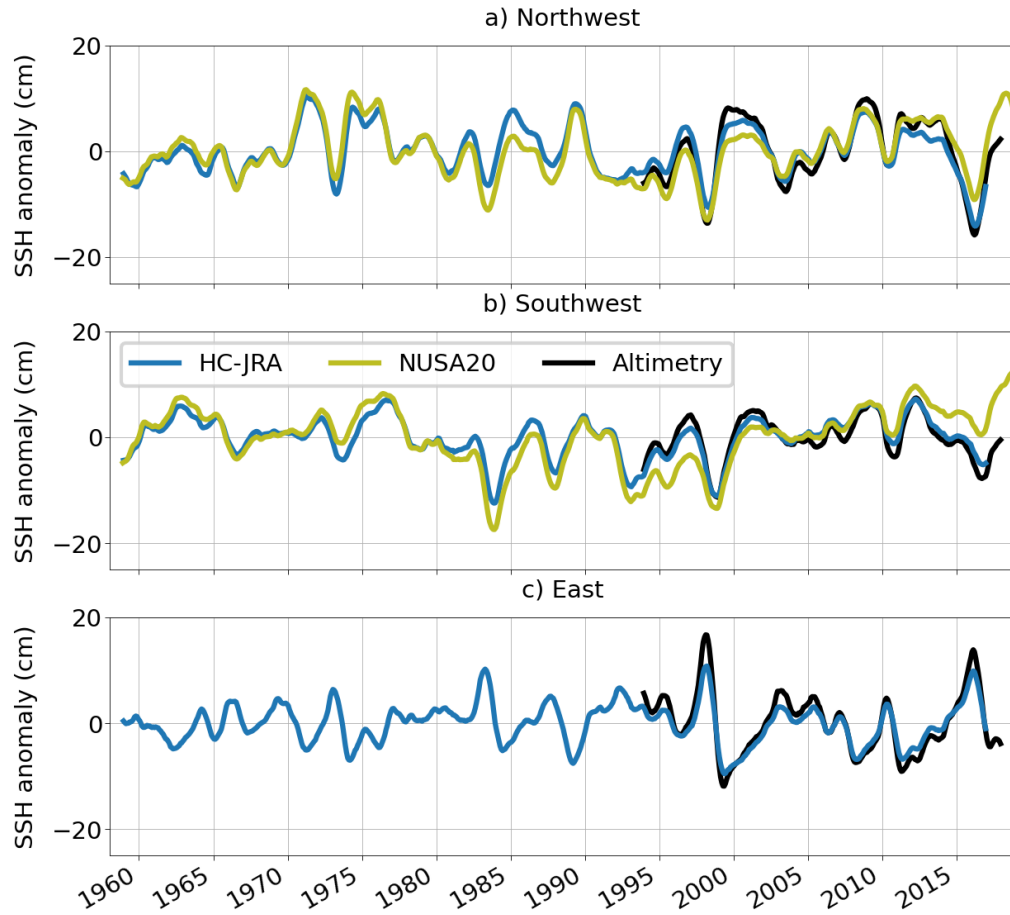


Fig. 2.3.: SSH anomaly timeseries from observations, HC-JRA and NUSA20, averaged over areas in the (a) northwestern, (b) southwestern and (c) eastern tropical Pacific as shown in Fig. 2.2. Anomalies were computed with respect to the period 1958–2016 and 1993–2016 for the model and altimetry data, respectively. The model data has been detrended and a global mean sea level has been subtracted from the altimetry data. All timeseries were smoothed with a 12-month running mean.

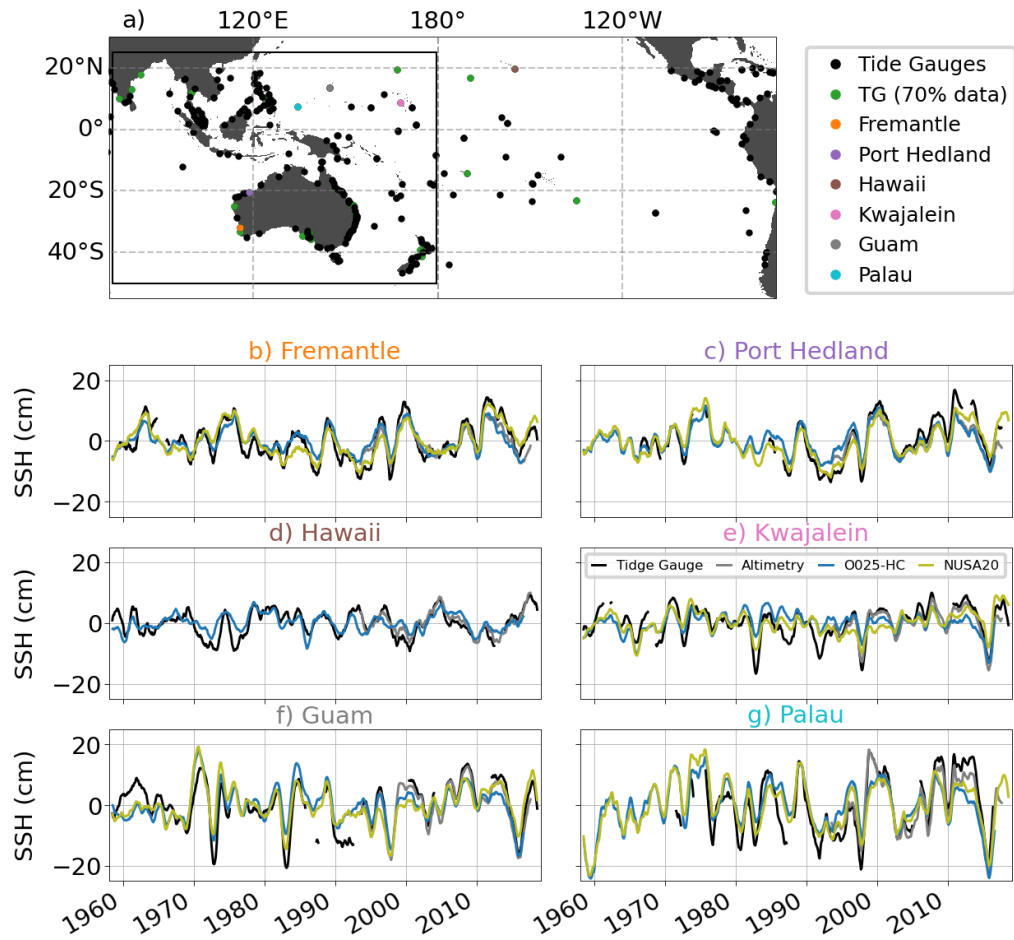


Fig. 2.4.: a) Location of all tide gauge stations in the domain available from Permanent Service of Mean Sea Level (PSMSL). The high-resolution domain of NUSA20 is indicated by the black box. Stations that have data for at least 70 % of all month between January 1958 and December 2016 are marked in blue. Six stations additionally show high correlations ($p > 0.9$) with altimetry measurements. Those stations are marked individually and used for model comparison in the six lower panels. (b-g) SSH anomaly timeseries smoothed with a 12-month running mean from tide gauge measurements (black), altimetry (gray), HC-JRA (blue) and NUSA20 (yellow).

	Obs	HC-JRA			NUSA20		
	SD (cm)	SD (cm)	ratio	ρ	SD (cm)	ratio	ρ
NWTP	5.4	4.2	0.78	0.96	3.8	0.7	0.96
SWTP	3.6	3.3	0.92	0.95	2.9	0.81	0.95
ETP	5.6	4.0	0.71	0.99	x	x	x
Average			0.80			0.76	
Fremantle	6.0	3.7	0.62	0.88	4.9	0.82	0.89
Port Headland	7.0	4.3	0.61	0.89	5.4	0.77	0.94
Hawaii	3.8	2.7	0.71	0.59	x	x	x
Kwajalein	4.8	3.0	0.62	0.58	3.3	0.69	0.72
Guam	7.1	5.3	0.75	0.7	5.7	0.8	0.74
Palau	9.4	7.4	0.79	0.72	7.8	0.83	0.79
Average			0.69			0.78	

Tab. 2.2.: SD of annually averaged SSH anomaly timeseries from observations and model data and ratio of these SDs (Model/Obs). Correlation coefficients (ρ) of annually averaged and detrended SSH timeseries between observations and models for the overlapping period. First three rows give values for SSH data from altimetry observations and models, averaged over three boxes in the northwestern (4°N – 14°N, 130°E – 150 °E), southwestern (15°S – 7°S, 159°E – 179 °E) and eastern (7°S – 3°N, 210°E – 240 °E) tropical Pacific as shown in Fig. 2.2. The corresponding timeseries are shown in Fig. 2.3. The lower three rows give values for SSH data from tide gauge observations and models. The location of the sites and the corresponding timeseries are shown in Fig. 2.4.

2.3.2 Western tropical Pacific stratification

Sea level is an integrated measure of the whole water column and it is therefore crucial to properly represent T-S characteristics in order to produce realistic sea-level estimates. The following paragraphs will compare model results to observational data in this respect. Temperature and salinity data from the World Ocean Atlas 2018³ (WOA18; Locarnini et al. 2019; Zweng et al. 2019) will serve as an observational benchmark.

Figure 2.5 compares temperature and salinity at a meridional section averaged zonally from 160°E to 180°E. The typical equatorial warmpool, with temperature of up to 29°C and a poleward decrease, is clearly visible (Fig. 2.5a). Surface salinity is highest in the subtropical regions due to excess evaporation. These high salinity waters are subducted and transported equatorward where they form a subsurface salinity maximum, usually referred to as "Subtropical Underwater" (STUW). The atmospheric convergence zones just north and south of the equator are characterized with surface salinity minima due to excess precipitation (Fig. 2.5b). Both

³<https://www.ncei.noaa.gov/archive/accession/NCEI-WOA18>, last access: 16 February 2021

model hindcasts reproduce this structure but also show some distinct differences. The strongest temperature biases of up to 4°C are found in both simulations at a depth of around 200 m, symmetric about the equator at 4° latitude, indicating an upward displacement of the thermocline (Fig. 2.5c and e). Salinity biases of up to 0.4 psu and 0.3 psu are present in HC-JRA and NUSA20 respectively, because the STUW, in particular in the Southern Hemisphere at around 10° S, is more saline than observations suggest. A negative salinity bias of the same magnitude is found below the thermocline in both experiments, again indicating a vertical displacement of the STUW. NUSA20 shows slightly weaker salinity biases, in particular along the subduction pathways of the STUW marked by the 1025 kg m⁻³ isopycnal in Fig. 2.5. It is noteworthy that most changes (in particular above the 1027 kg m⁻³ isopycnal and south of 15° S) appear to be density compensated, i.e. warm biases coincide with positive salinity biases and vice versa. The density structure is therefore very close to observations.

The mean states and biases of temperature and salinity, averaged over the upper 400 m, illustrate that these biases are not localized but are present throughout the tropical Pacific with almost no differences between HC-JRA and NUSA20 (Fig. 2.6). In fact, salinity biases in the eastern Pacific at around 20°S are even stronger in NUSA20 than in HC-JRA, probably due to the missing FWBC correction (Fig. 2.6 e,f). A different picture emerges for the eastern Indian Ocean. the coarse resolution configuration HC-JRA produces strong temperature and salinity biases, in particular in the Bay of Bengal and off the west coast of Australia, where salinity biases exceed 0.3 psu. Although still present, NUSA20 reduces these biases. Furthermore, in contrast to HC-JRA, NUSA20 produces very realistic results in the region of the ITF outflow in the Indian Ocean around 20°S and in the AMS, which is encouraging as NUSA20 was specifically developed to support analysis in this region. Note for example the strong biases of over 2.5 K and 0.2 psu in the northern part of the South China Sea in HC-JRA that are not reproduced by NUSA20. These differences with respect to the AMS will be discussed in more detail in chapter 5.

2.3.3 Makassar Strait

The AMS forms the only tropical inter-ocean exchange pathway, and the ITF is an important component for the large scale climate systems and part of the global meridional overturning circulation. The primary pathway of the ITF is through the

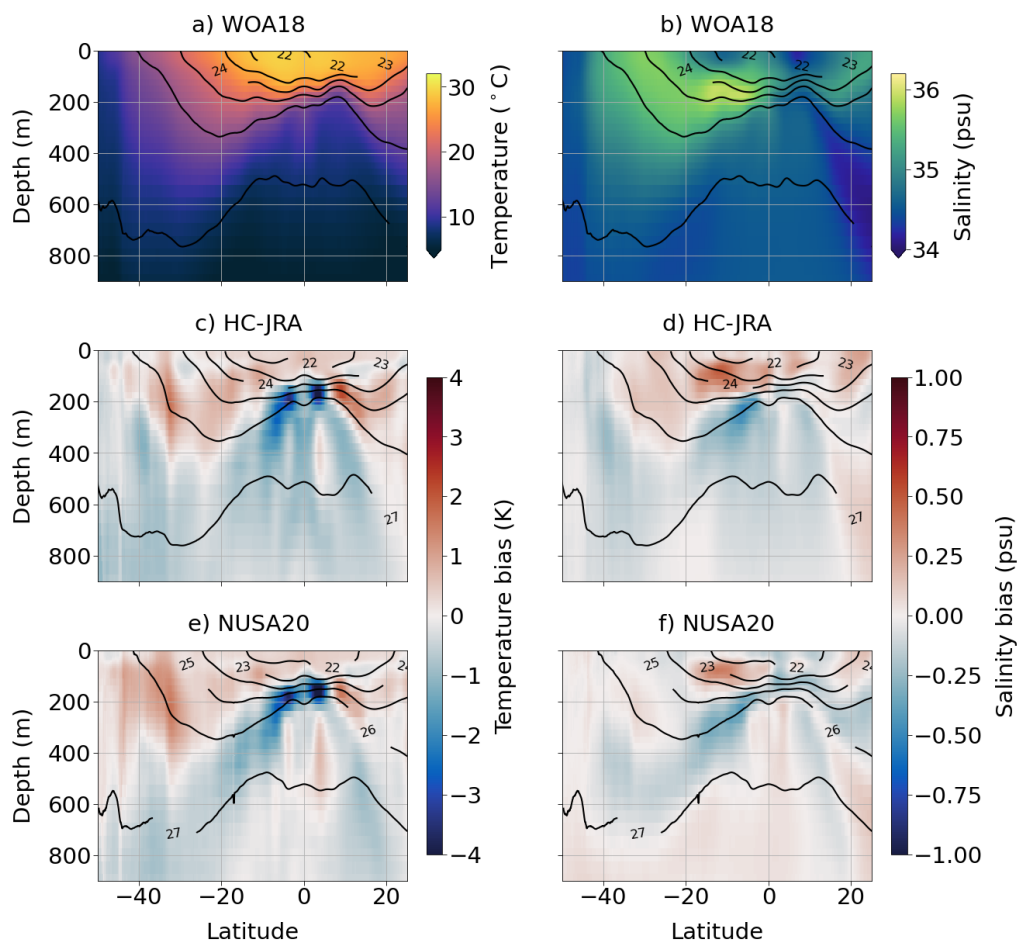


Fig. 2.5.: Meridional sections of (a) temperature and (b) salinity averaged from 160°E to 180°E from WOA18 and corresponding model biases of (c-d) HC-JRA and (e-f) NUSA20.

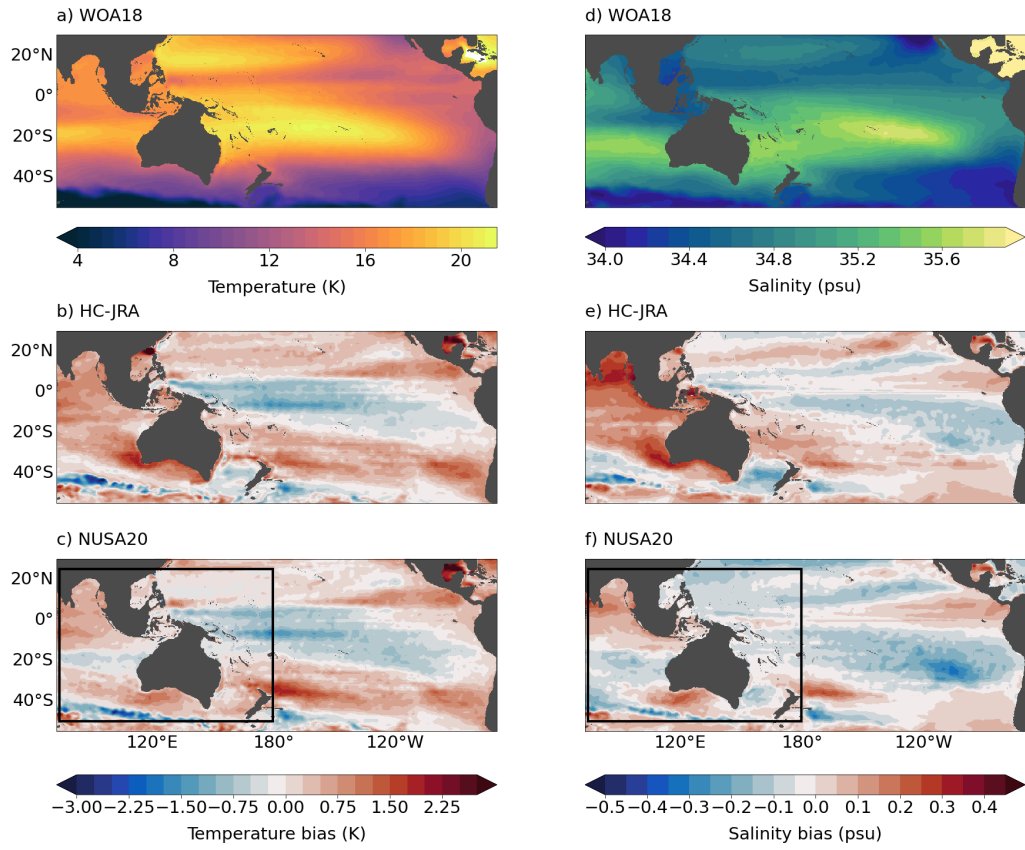


Fig. 2.6.: Mean state of temperature (a) and salinity (d) averaged over the upper 400 m from WOA18 and respective model biases for HC-JRA (second row) and NUSA20 (third row).

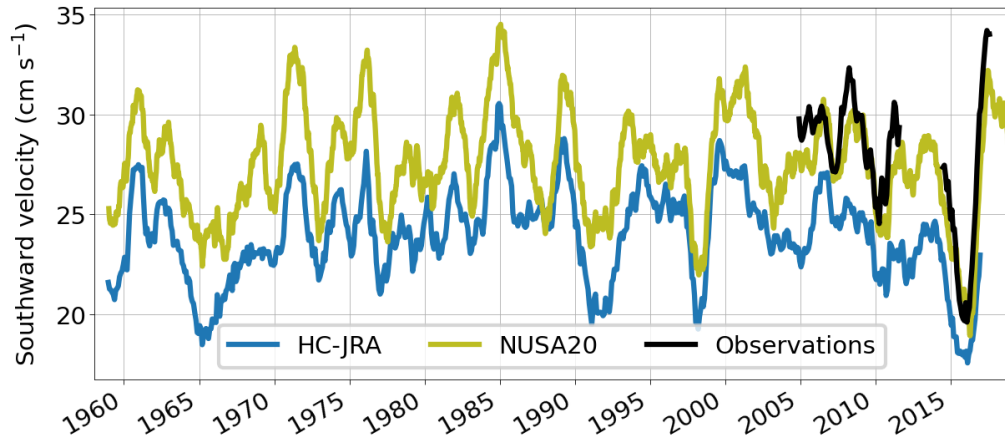


Fig. 2.7.: Southward velocities through Makassar Strait at 2.5°S from observations, HC-JRA and NUSA20. Model velocities are taken from the grid point closest to the mooring, which is located at $118^{\circ}27'3\text{ E}$. See Fig. 2.8 for reference.

Makassar strait that separates Borneo and Sulawesi. It is therefore the best sampled strait in the region with almost continuous observation between 2004 and 2017.

Two caveats need to be considered when comparing the observational velocity⁴ (Gordon et al., 2019) and transport estimates with model results. Firstly, observations from only one mooring in the western part of the channel cover the whole period. Transport estimates are derived by interpolating velocities to the channel boundaries (Gordon et al., 2019; Susanto and Tony Song, 2015; Gordon et al., 2012) which introduces an additional source of error. I therefore focus on a comparison of velocities rather than transport estimates. Secondly, the orientation of the Labani channel (the deep part of the Makassar Strait) is 170° . In order to compute true along channel velocities from the ocean model output, interpolation of meridional and zonal velocities on a common grid would be required, because the model output is staggered on an Arakawa-C grid. In case of HC-JRA this is complicated by the fact that the Labani channel is represented by only 2 grid points, which makes zonal interpolation difficult. Therefore, southward velocities rather than along channel velocities are compared below. This reduces the shown velocities by approximately 5% and has little effect on the transport estimates.

Depth averaged, southward velocities at the location of the mooring compare well between observations and both models, but NUSA20 is much closer to observations

⁴<https://doi.org/10.7916/d8-p78a-zm51>, last access: 27 January 2021

(Fig. 2.7). Note that the following statistical comparison is limited to the overlapping periods of models and measurements. Observations suggest a mean velocity of 27.7 cm s^{-1} . NUSA20 is slightly below that estimate with 26.4 cm s^{-1} and HC-JRA is further off with only 24.6 cm s^{-1} . Variability is evaluated based on timeseries smoothed with a 12-month running mean to filter out seasonal variability. Correlations with observations are 0.53 and 0.81 for HC-JRA and NUSA20, respectively (both significant on a 99% confidence interval) and standard deviations of the three time series are 3.2 cm s^{-1} , 1.6 cm s^{-1} and 2.3 cm s^{-1} for observations, HC-JRA and NUSA20, respectively. It is noteworthy that a large portion of the discrepancy in SDs is due to the strong increase after 2015 that is not adequately captured by both models. Excluding all years after 2014 reduces the discrepancy in SDs to 0.36 cm s^{-1} and 0.58 cm s^{-1} for NUSA20 and HC-JRA, respectively. Nevertheless, both models, and HC-JRA in particular, underestimate the interannual variability.

The reason for this inter-model differences is the complex topography in the region and the fine-scale velocity structure that is not adequately resolved with 0.25° resolution. This becomes obvious from Fig. 2.8 that shows a zonal section at 2.5°N (the latitude of the mooring) across the Makassar Strait. In HC-JRA the Labani channel is represented by only two grid points, the shelf region is too deep and misses some fine-scale topographic features and the velocity core is about 25 km broad (the zonal extent of a single model grid box). With $\frac{1}{20}^\circ$ horizontal resolution, NUSA20 is able to resolve much more topographic features and the zonal structure of the current. The velocity core is at a similar depth between 100 m and 200 m in both simulations. Unlike in HC-JRA, where a relevant fraction of the southward flow is on the shelf, in NUSA20 the flow is mostly confined to the Labani channel east of 118°E . Although horizontal resolution is likely to be the dominant factor, it should be noted that lateral boundary conditions also differ between both configurations and could also, at least in parts, account for the differences. While HC-JRA uses a "free slip" conditions, a "no slip" condition is used within the high-resolution nest of NUSA20 (Tab. 2.1)

The observed vertical structure of the flow features a distinct subsurface velocity maximum of 63 cm s^{-1} at 120 m depth and a subsequent decline to 3 cm s^{-1} at 760 m (Fig. 2.9 a). Although both simulations reproduce this structure, HC-JRA strongly overestimates the velocity maximum with values of over 120 cm s^{-1} at 120 m and a strong decline to northward flow below 350 m, which results in strong vertical shear at intermediate depths. This bias is improved with NUSA20, which however still overestimates the strength of the current, with maximum values of 83 cm s^{-1} . The

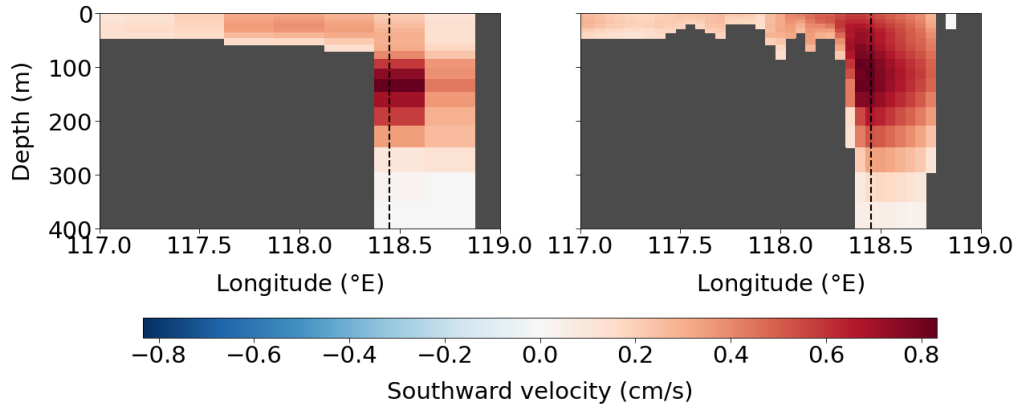


Fig. 2.8.: Southward velocities at a section at 2.5°S across the Makassar strait from (a) HC-JRA and (b) NUSA20. Dashed black line indicates location of mooring array.

flow drops to zero at about 450 m and does not show northward velocities.

The ITF is also characterized by a distinct seasonal cycle with maximum southward flow in August, which is also when the flow reaches its shallowest position above 100 m. The subsurface flow is weakest in December, when it is at its deepest position at about 150 m. Northward flow is only observed in boreal fall and winter below 500 m (Fig. 2.9b). This seasonal cycle and vertical propagation of the subsurface flow is reproduced only by NUSA20. HC-JRA shows velocities above 100 cm s^{-1} at depths of 120 m throughout the year and northward velocities below 300 m from March to December (Fig. 2.9 c, d).

Most recent estimates of total volume transport across the Makassar Strait are based on the observations shown above and give mean values of 12.5 Sv for the period between 2004 and 2017 (Gordon et al., 2019). Despite the overestimation of the subsurface flow in the upper layers, both simulations yield lower values of 11.3 Sv and 10.2 Sv in case of NUSA20 and HC-JRA respectively (not shown). This is due to the strong vertical shear that causes an unrealistic strong reduction of transport in the lower layers between 300 m and 700 m. Indeed, when considering only the upper 300 m Gordon et al. (2019) report observed values of 9.1 Sv which is exactly reproduced by NUSA20 but not by HC-JRA which gives 11.2 Sv .

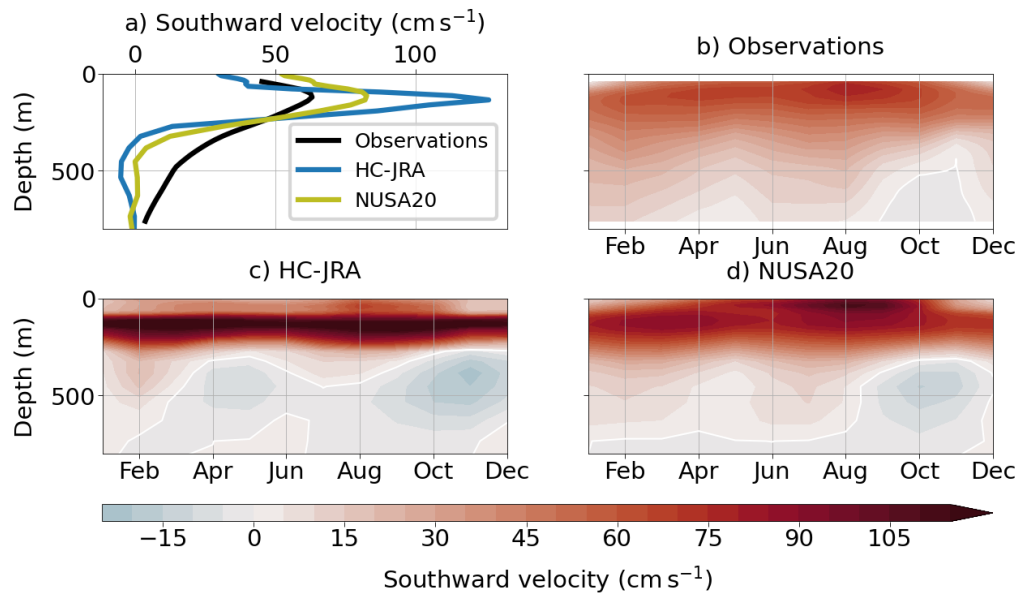


Fig. 2.9.: (a) Profile of southward velocities in the Labani channel from observations, HC-JRA and NUSA20. (b-d) Seasonal cycle of southward velocities from observations, HC-JRA and NUSA20 respectively. Model velocities are taken from the grid point closest to the mooring which is located at 118°27'3 E. See Fig. 2.8 for reference.

Assessment of a repeated year forcing

This chapter addresses the first research question stated in the introduction: the assessment of a repeated year forcing (RYF) with JRA55-do. The chapter makes use of six experiments introduced in the introduction. Three different RYF-experiments are compared to the respective hindcast simulation HC-JRA, and the Normal Year experiment CNYF is shown together with the corresponding hindcast experiment HC-CORE.

Markus Scheinert made the model output of the experiment HC-JRA available, and Lavinia Patara provided the output of HC-CORE and CNYF.

3.1 Abstract

This chapter evaluates the repeated-year-forcing methodology (RYF) as a way to complement the JRA55-do dataset, designed as a comprehensive forcing to drive ocean-sea-ice models, by a single repeating annual cycle. Such a forcing is necessary to conduct experiments without any imposed interannual variability: so-called climatological experiments. Three experiments forced by the periods from 1st May to 1st April of the years 1984/85, 1990/91 and 2003/04 (RYF84, RYF90, RYF03) are tested for their ability to characterize the model drift and transients over a typical hindcast period. It is shown that all three periods support a successful 59-year integration. The evolution of global mean temperatures and salinities is similar in all RYF-experiments and comparable to the hindcast simulation. Vertical and horizontal trend patterns of temperature and salinity are consistent across models and are, apart from surface trends, due to adjustment processes towards a model equilibrium or model deficiencies that cause spurious trends. Trends of key transports of the global overturning circulation are analysed. All RYF-experiments show similar trends that are consistent with the behaviour of the hindcast experiment. The choice of a single period might depend on the particular research question. However, RYF03 shows the largest deviations and is therefore rated as the least suitable candidate.

Furthermore, the quantification of spurious trends in the hindcast experiments based on three RYF-simulations is discussed.

3.2 Introduction

The ocean is mainly set into motion by the overlying atmosphere via air–sea momentum, heat and freshwater fluxes. Unlike in coupled ocean-atmosphere experiments, ocean-only experiments (as they are used throughout this thesis) use prescribed atmospheric fields as external drivers. Momentum, heat and freshwater surface fluxes are computed via bulk formulae (e.g. Large and Yeager, 2004) using these atmospheric field and the ocean model’s sea surface temperature (SST).

An advantage of the use of prescribed atmospheric forcing is that it allows for dedicated sensitivity experiments. Specific perturbations can be introduced to the atmospheric dataset to study the subsequent effect on the ocean and thereby advance the mechanistic understanding of the ocean-atmosphere system. A well established type of sensitivity studies are "climatological" experiments. Atmospherically forced variability, specifically on timescales longer than one year, is suppressed to study the contributions of the ocean’s intrinsic dynamics to the total variability, which is obtained from reference experiments using the full atmospheric forcing. This is found to be particularly useful because the variability directly forced by the atmosphere is often dominant, making it challenging to identify more subtle signals (Large and Yeager, 2004). However, climatological experiments can also serve a wider range of purposes.

1. Analyse ocean model drift and initial adjustment processes (e.g. Biastoch et al., 2009; Ummenhofer et al., 2013; Yeager and Danabasoglu, 2014; Ummenhofer et al., 2017; Jin et al., 2018; Patara et al., 2021).
2. Obtain a sufficiently equilibrated, climatological state of the ocean to be used as initial condition for further simulations (e.g. Duteil et al., 2014; Schwarzkopf, 2016; Stewart et al., 2020). Although the purpose is different, the requirements for such experiments are very similar to the first point. In order to reach a climatological equilibrium, the model drift needs to be small and the surface fluxes balanced.

3. Analyse "intrinsic"¹ variability that is generated spontaneously by an (eddy) ocean under steady atmospheric forcing (e.g. Penduff et al., 2011; Patara et al., 2016; Rieck et al., 2018; Penduff et al., 2019).
4. Separate forcing mechanism with specific sensitivity experiments (e.g. Schwarzkopf and Böning, 2011; Ummenhofer et al., 2013; Yeager and Danabasoglu, 2014; Patara and Böning, 2014; Jin et al., 2018; Ummenhofer et al., 2020; Ryan et al., 2021). The climatological forcing can be used to replace only parts of the atmospheric forcing, while the full interannual variability is retained otherwise. Interannual variability might be removed in specific regions only or for individual processes. A prominent example for the latter are so-called Buoyancy and Wind experiments, which will be used in section 4 and 5.

To facilitate climatological experiments, the protocol for "Coordinated Ocean-ice Reference Experiments" (CORE; Griffies et al. 2009) provides such a climatological forcing dataset. CORE defines a standardized framework for global ocean-sea-ice experiments using the same bulk formulae and atmospheric forcing. It provides two options of atmospheric forcing: an interannual forcing that varies from year to year (Corrected Inter-Annual Forcing; CIAF) and a climatological "Normal Year Forcing" (Corrected Normal Year Forcing; CNYF) that consists of a repeated annual cycle (Large and Yeager, 2004, 2009). As described in Large and Yeager (2004) the CNYF forcing was developed to meet the following six criteria:

1. Same structure as the CIAF dataset to permit an easy use of mixed forcing datasets
2. Include seasonal cycle
3. Include realistic high frequency variability (i.e weather), in particular storm events
4. Obtained fluxes should be as close as possible to a climatological mean.
5. Smooth transition between December and January to avoid initiation of spurious transients
6. Not weighted towards one particular year

The third criterion prevents the use of a climatological seasonal cycle, which complicates the endeavour of creating a suitable dataset substantially. The motivation beyond this requirement is the non-linear nature of the bulk formulae used to compute turbulent air-sea fluxes. For example, vertical momentum flux depends on the cube of the wind speed (Large and Yeager, 2009). Using mere climatological averages and thereby neglecting synoptic effects would therefore underestimate mean and seasonal averages of turbulent fluxes (e.g. Gulev, 1994; Ponte and Rosen,

¹The concept of intrinsic variability is also referred to as "chaotic" or "internal" variability.

2004; Hughes et al., 2012; Zhai et al., 2012).

Large and Yeager (2004) put a particular emphasis on point 4 to ensure closed surface flux budgets (i.e. no net ocean–atmosphere heat, freshwater and momentum fluxes) and make certain that the resulting ocean model output represents a meaningful, equilibrated, climatological state. However, it is important to note that the computation of turbulent fluxes does not only depend on the atmospheric field but also on the state of the ocean. The CNYF dataset assumes observed fields, but data provided by the ocean model is likely to deviate. Constructing an atmospheric forcing dataset that allows an equilibrated state for any given ocean model is therefore a challenging task.

The CNYF dataset is generated synthetically by spectrally averaging wind vectors, temperature and specific humidity fields over multiple decades such that the result represents observations in terms of long-term mean states and intra-annual variability. Climatologies are used for radiation, precipitation and run-off. A consequence of this approach is a lack of consistency between different fields.

The two stages of the CORE protocol and its forcing datasets proved to be useful in assessing inter-model differences and gaining insight into the climate system (e.g. Griffies et al., 2009, 2012; Danabasoglu et al., 2016; Tseng et al., 2016). However, various shortcomings became apparent over the last decade. Apart from biases in physical properties, like an overestimation of the zonal wind stress in the tropical domain (Tsujino et al., 2018), the CIAF dataset has not been updated since 2009 and thereby prevents research on the recent evolution of the climate system. This motivated the development of the updated forcing dataset JRA55-do (Tsujino et al., 2018) to be used in the CORE framework. The product is based on the Japanese reanalysis system JRA55 and the reader is referred to Tsujino et al. (2018) for details.

In the context of climatological experiments, it is important to note that the JRA55-do forcing is not complemented by a "Normal Year Forcing" dataset. Instead, the authors suggest using a repeated year forcing (RYF), i.e. the repeated use of the same 12-month period taken from the original, interannually varying JRA55-do dataset. However, they do not present an evaluation of the approach.

This task is taken on by Stewart et al. (2020), who reconsider the criteria a climatological forcing for state-of-the-art ocean models should meet. They conclude that the constraint of a perfectly balanced surface flux budget could be relaxed. High resolution models often do not run into equilibrium, since computational resources are limited and often do not allow multi-century integration. Over the last decade, it has also become clear that fully equilibrated runs are not strictly mandatory for meaningful science (Stewart et al., 2020 and references therein), even though this puts even more emphasis on the understanding of the model's drift behaviour. Additionally, as mentioned above, ensuring climatological surface fluxes poses the greatest technical challenge in the construction of the CNYF dataset. Relaxing this criterion would substantially simplify the construction. Consequently, Stewart et al. (2020) propose a RYF dataset to serve as a climatological forcing that would meet the following criteria:

1. Unaltered subset of JRA55-do
2. Full seasonal cycle is retained
3. High-frequency forcing is retained, including consistency between fields
4. Smooth transition period without violating criteria 3
5. Quasi-climatological with neutral climate indices
6. Periods from which subsets are taken should be recent to fall within the satellite era (post 1970s) but be affected by global warming as little as possible

In order to fulfil these criteria as good as possible, they propose the following approach. They use three climate indices, SOI, NAO and SAM, which are all based on sea level pressure and therefore directly derivable from the atmospheric data, to identify "neutral" years. They suggest three candidates: 1984, 1990, 2003 (Fig. 3.1). Furthermore, the transition is moved from December-January to April-May² in order to avoid periods of strong atmospheric variability in high latitudes during winter.

Stewart et al. (2020) provide a detailed assessment, build on several ocean models, of these three RYF-periods in terms of ocean model drift. Their main aim is to identify RYF-periods that can be used for long-term ocean model spin-up integrations. Although, they generally recommend using the RYF90-period, they find the differences between experiments forced with these three periods small compared to inter-model differences. They therefore judge the choice of a specific year as not critical. However, the choice might depend on the specific research question at hand

²Therefore, each RYF-period includes months from two years, but I will refer to them as RYF84, RYF90 and RYF03 to identify these periods unambiguously.

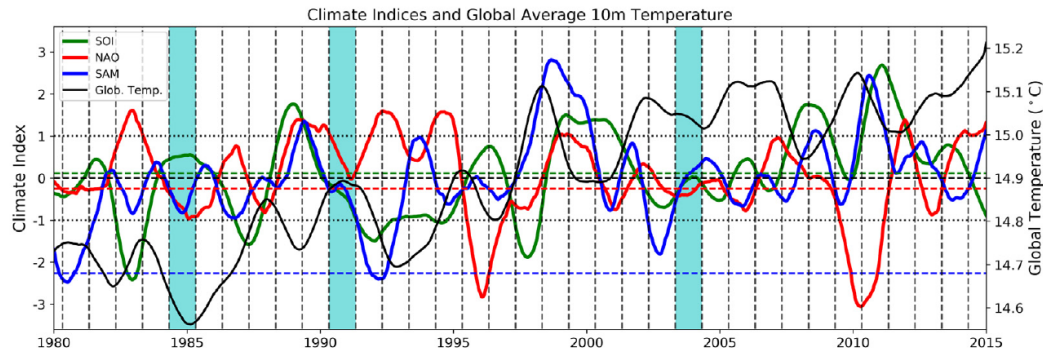


Fig. 3.1.: Timeseries of 12-month running mean of major climate indices – Southern Oscillation Index (SOI), North Atlantic Oscillation (NAO), and Southern Annular Mode (SAM). The global surface air temperature is shown in black, and the average SOI, NAO and SAM indices of the CORE-NYF are shown in dashed green (0.11), red (-0.25) and blue (-2.26), respectively. Vertical dashed lines indicate May 1, and the three cyan bands indicate the three candidate years, RYF84, RYF90 and RYF03 (from Stewart et al. 2020).

and, since they find inter-model difference to be large, also on the OGCM itself.

Indeed, the model setup used in this thesis differs from the ones analysed in Stewart et al. (2020). They use three OGCMs with a spatial resolution of 1° (two configurations offer increased resolution of about 0.3° in the equatorial domain), which they integrate for 500 years in order to ensure an equilibrated state. In contrast, the models used here have a spatial resolution of 0.25° globally but are only integrated for about 90 years (including a 30 year spinup-phase). Consequently, we can not expect to reach an equilibrated model state and the purpose of climatological experiments in the context of this study is different. While Stewart et al. (2020) aim to provide a spun-up ocean that can be used as an initial condition for further experiments, the focus in this chapter lies on the characterization of the model's adjustment towards an equilibrated state and spurious trends due to ocean–atmosphere flux imbalances or model deficiencies. In order to analyse the hindcast experiments, meant to reproduce observed variability, we need a proper characterization of these trends.

In summary, the aim of this chapter is to compare the three RYF-candidates, identified by Stewart et al. (2020), but with the specific model setup used in this thesis, and a different focus. Specifically, the following chapter will:

- compare the model adjustment processes and drifts over one hindcast period and assess whether, or which, RYF-experiments are representative for the behaviour of the hindcast.

- identify causes and mechanism for model drift and quantify spurious trends in hindcast experiments.

3.3 Ocean models

This chapter will make use of six experiments introduced in detail in chapter 2.1. The main set of four experiments uses JRA55-do forcing and another set of two runs utilizes the CORE.v2 dataset:

- RYF84: repeated-year-forcing experiment using the RYF84-period.
- RYF90: repeated-year-forcing experiment using the RYF90-period.
- RYF03: repeated-year-forcing experiment using the RYF03-period.
- HC-JRA: Reference run forced with interannually varying JRA55-do forcing.
- CNYF: Climatological experiment forced with CORE Normal Year Forcing.
- HC-CORE: Reference run forced with interannually varying CORE.v2 forcing

Both sets (forced with either JRA55-do or CORE.v2) are consistent among their members regarding model parameter and initialization and only differ with respect to the atmospheric forcing (i.e. climatological or interannual forcing). However, there are differences between both sets (see chapter 2.1 for details) which are pointed out below as they become relevant.

3.4 Results

The evolution of globally averaged temperature and salinity is analysed below. This is useful for two reasons. First, to assess if the experiment reaches an equilibrated state. If the thermodynamic properties show a continued drift, other integrated measures that are of more immediate interest, like the global overturning circulation for example, are likely to be affected as well. Second, comparing temperature and salinity drift among all climatological experiments and their relation to globally integrated surface heat and freshwater fluxes allows to attribute these trends to either surface flux imbalances or model deficiencies.

An initial decline of globally averaged temperature is found in all four JRA-experiments (Fig. 3.2). RYF90, RYF03 as well as HC-JRA show only very weak trends at the end of the integration, with temperatures around 2.82°C (Fig. 3.3a). Temperature

	RYF84	RYF90	RYF03	CNYF	HC-JRA	HC-CORE
Trends per decade						
T (10^{-3} K)	-8.0	-2.5	-1.4	-1.2	-2.4	3.0
S (10^{-4} psu)	-3.0	-2.9	-3.4	-0.1	-3.9	-4.1
SST (10^{-3} K)	-4.7	-2.6	-3.0	-1.8	79.5	53.0
SSS (10^{-4} K)	-67.1	-46.5	-59.8	-7.1	16.7	-61.2
HF (10^{13} W)	5.4	2.8	3.4	3.6	5.9	7.9
FWF (10^4 kgs $^{-1}$)	-9.8	-6.6	-5.9	-1145.2	13.8	-6359.8
Subsurface (1000 m) trends (per decade)						
T (10^{-3} K)	-30.8	-22.6	-14.4	-9.9	-20.4	-0.1
S (10^{-4} psu)	-20.3	-23.6	-22.3	-21.5	-22.6	-23.5
Transport trends (Sv per decade)						
AMOC (35 years)	-0.38	-0.36	-0.63	-0.22	-1.14	-0.31
ACC (40 years)	-2.24	-2.05	-1.40	-2.88	-0.18	-0.48
Total ITF	-0.34	-0.30	-0.58	-0.44	-0.51	-0.64
Wind driven ITF	0	0	0	0	0.08	0.11
Pacific upwelling	-0.32	-0.29	-0.63	-0.49	-0.61	-0.74

Tab. 3.1.: Linear trends over the last 50 years (unless stated otherwise) of each experiment of globally averaged temperature (T), salinity (S), SST, SSS, turbulent heat flux (HF), turbulent freshwater flux (FWF), transport of AMOC, Antarctic Circumpolar Current (ACC) across Drake Passage, Indonesian Throughflow (ITF) measured at 115° E between Australia and Indonesia. The wind driven ITF is computed according to the amended Island Rule (see section 3.3). Pacific upwelling conforms to vertical transport at 1500 m, north of 44° S.

trends in RYF84 are strongest and lead to the lowest temperature of all available experiments at the end of the integration period of about 2.78°C . Global mean temperature are highest in CNYF with about 2.84°C and only weak negative trends at the beginning of the integration and slightly increasing temperatures after 1990. The evolution of temperature in HC-CORE follows the curve of CNYF, until the early 90s, when temperature starts to increase. As expected, interannual variability is stronger in both hindcasts.

Globally averaged SST trends in all climatological experiments are of similar magnitude as for the global mean temperature (Tab. 3.1). In Fig. 3.2 b) this is however masked by the much stronger interannual variability and strong positive trends in

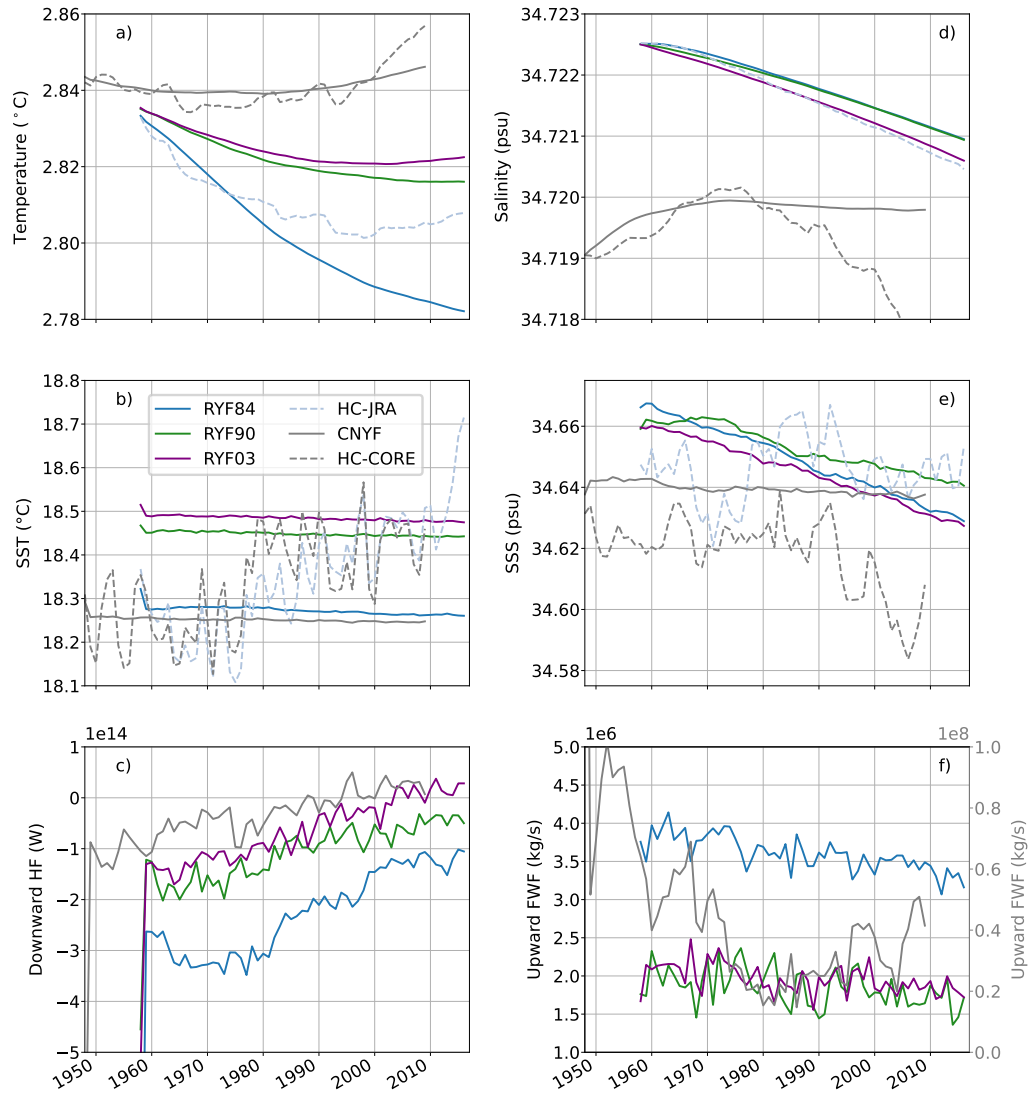


Fig. 3.2.: Timeseries of globally averaged (a) temperature and (b) sea surface temperature (SST) and (c) global sum of downward ocean-atmosphere heat flux (HF). Globally averaged (d) salinity and (e) sea surface salinity and (f) global sum of upward freshwater flux (FWF). All quantities are given for all six experiments, except for the surface fluxes (c and f) where results from both hindcasts are neglected because their strong interannual variability would mask the drift of the climatological experiments. Their results are instead deferred to Fig. A.1. Note the two scales of panel (f).

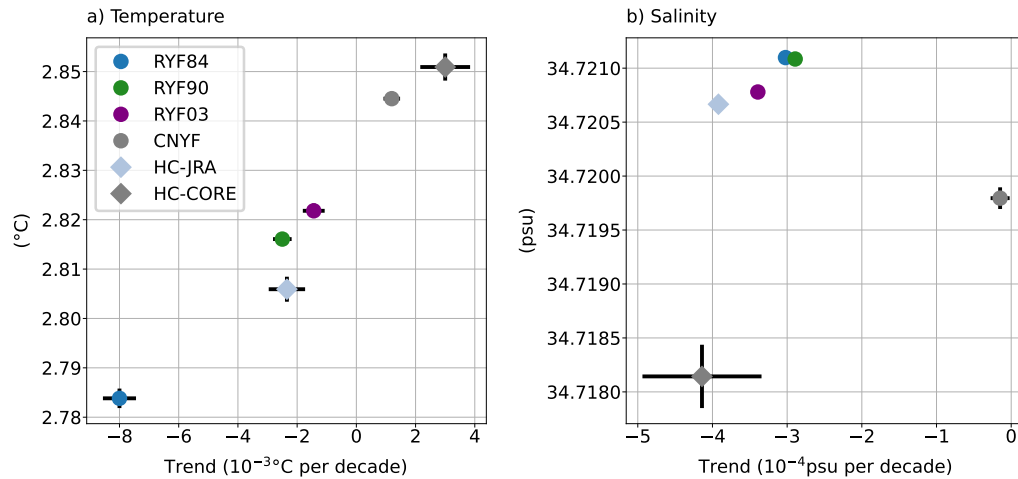


Fig. 3.3.: Mean over the last ten years of each experiment and linear trend over the last 50 years of each integration of globally averaged (a) temperature and (b) salinity. Horizontal and vertical bars give 99 % confidence intervals and interannual standard deviation, respectively. Bars are omitted where the represented quantities are too small for the bars to exceed the marker itself.

both hindcast experiments. Again, RYF03 shows the warmest and RYF84 the coldest temperatures among the RYF-experiments. Interestingly, SSTs in CNYF are colder than in all RYF-experiment, indicating a more efficient downward heat flux from the upper into the deep ocean in the CORE-experiment.

The temporal evolution and inter-model differences of the global mean temperature is related to the turbulent surface heat fluxes (Fig. 3.2 c). Heat fluxes are initially upward in all four climatological experiments but weakest in CNYF. Their absolute values are similar in RYF90 and RYF03 and strongest in RYF84. All climatological experiments, except for RYF84, reach an approximate heat flux balance around 0W, which is consistent with the continued temperature drift in RYF84. Note, that a separate figure (Fig. A.1) is reserved for the heat fluxes of both hindcasts because their strong interannual variability would effectively mask the trends of the climatological experiments. In summary, the evolution of globally averaged temperature is consistent among all RYF-experiments and characterize the behaviour of HC-JRA at least qualitatively. Quantitative differences are related to the atmospheric heat flux forcing that is strongest for RYF84 and produces the strongest temperature decline.

The evolution of globally averaged salinity differs between JRA55-do and CORE.v2 experiments (Fig. 3.2 d). All three RYF-experiments and also JRA-HC show a negative drift of 2.9 to 3.9 x 10⁻⁴ psu per decade (Fig. 3.3 b). Salinity in CNYF is stable

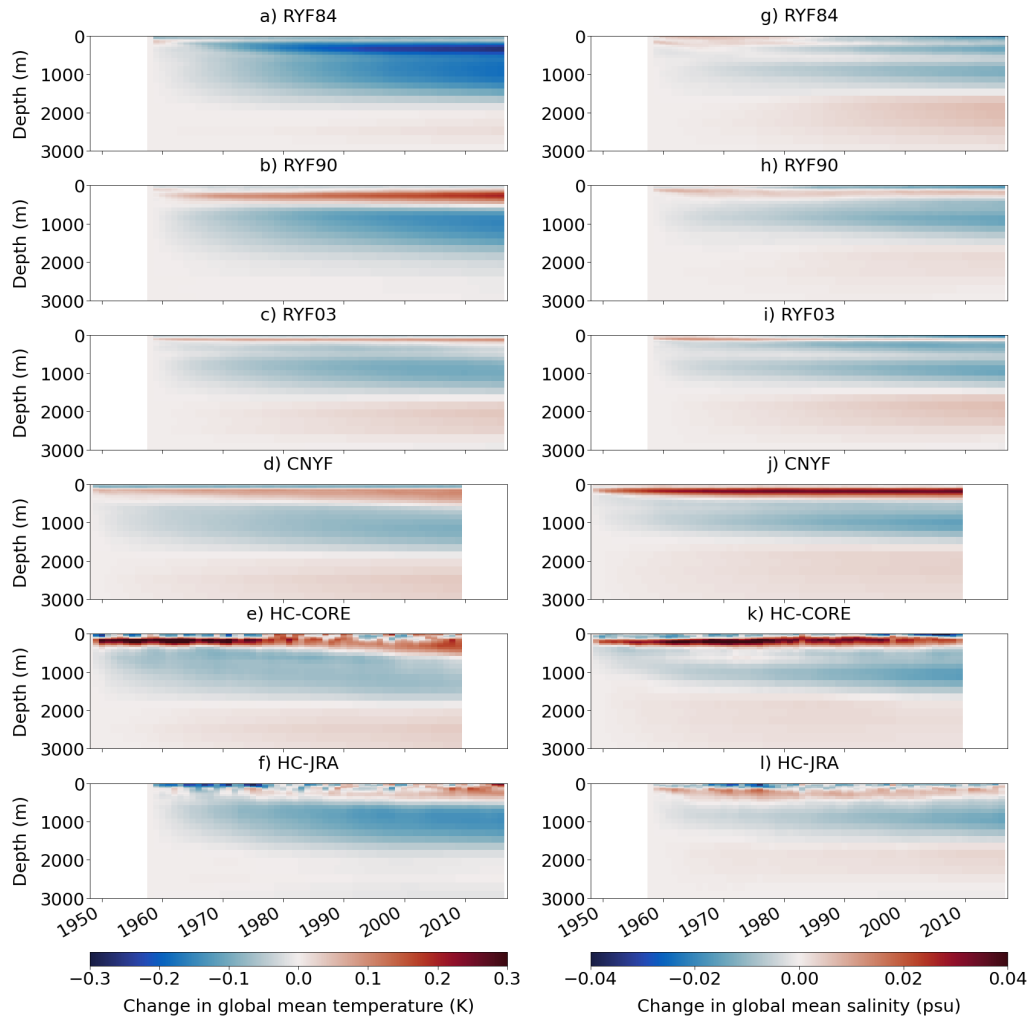


Fig. 3.4.: *The depth dependent change in global mean temperature (a-f) and salinity (g-l) referenced to the initial conditions for the six experiments.*

after an initial adjustment of about 20 years, while salinity in CORE-HC closely follows the climatological experiments for about 30 years, after which it starts to decline. Evolution of sea surface salinity (SSS) in the climatological experiments is consistent with the behaviour of total salinity, but trends are stronger by about one order of magnitude (Tab. 3.1) and long-term trends in both hindcasts are masked by strong interannual variability (Fig. 3.2 e).

Freshwater fluxes are upward in all climatological experiments, but much larger and with stronger variability in case of CNYF (note the different scales in Fig. 3.2 f). The most likely reason for this difference is the freshwater budget correction (FWBC) applied only to the JRA-experiments. The FWBC artificially forces the freshwater

fluxes to zero every three hours (the temporal resolution of the forcing) by modifying the fluxes accordingly. It is noteworthy that all climatological experiments freshen despite a loss of fresh water to the atmosphere. Again, fluxes from both hindcast are moved to the appendix (Fig. A.1). Unlike the temperature drift, surface fluxes imbalances can not explain salinity trends but require further investigation.

The vertical structure of globally averaged temperature and salinity changes is very similar among all experiments (Fig. 3.4). Between depth of 500 m and 2000 m, all climatological experiments suggest negative temperature and salinity trends. At 1000 m depth, these range from -9.9×10^{-3} to -30.8×10^{-3} K per decade and -21.5×10^{-4} to -23.6×10^{-4} psu per decade (Tab. 3.1). Differences are mainly limited to the upper 500 m where the evolution depends on the atmospheric forcing and trends differ even in sign. This structure is also found in both hindcast experiments, but with much stronger upper ocean variability. Note, in particular, the strong positive salinity trends in the upper ocean in both CORE.v2 simulations, which are consistent with strong upward freshwater fluxes noted above. They compensate the negative trends in the deep ocean, which are present in all simulation.

In order to identify the processes involved in the temperature and salinity drifts, it is useful to analyse their spatial distribution. Figure 3.5 maps temperature and salinity trends at 1000 m depth. All experiments, climatological as well as hindcast produce the strongest cooling in the North Atlantic and also in the Indian Ocean and the Pacific section of the Southern Ocean. The North Pacific and, except for RYF84, also the South Atlantic warm in all experiments. The spatial pattern of salinity trends is very robust across all experiments. Negative salinity trends are found in the North Atlantic and the Indian Ocean, in particular the Bay of Bengal, while the subtropical and tropical Atlantic, the Pacific domain of the Southern Ocean and the North Pacific are characterized by positive trends.

Although the inter-model differences in terms of temperature drift can be related to differences in the heat flux forcing, the spatial patterns, in particular the cooling and freshening in the Bay of Bengal, are robust over all simulations and appear to be rather independent of the atmospheric forcing. This leads to the conclusion that they are due to model deficiencies rather than shortcomings of the forcing. The robust dipole pattern in the Atlantic, with cooling and freshening in the north and warming and salinification to the south, suggests a weakening of the Atlantic Meridional

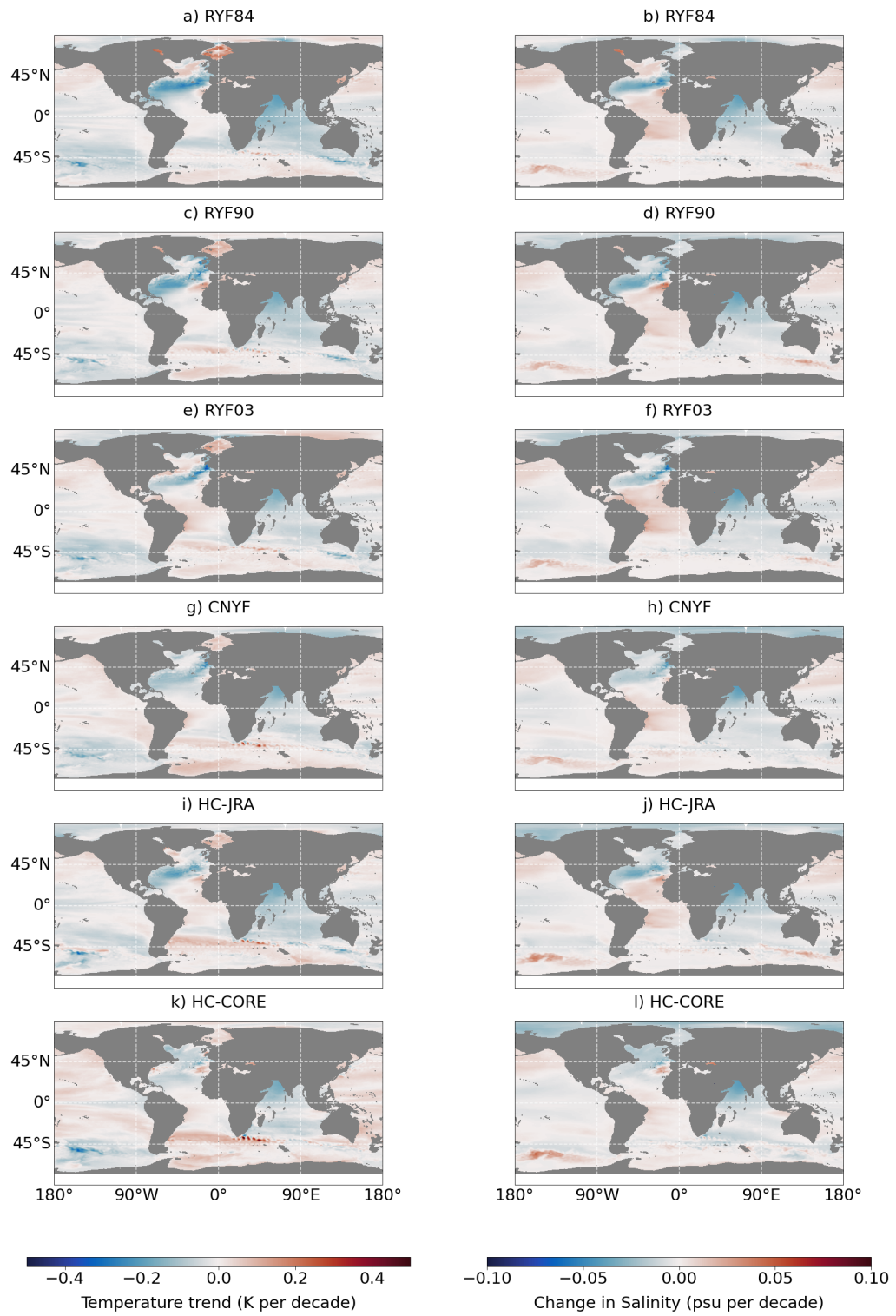


Fig. 3.5.: Trends over the last 50 years of each integration of (a-f) temperature and (g-l) salinity at 1000 m depth.

Overturning Circulation (AMOC), that would reduce the northward transport of warm and saline waters in the Atlantic.

3.4.1 Atlantic Meridional Overturning Circulation

The AMOC weakens in all experiments, at least over the last four decades of the integrations. (Fig. 3.6). All climatological experiments show an initial strengthening, which is more pronounced in the RYF-experiments where the peak is reached after 15 to 20 years, followed by a reduction. No negative AMOC-trends are found in RYF84 and RYF90 during the last ten years of their integration, suggesting that they might have reached a stable state. RYF03 and CNYF continue to decline. Averaged over the last ten years of the experiment, RYF90 produces the strongest AMOC (16.4 Sv), followed by RYF84 (15.8 Sv), CNYF (15.4 Sv) and RYF03 (12.5 Sv). It is striking that RYF84 and RYF90 apparently adjust to the same level that HC-JRA reaches during its respective RYF-periods (marked by the dashed lines in Fig. 3.6). RYF03 falls below this level, which supports the conclusion that RYF03 is unable to support a stable AMOC. The continued decline in CNYF is consistent with the increased freshwater input in CNYF compared to the JRA-experiments. However, it does not fall below the climatological mean AMOC value of HC-CORE within the 60 years of its integration, making it difficult to judge its stability. Note that linear trends over the last 35 years of each integration are not significantly different between any of the climatological experiment except RYF90 (Fig. 3.6).

A likely reason for the unstable AMOC in RYF03 is the absence of deep convection in the North Atlantic. RYF03 is the only experiment where averaged mixed layer depth (MLD) during winter do not exceed 1000 m in the Labrador Sea (Fig. 3.7). Both hindcasts and also CNYF produce very similar MLD patterns and amplitudes. RYF84 and RYF90 yield strong deep convection that extends further east than the climatological mean of HC-JRA suggests, which fits that relatively strong AMOC.

3.4.2 Antarctic Circumpolar Current

In the Southern Ocean, the global meridional overturning circulation is directly linked to the ACC which is therefore another key quantity of OGCMs. Past simulations, with CORE.v2 forcing but otherwise similar model setups in terms of model code and resolution, produced unstable ACC transports with decreasing trends

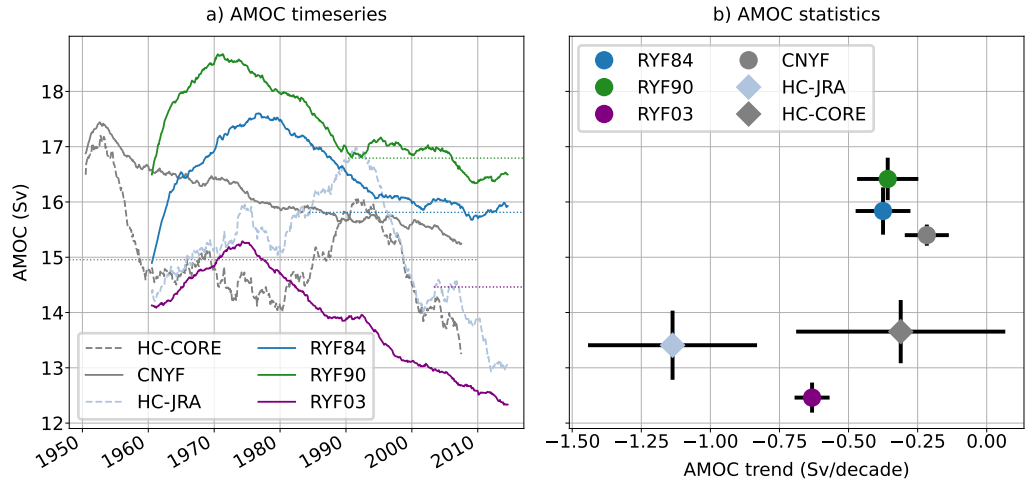


Fig. 3.6.: AMOC transport. (a) timeseries smoothed with a five-year rolling mean for four climatological experiments (solid) and two hindcast experiments (dashed). Dotted lines for each RYF-experiment start at their respective RYF-period and give the value from the hindcast experiment (HC-JRA) averaged over the 12-month period. (b) Mean value for the last ten years of each experiment and trends over the last 35 years of each integration. Horizontal and vertical bars give 95% confidence intervals and deviations, respectively.

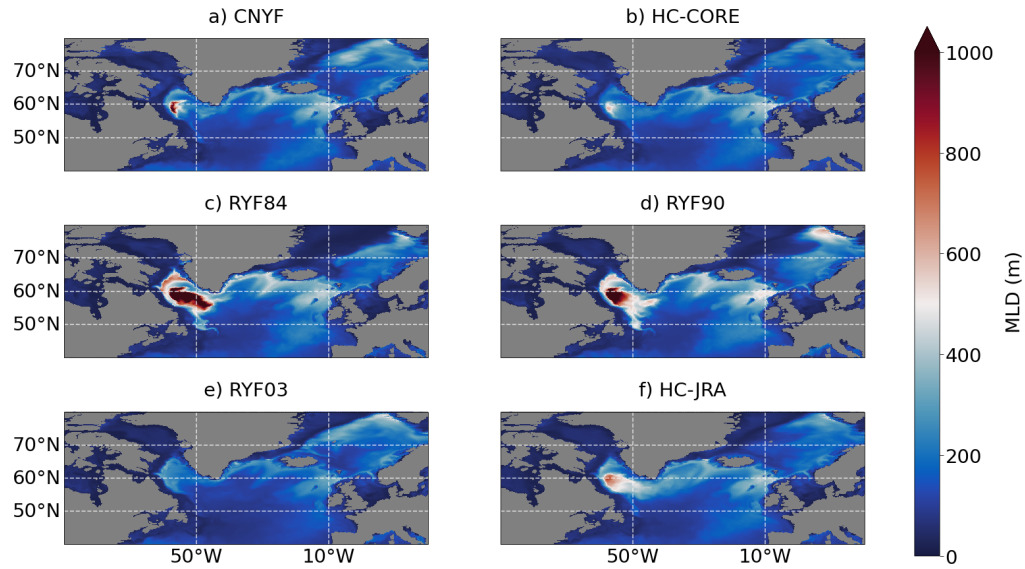


Fig. 3.7.: Mixed layer depth in winter (DJF) averaged over the last ten years of each integration from six experiments.

(Farneti et al., 2015). This is also true for the experiments presented here. The ACC, measured across the Drake Passage, declines in all climatological experiments with trends ranging from -1.4 Sv per decade in RYF03 to -2.9 Sv per decade in CNYF, while trends in both hindcast are weak (Fig. 3.8 a and Tab. 3.1). As for the AMOC-trends, RYF84 and RYF90 yield comparable trend estimates, that do not differ significantly (Fig. 3.8 b).

The baroclinic part of the ACC transport is linked to a meridional density gradient that is characterized by an upward sloping of isopycnals across the major frontal zones. The system is mainly set up by the prevailing westerly wind stress that causes divergent Ekman transport and thereby upwelling, but is also influenced by buoyancy forcing and eddy dynamics. Because the wind stress in the climatological experiments is almost constant on an interannual timescale by definition, wind-stress variations can not account for the simulated ACC trends. Instead, a deep warming in climatological (Fig. 3.8 c; only RYF90 is shown) and hindcast experiments (Fig. 3.8 d: only HC-JRA is shown) causes a reduction of the meridional density gradient across the Southern Ocean (not shown) and the meridional temperature gradient across the ACC is therefore closely correlated to the ACC transport in all climatological experiments. This correlation is much weaker in case of the hindcast experiments because the ACC transport is also affected by wind-stress variability (Fig. 3.8 e; only one hindcast is shown for clarity). Since the underlying mechanism, i.e. the deep warming in the Southern Ocean, is also present in both hindcasts, it seems reasonable to assume that an overall positive ACC trend over the hindcast period is masked by spurious model drift.

It is, however, difficult to quantify this trend, in particular in the case of HC-JRA, where three different trends estimates are available. A linear relationship between some proxy and the ACC transport decline would be useful to quantify the ACC drift of the hindcast experiments. The proxy should be unaffected by direct atmospheric forcing and the temperature drift in the deep Southern Ocean appears to be a promising candidate for the ACC transport. However, inferring a robust relationship from the very small set of climatological experiments turns out to be challenging. Figure 3.8 f) shows the relationship between the deep temperature trends (averaged zonally, from 2000 m to the bottom and from 70°S to 60°S) and the ACC transport trends. The resulting linear regression would not only be very sensitive to the exclusion of any single climatological experiment, but also to the exact choice of the depth and latitudinal range for which the temperature trends are calculated (not shown).

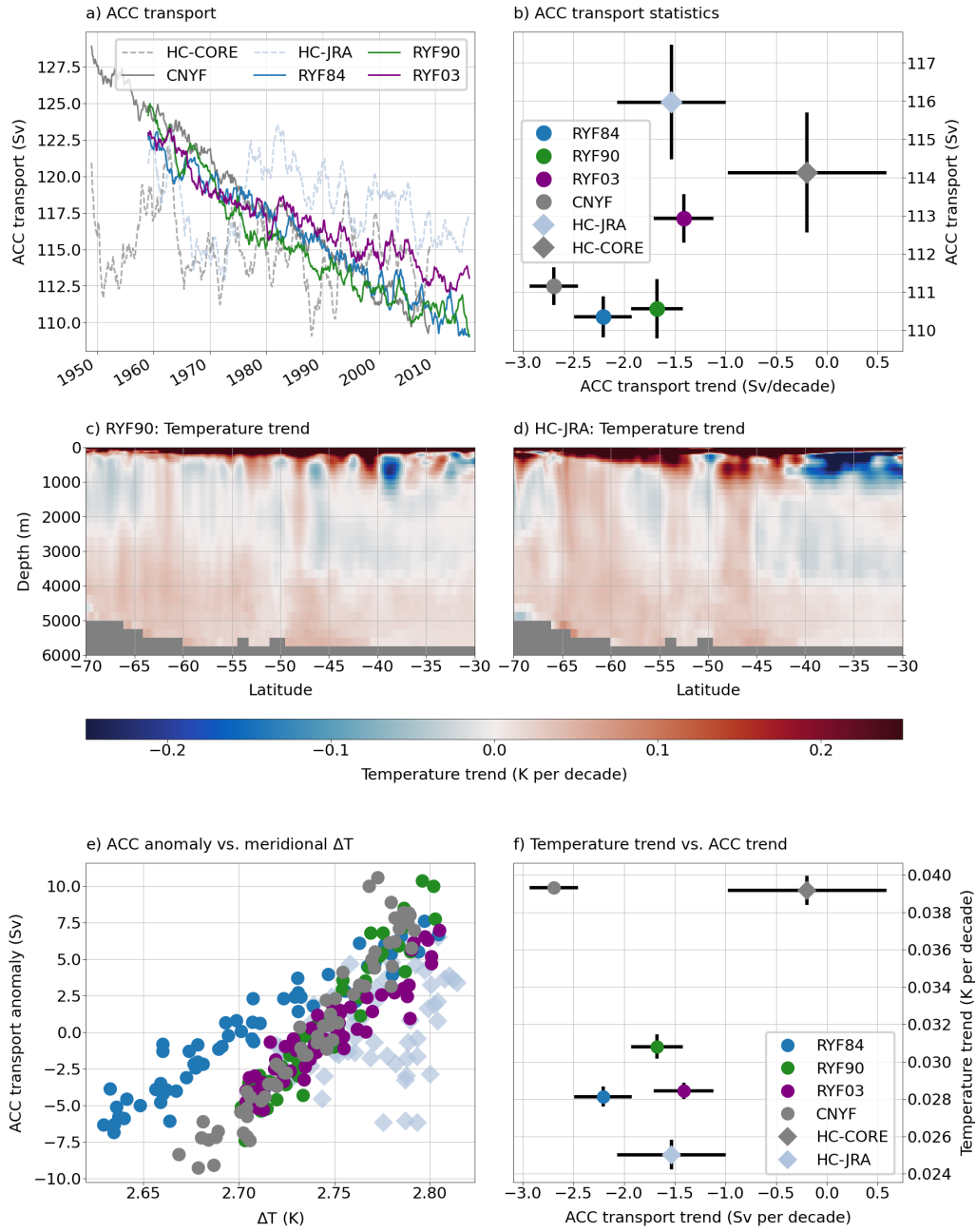


Fig. 3.8.: Decline of ACC transport and meridional temperature gradient. (a) ACC transport across Drake Passage. (b) Mean and trend of ACC transport. Trends of zonally averaged temperature in (c) RYF90 and (d) HC-JRA. (e) ACC transport anomaly vs. meridional gradient of zonally and vertically averaged temperature between 70°S and 30°S. (f) ACC transport trend against the trend of temperature averaged zonally, from 2000 m to the bottom and from 70°S to 60°S. Mean and trends are computed over the last 10 and forty years of the integrations, respectively. Horizontal and vertical bars give 99% confidence intervals and interannual standard deviations, respectively. Bars are omitted where the represented quantities are too small for the bars to exceed the marker itself.

3.4.3 Indonesian Throughflow

Yet another current that is part of the global overturning circulation and of special importance for chapter 4 of this thesis is the Indonesian Throughflow (ITF). It connects the Pacific and Indian Oceans at a tropical latitude and is the only low-latitude connection of ocean basins.

The model allows of course for a direct estimation of ITF transport, but a more indirect approach is useful to identify forcing mechanisms. Velocity observations are sparse in space and time, which is why estimation of ITF transport rely on proxies. The traditional way of computing the wind-stress-driven transport of the ITF is the Island Rule (Godfrey, 1989) and its extensions (Wajsowicz, 1993, 1996; Pedlosky et al., 1997). It is based on the Sverdrup balance and relates the wind stress along a contour, enclosing Australia and running along the eastern boundary of the South Pacific, to the transport around the island. Based on his theory, Godfrey (1989) estimated an ITF transport of around 16 Sv which is very close to today's observational estimates of 15 Sv (Feng et al., 2018). However, Feng et al. (2017) point out that the Sverdrup balance assumes that the ocean is inert below a level of no motion, which is of course not true. Therefore, Feng et al. (2017) amend the Island Rule by an additional term that accounts for deep upwelling across the Pacific:

$$T_{ITF} = -\frac{1}{f_s} \oint_C \frac{\tau^l}{\rho_0} dl + \iint_{Pacific} w_z ds \quad (3.1)$$

where f_s is the Coriolis parameter at the southern end of Australia, τ^l is the along contour wind stress, ρ_0 is the mean seawater density and w_z is the vertical velocity at depth z . The first term on the right-hand side is the classical Island Rule and represents the wind-stress-driven fraction of the ITF. The last term represents upwelling at a depth z across the Pacific north of 44°S that, due to continuity constraints, also contributes to the ITF transport. The reader is referred to Feng et al. (2017) for a detailed derivation. The contour line C is shown in Fig. 3.9. Consistent with Feng et al. (2017), upwelling is computed at $z = 1500$ m, which represents the boundary between the circulation of the upper and the deep ocean (not shown). However, as long as z exceeds the sill depths of 1500 m along the ITF pathway, the exact depth is not critical for the result.

All experiments show negative ITF trends that range from -0.3 Sv per decade in RYF90 to -0.63 Sv per decade in HC-JRA (Fig. 3.10 a, Fig. 3.11 and Tab. 3.1). Once more, RYF03 constitutes an outlier in terms of the linear trend, while RYF84 and RYF90 yield consistent estimates. In order to identify the mechanism that drive

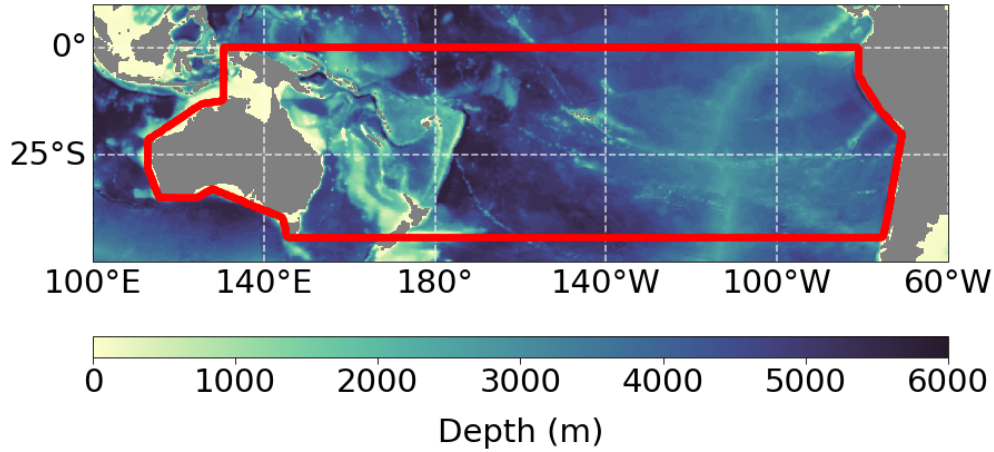


Fig. 3.9.: Contour line C used in equation 3.1 to compute the ITF transport. Colorshading indicates bathymetry.

this negative trend, it is useful to reconstruct the ITF transport using the Island Rule Amendment described above. Although, the reconstructions overestimate the ITF transport by 17 to 25 %, it captures the interannual variability faithfully and also reproduces the trends. Correlations (based on detrended, annually averaged timeseries) with the direct ITF estimates, taken at 115°E between Australia and Indonesia, are above 0.82 for all experiments.

The negative ITF trends in all RYF-experiments and also in CNYF are not explained by the wind-stress-driven component, which show no trends at all. Instead, they are due to a reduction of vertical transport, i.e. a reduction of deep Pacific upwelling (Fig. 3.10 and Tab. 3.1). The trends in both hindcasts can be understood as a combination of both mechanisms. The wind drives weak positive trends of 0.08 and 0.3 Sv per decade in HC-JRA and HC-CORE, respectively, which are exceeded by strong negative trends due to the reduced upwelling, resulting in a total decline of ITF transport. It is tempting to use the upwelling trends to estimate the spurious trend in both hindcast. However, the upwelling trends in both hindcast tend to be stronger than in the respective RYF and CNYF experiments. This could indicate a realistic signal on top of the spurious trends, which might be worth investigating.

ITF transport variability is small ($SD < 0.37$ Sv) in all climatological experiments and due to intrinsic variability of the Pacific overturning (Fig. 3.10). Note, that the strength of the wind-stress-driven ITF in each RYF-experiment corresponds to the strength of HC-JRA during the respective RYF-period. The total transport variability

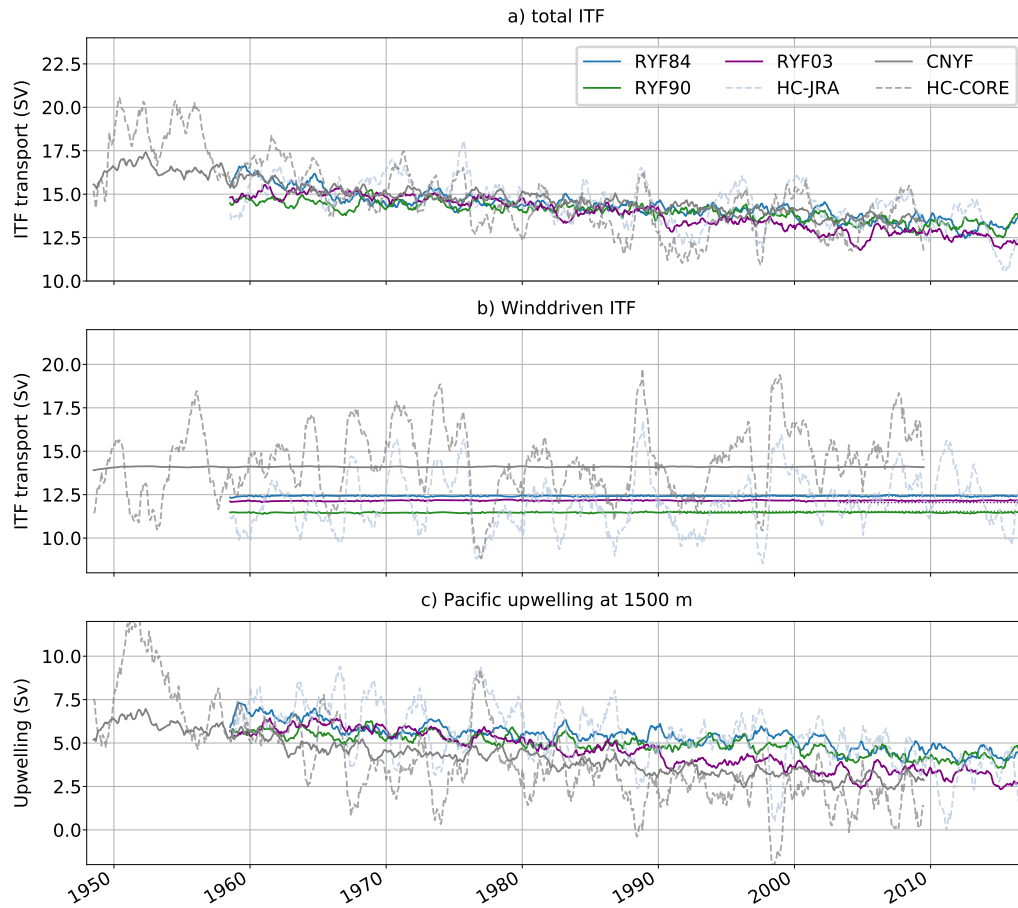


Fig. 3.10.: Decomposition of (a) total ITF transport into components driven by (b) direct wind-stress forcing and by (c) upwelling in the Pacific north of 44°S . Note that the range of the y-axis is the same in all panels to facilitate a visual comparison of the variability.

in both hindcast experiments amounts to 1.1 Sv and 1.5 Sv in HC-JRA and HC-CORE, respectively, and is precisely captured by the linear combination of wind driven transport and upwelling (not shown). Although the total transport is correlated to the wind-stress-driven part (correlation coefficient of 0.6 for both hindcasts) the latter overestimates the amplitude of the variability by 45 % and 33 % in case of HC-JRA and HC-CORE, respectively. The transport due to Pacific upwelling is anti-correlated to the wind driven transport (correlation coefficient of -0.76 and -0.72 in HC-JRA and HC-CORE, respectively) and causes a partial compensation (compare panels b and c of Fig. 3.10). The issue warrants further investigation, but will not be addressed any in this thesis.

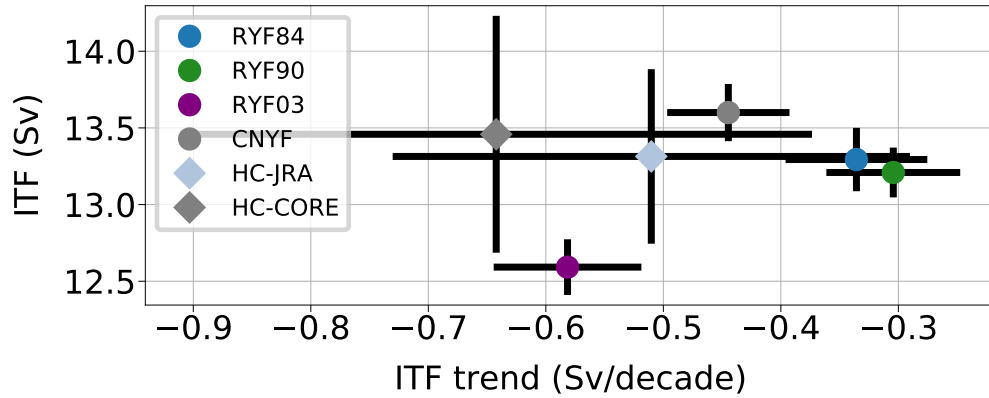


Fig. 3.11.: *ITF transport statistics. Mean over the last ten years of each experiment and linear trend over the last 50 years of each experiment. Horizontal and vertical bars give 95 % confidence intervals and interannual standard deviation, respectively.*

3.5 Estimation of spurious trends in hindcast experiments

As pointed out in the introduction, a major motivation to conduct climatological experiments is to quantify spurious model trends. Typically, the drift of a climatological experiment is assumed to represent the spurious drift. But the RYF-approach does not provide one but several (three in this case) climatological forcings and every RYF-experiment yields a (slightly) different trend. One way to deal with this issue is to reduce the number of estimates using physical and statistical arguments. The timeseries of ITF transport shall serve as a first example. RYF-experiments give trend estimates between -0.3 and -0.58 Sv per decade, of which two are not significantly different (on a 95% confidence interval). An argument to disregard the strong negative trend of RYF03 could be the fact that previous studies (Feng et al., 2017) suggest a reduction of ITF transport due to a slowdown of deep Pacific upwelling with global warming and that the global mean temperature of the RYF03-period already includes a global warming signal (Fig. 3.1). Averaging the two remaining estimates of RYF84 and RYF90 gives -0.32 Sv per decades of spurious ITF drift.

A similar approach works in case of the AMOC trends. As pointed out above, RYF03 does not produce deep convection and is therefore unable to support a stable AMOC. RYF84 and RYF90 give consistent estimates in terms of mean transport strength and trends that can be averaged to get a single estimate.

This approach fails in the case of the ACC where trend estimates vary between -1.4 and -2.24 Sv per decade. Although RYF03 may be considered to be an outlier in a statistical sense (Fig. 3.8 b), there is no obvious physical argument to exclude it. The meridional density gradient across the ACC is predicted to strengthen with global warming due to a warming of the ocean north of the ACC, but neither is it certain that this will cause a strengthening of the ACC (Stocker et al., 2013), nor does the stronger ACC transport in RYF03, compared to RYF84 and RYF90, seem to be caused by a stronger meridional density gradient (not shown). The RYF84-period on the other hand is characterized by a negative SAM index, which Stewart et al. (2020) conclude to be the cause for a very weak ACC transport in their experiments. However, we find the ACC transport in RYF84 only to be 1.2 Sv below RYF90. Averaging the trends of all three RYF-experiments seems to be the most justified approach in this case.

Another option tested above is to use the RYF-experiments to establish a linear relationship between a proxy and the variable of interest to quantify a spurious trend in the hindcast experiment. Although, the RYF-experiments allow to identify the mechanism behind the spurious drift of a particular quantity, the approach turned out to be unsuccessful for the examples presented here. In the case of the ITF transport, the temporal evolution of the potential proxy, i.e. the deep upwelling, is not exclusively spurious. In the case of the ACC transport, identifying a robust relationship based on a set of only four experiments turned out to be difficult.

One last notion in this respect: even if a robust trend can be inferred, there is no obvious way of obtaining an estimate of the uncertainty. This applies to both, the NYF and RYF, approaches. One might be tempted to consider multiple RYF-realizations as a small ensemble and infer an uncertainty from the ensemble spread. However, one should be aware that three realization are far from being sufficient and that the result should be considered to be a lower bound at best.

3.6 Summary and conclusion

In this chapter, the recently introduced approach of a repeated year forcing with JRA55-do is evaluated. The ability of three different RYF-experiments with JRA55-do forcing to characterize the model drift and transients over a typical hindcast period are tested. Specifically, a range of integrated quantities and key transport of the

global circulation are compared among those RYF-simulations, a NYF-experiment under CORE.v2 forcing and two hindcasts with interannually varying forcing from both forcing products.

The global mean temperature in all, climatological as well as hindcast, experiments evolves similarly. However, all experiments adjust to slightly different mean states. These different states are determined by the atmospheric forcing and depend on the energy input via turbulent heat fluxes. A continued temperature drift at the end of the integration is found only in RYF84. This is somewhat in contrast to results of Stewart et al. (2020), who find a continued negative temperature drift in almost all experiments over the full 500-year integration cycle. The integration of a second cycle could clarify whether the experiments presented here do indeed reach a balanced heat flux budget. The (initial) negative temperature drift is mostly due to decreasing temperatures in the North Atlantic and the northern part of the Indian Ocean at depths between 500 and 2000 m. These negative deep trends are found in all experiments but are partially compensated by positive trends in the upper 500 m in RYF90 and RYF03 but amplified by negative trends in RYF84.

Globally averaged salinity evolves differently in JRA and CORE-experiments. While CNYF reaches an equilibrium after about 20 years, salinity continuous to decline in all RYF-experiments. Again, this decline is driven by salinity anomalies at depth between 500 and 1500 m in the North Atlantic and the northern Indian Ocean and also present in the CNYF experiment. However, in case of CNYF this decline is compensated by surface freshwater fluxes, resulting in a stable freshwater budget. The FWB correction, meant to ensure a balanced freshwater budget, dampens surface freshwater fluxes in all JRA-experiments preventing them from balancing the deep salinity trends, which results in a total gain of fresh water. In comparison, Stewart et al. (2020) find stable salinity after an initial adjustment of less than 10 years in three out of two simulations (independent of the RYF-period used). The remaining model does also use a global FWBC (Stewart et al., 2020; Danabasoglu et al., 2016) and shows trends that are very similar to the ones reported here. However, it is unclear whether the models with stable salinity employ a FWBC or not. In any case, for future experiments, the use of a FWBC should clearly be revisited.

In addition to the global evolution of temperature and salinity, this chapter presented a series of key transport time series and analysis of their temporal evolution in order to assess the suitability of the different RYF-periods.

Only RYF84 and RYF90 produce a stable AMOC transport at the end of the integration, while RYF03 yields a continued decline due to a lack of deep convection in the Labrador Sea during boreal winter. Stewart et al. (2020) report a similar tendency: although all RYF-experiments produce deep convection ($MLD > 1000$ m) it is weakest in RYF03. Consequently, they also find a steep decline of AMOC transport (8-10 Sv) over the first 50 years of their RYF03-integrations in two of their three models (the data is unavailable for the third experiment), and a subsequent recovery over the course of the 500-year integration period. Even though, there is no sign of a reduced decline of the RYF03-AMOC presented here, a similar behaviour can not be excluded. Again, a second cycle of integration could shed light on this issue. Furthermore, it is remarkable that the equilibrium of RYF84 and RYF90 (that yield stable AMOC transports) corresponds to the value given by HC-JRA averaged over the respective RYF periods. In comparison, except for a slight initial increase, AMOC transport in CNYF continuous to decline throughout the integration which might be related to the strong freshwater input, that is not dampened by any FWBC.

A decline of ACC transport in all climatological experiments is caused by a deep warming in the Southern Ocean that acts to reduce the meridional density gradient across the Southern Ocean. This warming is also present in both hindcast experiments, but corresponding ACC transport trends are not apparent and most likely masked by opposing trends due to the atmospheric forcing. This is in line with results from Stewart et al. (2020) who find an initial decline of Drake Passage transport over the first 60-100 years in all experiments, with the decline being strongest in RYF84-experiments and weakest in RYF03.

ITF transport in the model is driven by direct wind-stress forcing and deep Pacific upwelling, with the latter being the driver of intrinsic variability and of a decline in all climatological experiments.

3.6.1 Recommendation for a single RYF-period

The selection of a single RYF-period, rather than three, would greatly reduce the time, effort and computational costs needed to conduct experiments and the purpose of this chapter is to support an informed choice on which period is suited best. First, the results presented above suggest that no period is entirely unsuited for a RYF-experiment. All periods supported a successful integration with no fundamental

differences. That is, the behaviour of all RYF-experiments is comparable in terms of mean states and trends and can be used to characterize spurious model behaviour at least qualitatively. RYF03 produced the largest deviation for two reasons. First, the period does not support deep convection in the North Atlantic, which caused the AMOC in RYF03 to collapse. Second, as also pointed out by Stewart et al. (2020), atmospheric global mean temperature in the year 2003 includes a global warming signal. This could affect model trends and is a likely reason for the strong ITF trends in the data presented here. RYF03 can therefore be considered the least suitable candidate. RYF84 is the only RYF-experiment with a continued decline of global mean temperatures by the end of its integration because upward turbulent heat fluxes are strongest. However, this might also be due to the spinup strategy because the difference in atmospheric global mean temperature to the restart condition of 2009 is strongest in 1984. This effect could be mitigated by adapting the spinup strategy as discussed below. Note that Stewart et al. (2020) recommend using the RYF90-period rather than RYF84-period because they find very weak Drake Passage and Kurushio transport in their RYF84-experiments. A result that can not be confirmed with the model setup used here. Accordingly, the results presented here support dismissing the RYF03-period as candidate for RYF-experiments but do not justify a preference of either RYF84 or RYF90. One last comment in this regard: the difficulty in choosing an appropriate RYF-period raises the question about the uncertainty that is associated with the CNYF approach. Assuming the model parameters of the CNYF and RYF-experiments were comparable (which is not true here), one might consider the CNYF forcing an additional realization of the small RYF-ensemble.

3.6.2 Future RYF-experiments

For future RYF-experiments, a changed integration strategy should be considered. As described in section 2.1, all RYF-experiments are restarted from a 30-year spinup (1980-2009) using the interannually varying JRA55-do forcing, that is meant to allow the model to reach an equilibrium, at least in the upper ocean. This approach is based on the established spinup-strategy for hindcast simulation. This also makes sense for CNYF-experiments where the "Normal Year Forcing" and the interannually varying dataset would force the model towards the same climatological state. With the RYF-approach however, this produces a shift of the climatological mean state of the forcing between the spinup-period and the actual experiment. In fact, this is somewhat in contradiction to the purpose of the spinup-period. This might be the reason why global mean temperature in CNYF does not drift, whereas the RYF-

experiments need at least 30 years to reach a neutral state. As an alternative, all RYF-experiments should start from rest but be integrated for additional 30 years. The downside is, of course, that this strategy is more expensive since each RYF-experiment requires its own spinup-integration. Furthermore, it is recommended to integrate RYF-experiments for at least 150 years whenever possible. In particular, global mean temperature and AMOC did only reach a stable state towards the end of the integration. To assess whether the state is indeed stable, an extended integration is needed. This argument is supported by results from Stewart et al. (2020), who demonstrate that an initial adjustment takes between 50 and 100 years for most quantities.

Contribution of buoyancy fluxes to tropical Pacific sea-level variability

This chapter addresses the second research question stated in the introduction and presents an analysis of the impact of buoyancy fluxes on tropical Pacific sea-level anomalies. It makes use of the sensitivity experiments WIND and BUOY that are both based on the RYF-approach, evaluated in the last chapter.

Because only a subset of the OGCM experiments introduced in chapter 2 is used here, the naming is adapted, and all experiments are labelled with the prefix "O025" to indicate their spatial resolution:

HC-JRA: O025-HC

WIND: O025-W90

BUOY: O025-B90

RYF90: O025-RYF90

Markus Scheinert provided the model output of the experiment HC-JRA.

This chapter has been published in the Journal "Ocean Science":

Wagner, P., Scheinert, M., and Böning, C. W.: Contribution of buoyancy fluxes to tropical Pacific sea level variability, Ocean Sci., 17, 1103–1113, <https://doi.org/10.5194/os-17-1103-2021>, 2021.

4.1 Abstract

Regional anomalies of steric sea level are either due to redistribution of heat and freshwater anomalies or due to ocean–atmosphere buoyancy fluxes. Interannual to decadal variability in sea level across the tropical Pacific is mainly due to steric variations driven by wind-stress anomalies. The importance of air–sea buoyancy fluxes is less clear. We use a global, eddy permitting ocean model and a series of

sensitivity experiments with quasi-climatological momentum and buoyancy fluxes to identify the contribution of buoyancy fluxes for interannual to decadal sea-level variability in the tropical Pacific. We find their contribution on interannual timescales to be strongest in the central tropical Pacific at around 10° latitude in both hemispheres and also relevant in the very east of the tropical domain. Buoyancy flux forced anomalies are correlated with variations driven by wind-stress changes, but their effect on the prevailing anomalies and the importance of heat and freshwater fluxes vary locally. In the eastern tropical basin, interannual sea-level variability is amplified by anomalous heat fluxes, while the importance of freshwater fluxes is small and neither has any impact on decadal timescales. In the western tropical Pacific, the variability on interannual and decadal timescales is dampened by both heat and freshwater fluxes. The mechanism involves westward-propagating Rossby waves that are triggered during El Niño–Southern Oscillation (ENSO) events by anomalous buoyancy fluxes in the central tropical Pacific and counteract the prevailing sea-level anomalies once they reach the western part of the basin.

4.2 Introduction

Sea level is an integrated measure that contains information about the water column as well as about ocean–atmosphere interaction. Global mean sea-level (GMSL) variability is usually separated into two processes: changes in the ocean’s total mass due to redistribution of water between the ocean and the atmosphere, land or cryosphere and changes in the density of the water column which are associated with changes in subsurface temperature and salinity distributions. Sea-level variability is not spatially uniform (e.g. Stammer et al., 2013). Instead, it is influenced by ocean dynamics that act to redistribute ocean mass, heat and fresh water (e.g. Zanna et al., 2019). These redistributions leave the GMSL unaffected but can have strong impacts on regional scales rendering the spatial patterns of sea-level variability highly non-uniform (e.g. Merrifield and Maltrud, 2011). Ocean–atmosphere heat and freshwater fluxes can additionally modulate spatial patterns of sea-level variability (e.g. Piecuch and Ponte, 2012; Forget and Ponte, 2015).

The tropical Pacific is a prominent example of an area where regional sea-level variability substantially deviates from the GMSL. Between 1993 and roughly 2012 sea-level rise in the western part of the basin was three times as strong as the global mean rate while the eastern basin saw no or even negative trends. These anomalies have been attributed to gradually increasing trade winds since the early 1990s

(Merrifield and Maltrud, 2011). As such, they are part of a multidecadal pattern of variability that can be related to climate modes such as Pacific Decadal Oscillation (PDO) or El Niño–Southern Oscillation (ENSO) (Merrifield et al., 2012).

It seems clear that the better part of sea-level variability in the tropical Pacific is due to adiabatic processes and can be understood in terms of redistribution of heat driven by wind-stress changes (Timmermann et al., 2010; Piecuch and Ponte, 2011; Merrifield, 2011; Merrifield and Maltrud, 2011; McGregor et al., 2012b; Merrifield et al., 2012; Moon and Song, 2013; Moon et al., 2013; Qiu and Chen, 2012). However, exchanges of heat and fresh water between the ocean and the atmosphere can also affect sea-level variability, as they change the density of the surface waters. They are commonly referred to as "buoyancy fluxes". Only a few studies have addressed the importance of such diabatic processes for sea level in the region. Piecuch and Ponte (2011) assessed the contribution of surface buoyancy fluxes to steric sea-level variability and identified a few regions where the contribution of local buoyancy fluxes is not negligible. One of them is the warm pool region in the western tropical Pacific. Other studies identified the central tropical Pacific as another region where local buoyancy fluxes contribute to interannual sea-level variability (Piecuch and Ponte, 2012; Forget and Ponte, 2015; Meyssignac et al., 2017). Piecuch et al. (2019) argue that local, latent heat fluxes in particular are relevant on decadal timescales and contributed to the recent reversal of sea-level trends in the tropical Pacific since 2012. All these studies used either local budget calculations or ocean model sensitivity simulations to estimate the contribution of buoyancy fluxes. Fukumori and Wang (2013) chose a different approach in a semi-Lagrangian model study and found buoyancy fluxes to be the dominant driver of sea-level trends between 1993 and 2004 in the western Pacific warm pool.

A detailed assessment of the relative contribution of buoyancy flux anomalies to sea-level variability in the region is important for projecting future sea-level trends in this region, since adiabatic and diabatic forcing mechanisms might evolve rather differently. However, in particular for the pre-altimetry era and on decadal timescales, we currently lack a detailed picture on how buoyancy fluxes affect sea level in the tropical Pacific and which mechanisms are involved. By means of eddy-permitting ocean model experiments that allow us to individually apply buoyancy and momentum flux forcing to the underlying ocean and by decomposing the steric sea-level component into thermosteric and halosteric contributions, we assess the importance of buoyancy fluxes on interannual to decadal timescales over the last 6 decades,

analyse their interplay with the wind-stress-driven variability and determine the importance of heat vs. freshwater fluxes.

4.3 Model experiments

We use a global ocean general circulation model (OGCM) configuration of the "Nucleus for European Modelling of the Ocean" (NEMO) code version 3.6 (Madec and NEMO-team, 2016). The model uses a global tri-polar ORCA grid at a $1/4^\circ$ horizontal resolution. The vertical grid consists of 46 z-levels with layer thickness varying from 6 m at the surface to 250 m at the deepest levels. Bottom topography is interpolated from 2-Minute Gridded Global Relief Data ETOPO2v2¹ and represented by partial steps (Barnier et al., 2006). The model is forced with the JRA55-do forcing (Tsujino et al., 2018) which builds on the JRA-55 reanalysis product but is adjusted relative to observational datasets.

Laplacian and bilaplacian operators are used to parameterize horizontal diffusion of tracers and momentum respectively. The ocean model is coupled to the Louvain-La-Neuve sea-ice Model version 2 (LIM2-VP; Fichefet and Maqueda 1997).

To avoid spurious drifts of global freshwater content, all models use a sea surface salinity restoring with piston velocities of 137 mm d^{-1} , which corresponds to a relaxation timescale of one year for the upper 50 m, and a freshwater budget correction that sets changes in the global budget to zero at each model time step.

In addition to a hindcast simulation (O025-HC) that uses realistic, interannual forcing and is integrated from 1958 to 2016, three sensitivity experiments were conducted to single out the effect of heat and freshwater fluxes (i.e. buoyancy fluxes) as well as intrinsic variability on sea-level variability on interannual to decadal timescales. In these experiments the interannual variability in the turbulent ocean-atmosphere fluxes is suppressed, either for all fluxes (O025-RYF90), for momentum fluxes (O025-B90), or for buoyancy fluxes (O025-W90).

This requires a method to eliminate interannual variability from the forcing, and we followed the approach of a "repeated-year forcing" (Stewart et al., 2020) to construct quasi-climatological atmospheric fields. Specifically, a 12-month period,

¹<http://www.ngdc.noaa.gov/mgg/global/relief/ETOPO2/ETOPO2v2-2006/ETOPO2v2g/>, last access: 12 June 2018

that is "neutral" with respect to a range of climate indices (hence the term quasi-climatological), is taken from the JRA55-do dataset and used repeatedly for the computation of turbulent fluxes. We followed the recommendation from Stewart et al. (2020) and used the period from May 1990 to April 1991 to force 59 cycles of each sensitivity experiment to match the length of the hindcast. The transition is moved from April to May, rather than December to January, to avoid periods of high variability at high latitudes, and therefore abrupt changes. The reader is referred to Stewart et al. (2020) for further information regarding the repeated-year approach. All model output is stored with monthly resolution and has been used previously for studies of Indian Ocean heat content (Ummenhofer et al., 2020) and marine heatwaves (Ryan et al., 2021).

Three caveats need to be considered when analysing the sensitivity experiments: firstly, the computation of turbulent fluxes depends not only on the atmospheric forcing but also the state of the underlying ocean. This introduces a source of interannual variability in buoyancy and momentum fluxes even where we aim to suppress it. Secondly, all experiments contain intrinsic variability, which is generated spontaneously by the ocean rather than by the atmospheric forcing. OGCMs with an eddy-permitting resolution, such as the ones used here, are able to capture this variability (Penduff et al., 2011). Consequently, variability in O025-W90 for example, can not exclusively be attributed to momentum flux but might also be generated by intrinsic variability. We will use the climatological experiment O025-RYF90, where this will be the dominant source of variability, to quantify this. Thirdly, the approach assumes a linear superposition of variability forced by momentum and buoyancy fluxes. However, the OGCM used here also includes non-linear responses of the ocean to atmospheric forcing, for example due to the non-linear nature of the equation of state, which may violate this assumption.

Interannual sea surface height² (SSH) variability from the model hindcast compares well with observations. Figure 4.1 shows interannual SSH variability as observed by satellite altimetry (gridded product is provided by the Copernicus Marine Service Center³ and simulated by the OGCM. Because the Boussinesq model used here does not capture the GMSL signal and the freshwater budget correction forces the GMSL anomaly to zero, the global mean signal has been removed from the altimetry data. The domain is characterized by the well-known zonal dipole with its

²We will refer to the sea-level estimate of the OGCMs, which gives height above the geoid, as SSH

³https://resources.marine.copernicus.eu/?option=com_csw&view=details&product_id=SEALEVEL_GLO_PHY_L4_REP_OBSERVATIONS_008_047, last access: 12 June 2018

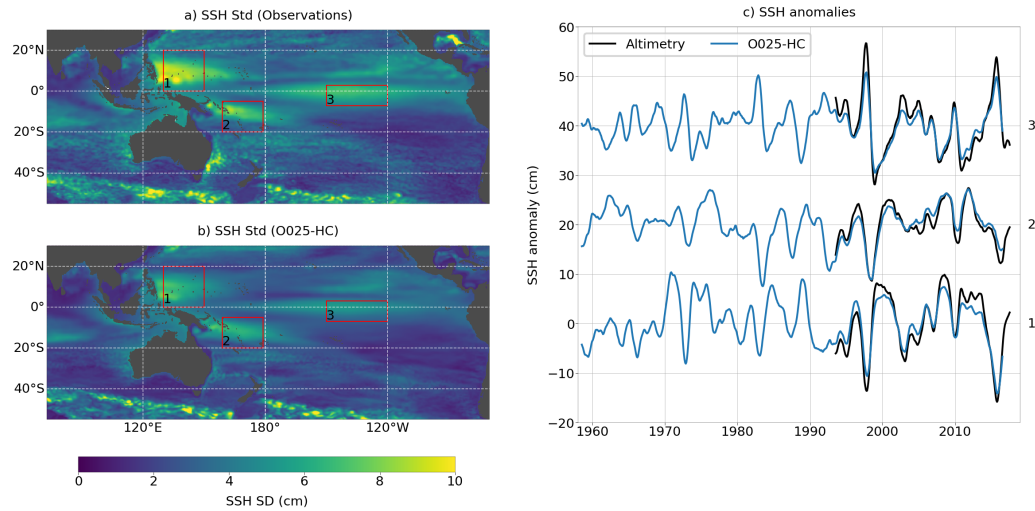


Fig. 4.1.: Standard deviation (SD) of SSH from (a) observations and (b) model simulation O025-HC. (c) SSH anomalies from observations and O025-HC averaged over three areas indicated by red boxes on the maps. Note that in panel c) a constant offset of 20 cm and 40 cm was added to anomalies from box 2 and 3 respectively. SD is based on the period from 1993 to 2016. The global mean trends have been subtracted, and all data were smoothed with a 12-month running-mean window prior to calculation.

eastern pole centred on the Equator in the central to eastern Pacific. The western pole shows two maxima located around 10° S and 10° N in the western part of the basin. Observations show amplitudes of up to 10 cm in the west and around 6 cm in the east (Fig. 4.1a). Overall, this structure is well captured by the model experiment, although the overall strength of the dipole is slightly underestimated with amplitudes of 8 cm and 5 cm in the western and eastern part respectively (Fig. 4.1b). SSH anomalies, averaged over three representative boxes in the northwestern (0° N– 20° N, 130° E– 150° E), southwestern (20° S– 5° S, 159° E– 179° E) and eastern (7° S– 3° N, 210° E– 240° E) tropical Pacific (shown as red boxes 1–3 on the maps in Fig. 4.1), from observations and model simulation confirm the reduced amplitude of interannual variability by about 20%. However, the phase of the interannual variability is reproduced well, with correlation coefficients above 0.93 for all three boxes. Within a latitudinal band of about 40° around the Equator, this result is not overly sensitive to the choice of the boxes (not shown). However, likely due to an insufficient spatial resolution, the model does not capture the mesoscale activity of the western boundary current regions properly and therefore underestimates SSH variability in this region even further, as can be seen by comparing Fig. 4.1 a) and b).

4.4 Results

Regional SSH variability is predominantly due to changes in the density of the water column (Fig. 4.2) with contributions from changes in the mass distribution negligible everywhere, except in shallow coastal regions (not shown). Fig. 4.2 shows the total SSH signal and its decomposition into steric, thermosteric and halosteric contributions for all three experiments. The steric signal in O025-HC is to a large extent due to changes in heat content (compare Fig. 4.2d and g). Compared to the total steric signal, the thermosteric variability shows slightly higher amplitudes in particular southwestern in the tropical Pacific. The same area is characterized by elevated values of halosteric variability (Fig. 4.2j), reflecting a compensating effect of thermosteric and halosteric changes in the region.

The momentum flux experiment yield a very similar result. Here, total SSH variability is mostly due to heat content changes with small contributions from halosteric changes that tend to dampen the thermosteric signal (compare Fig. 4.2b, e, h, k). Overall, these results concur with earlier accounts of the dominant role of thermosteric changes due to wind-stress variability for SSH variability in the tropical Pacific (e.g. Timmermann et al., 2010; Piecuch and Ponte, 2011; Merrifield et al., 2012; Moon and Song, 2013; Forget and Ponte, 2015).

However, although interannual SSH variability driven by surface buoyancy fluxes is small compared to the momentum-flux-driven variability, it is not negligible. Its spatial pattern differs from the wind-stress-driven component (Fig. 4.2c). The buoyancy flux contribution is most pronounced in the southern part of the study domain, with its maximum in the central Pacific around 10° S and is lowest on the Equator. The buoyancy-flux-driven signal is again steric in nature but in contrast to the wind-stress-driven signal the halosteric contribution is comparable in magnitude to the thermosteric part (compare Fig. 4.2 f, i and l). Note that O025-B90 also shows strong variability in the boundary current region of the Kuroshio, north of 20° N. This is a region of strong intrinsic variability (Fig. 4.3), most likely due to the strong mesoscale activity. We will therefore neglect this region in our analysis. It is also evident from Figure 4.3 that intrinsic variability is mostly negligible equatorward of approximately 20° latitude. Here, the ratio between SSH variance from O025-RYF90 and O025-HC does not exceed 5%.

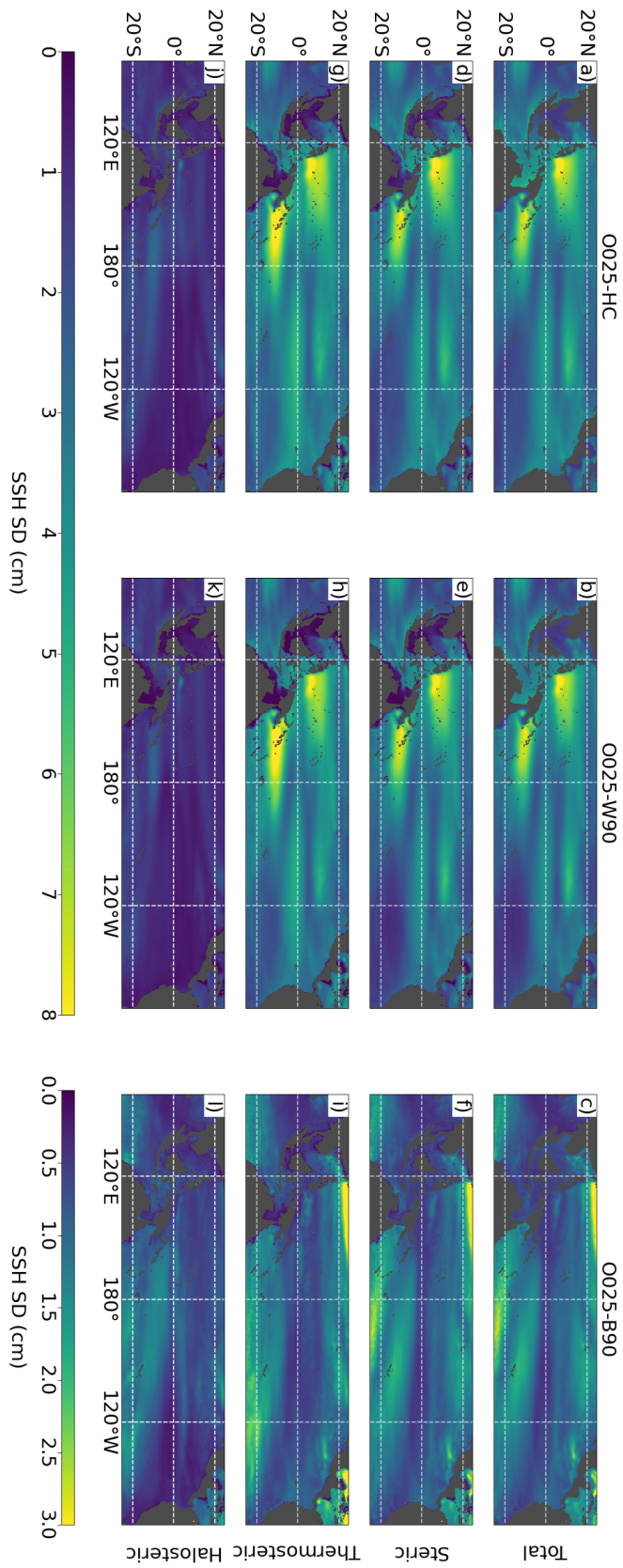


Fig. 4.2.: SD of total SSH (first row), steric SSH (second row), thermosteric SSH (third row) and halosteric SSH (fourth row) from O025-HC (left), O025-W90 (middle) and O025-B90 (right). SD is based on the period from 1958 to 2016. The global mean trends have been subtracted, and all data were smoothed with a 12-month running-mean window prior to calculation.

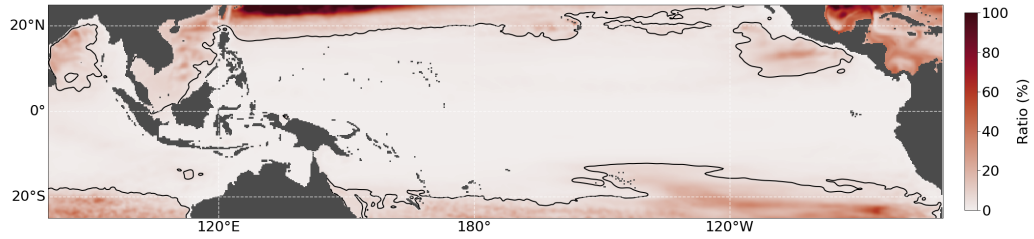


Fig. 4.3.: Ratio of SSH variance from O025-RYF90 and O025-HC. Black contour lines mark the 5% threshold. SDs are based on the period from 1958 to 2016. The global mean trends have been subtracted, and all data were smoothed with a 12-month running-mean window prior to calculation.

In order to assess the interplay between momentum and buoyancy fluxes, we analyse the change in variability between the hindcast experiment O025-HC and the momentum flux experiment O025-W90. This allows us to identify regions where momentum and buoyancy fluxes are correlated and to assess whether they tend to amplify or dampen one another. Figure 4.4 shows the change in interannual SSH variability in O025-W90 compared to O025-HC in terms of standard deviation (SD). Red/blue areas indicate regions where the variability increases/decreases when the interannual variability from the buoyancy flux forcing is removed, i.e. where buoyancy fluxes dampen/amplify wind-stress-driven SSH variability. The change in total SSH shows a pattern that is almost symmetrical about the Equator (Fig. 4.4a). Negative values prevail around the Equator and east of 225° E. A horseshoe-shaped minimum is located at the eastern boundary, where variability is reduced by up to 1 cm in the very east. Positive values are centred at 175° E on both sides of the Equator at 10° latitude with values of up to 0.4 cm in the north and 0.6 cm in the south. The same pattern can be seen for steric SSH (Fig. 4.4b) and, to a slightly lesser extent, for thermosteric SSH (Fig. 4.4c). The change in halosteric SSH is similar in magnitude but shows a different pattern. Changes are mainly limited to the western and southwestern tropical Pacific, where the halosteric SSH variability decreases in O025-W90 by up to 0.8 cm. Buoyancy fluxes seem to have a small effect on halosteric SSH in the eastern to northeastern tropical Pacific, where SD in O025-W90 changes by no more than 0.2 cm. Notably, regions where halosteric SSH variability is increased coincide with regions where total steric variability is damped. This indicates again the compensating effect of halosteric and thermosteric SSH changes. In short, buoyancy fluxes tend to dampen SSH variability in the eastern part of the domain and amplify it in the central and western part of the region.

We take a closer look at two regions where buoyancy fluxes have a strong, but opposite effect and analyse spatial averages over the two boxes marked in Fig.

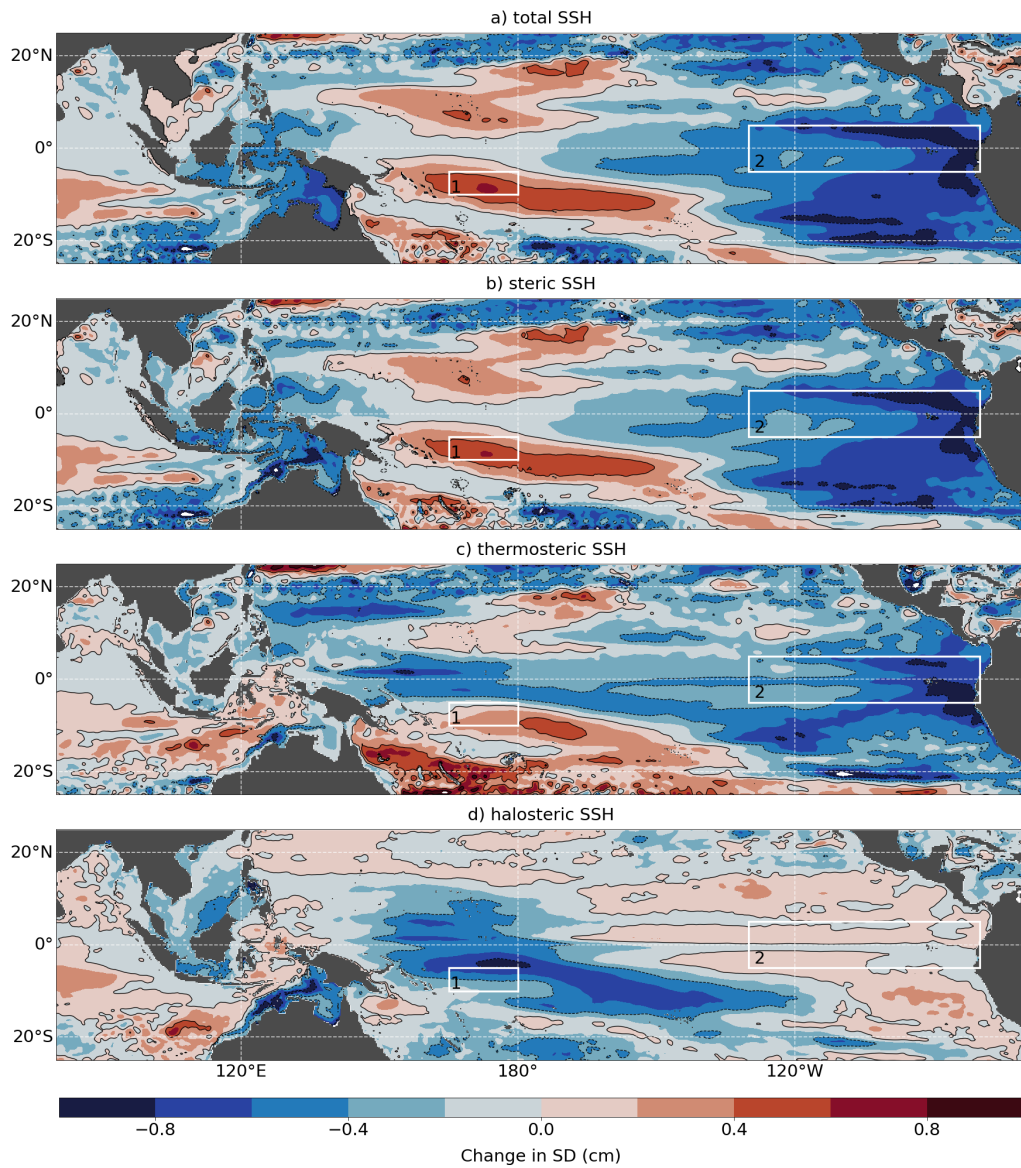


Fig. 4.4.: SD from O025-HC minus SD from O025-W90 for (a) total SSH, (b) steric SSH, (c) thermosteric SSH and (d) halosteric SSH. SD is based on the period from 1958 to 2016. The global mean trends have been subtracted and all data were smoothed with a 12-month running-mean window prior to calculation. Contour lines mark ± 4 cm, ± 8 cm and 0 cm.

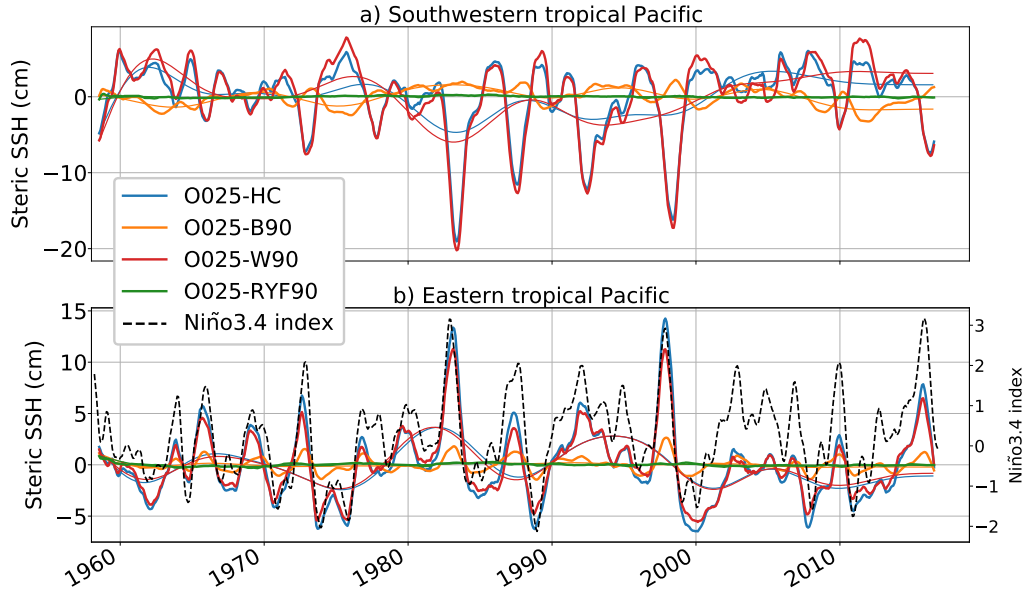


Fig. 4.5.: Time series of steric SSH anomalies from O025-HC, O025-W90 and O025-B90 averaged over boxes in the (a) southwestern and (b) eastern tropical Pacific. Exact regions are shown as white boxes (1,2) in Fig. 4.4. Thick lines are smoothed with a 12-month running-mean. Thin lines are low-pass filtered with an 8-year Butterworth filter. Dashed line in panel b) indicates Niño3.4 index.

4.4. In the southwestern tropical Pacific, SSH changes driven by momentum and buoyancy fluxes are clearly out of phase on interannual to decadal timescales. This negative correlation ($p=-0.6$) corresponds to the damping effect of buoyancy fluxes identified before. Measured by the change in SD between O025-HC and O025-W90, buoyancy fluxes dampen the variability by 11% on interannual and by 20% on decadal timescales. (Fig. 4.5a). The superposition of anomalies from O025-W90 and O025-B90 should reconstruct anomalies from O025-HC. We find a root-mean-square-error (RMSE) of 0.45 cm for this reconstruction. As discussed in section 4.3, possible causes are intrinsic variability (green lines in Fig. 4.5) and non-linear effects. Intrinsic variability is weak (SD of 0.11 cm), which suggests that non-linearities are the main cause.

Moving to the eastern box, we find steric SSH variability to show similar amplitudes of interannual and decadal variability with the corresponding signals being in phase ($p=0.7$). This is in line with the amplifying effect of buoyancy fluxes described above, and we find an increase in variability due to buoyancy fluxes by 16 %. In contrast to the western box, buoyancy fluxes have no effect on decadal SSH variability in the eastern part of the basin (Fig. 4.5b). Here, the superposition of O025-B90 and

O025-W90 to reconstruct O025-HC gives a much smaller RMSE of 0.2 cm. Unlike in the western box, intrinsic variability can account for a large fraction of this (SD of 0.14 cm).

Additionally, Fig. 4.5 b) visualizes the expected strong correlation between SSH anomalies and ENSO cycles.

Figure 4.2 suggests that both heat and freshwater fluxes drive SSH variability, in particular in the southwestern tropical Pacific. We investigate this further by decomposing SSH from O025-B90 into its thermosteric and halosteric part again. Figure 4.6 shows this decomposition for SSH anomalies in the southwestern and eastern tropical Pacific. In the southwestern domain (Fig. 4.6a) steric SSH is influenced in equal parts by halosteric and thermosteric contributions. Correlation coefficients are 0.62 and 0.48 (both significant on a 99% confidence interval) respectively, and from the beginning of the simulation until approximately 1990 the variability in both components has a similar amplitude. However, thermosteric SSH variability decreases after 1990 by more than 20% (SD drops from 0.75 cm to 0.59 cm and a moving-window calculation yields a linear decline of SD by 0.1 of cm per 10 years that starts around 1985; not shown) and steric SSH is subsequently primarily controlled by halosteric SSH (SD of 0.76 cm throughout the integration period). Steric SSH in the eastern equatorial Pacific is almost exclusively governed by thermosteric SSH with correlation coefficients of 0.89 (significant on a 99% confidence interval). While its variability is also smaller during the later part of the simulation, the decrease is not as drastic as in the western box (SD reduces from 71 cm to 63 cm). Halosteric SSH shows no significant correlations (on a 99% confidence interval) and only minor contributions, in particular during El Niño events (e.g. the 1997/98 El Niño; SD of halosteric SSH increases from 0.20 cm to 0.25 cm between the two periods, which is due to this strong El Niño event).

The effect of buoyancy fluxes on SSH variability is uniform across the zonal extent of the tropical Pacific. This is in particular true south of the Equator and explains the opposite effect of buoyancy fluxes (i.e. damping in the west and amplification in the east) on the wind-stress-driven zonal dipole structure. Figure 4.7 shows the temporal evolution of SSH along a zonal section at 10° S. The dipole structure in thermosteric SSH is clearly visible in O025-HC and O025-W90 (Fig. 4.7a, b, d, e) whereas the effect of halosteric SSH in the same experiments is limited to the central and western part of the region (Fig. 4.7c, f). Its compensating effect, related to the adiabatic advection of warm and saline surface waters, is clearly visible. Negative SSH anomalies dominate in the western part of the area during the negative PDO

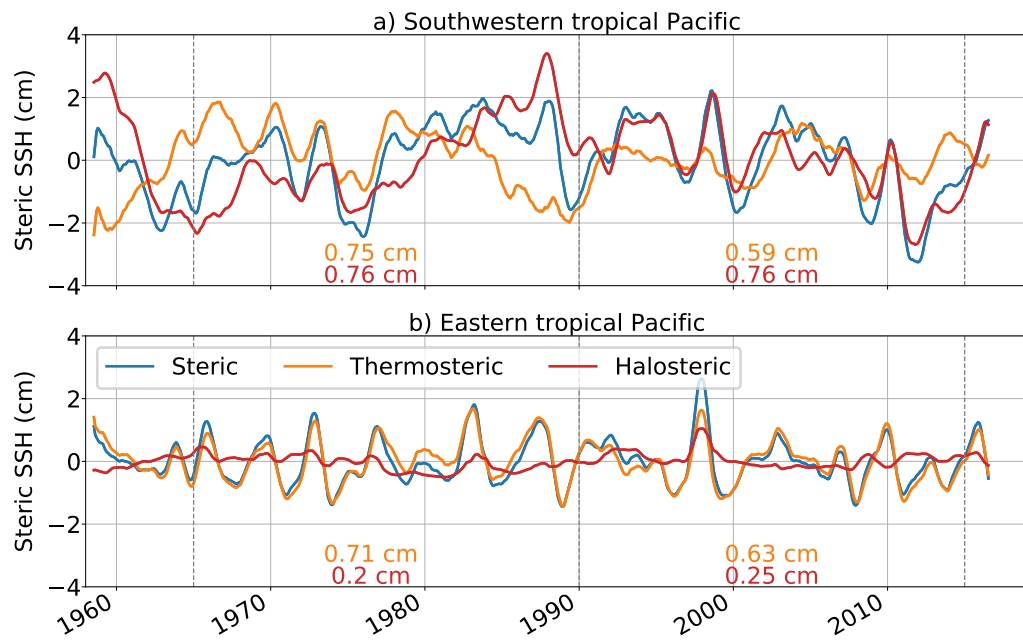


Fig. 4.6.: Time series of steric SSH anomalies from O025-B90 averaged over boxes in the (a) southwestern and (b) eastern tropical Pacific. Exact areas are shown as boxes 1 and 2 respectively in Fig. 4.4. Standard deviations for thermosteric and halosteric SSH anomalies are given for the periods from 1965–1990 and 1990–2015. All time series are smoothed with a 12-month running-mean.

phase in the 1980s and 90s and are caused by thermosteric anomalies. Positive halosteric anomalies act to increase SSH. SSH anomalies in O025-B90 show a zonally uniform structure across the basin (Fig. 4.7 g–j); i.e. their effect on the western and eastern poles of the wind-stress-driven, thermosteric dipole is exactly opposite. Maximum anomalies are located between 200° E and 220° E and are more pronounced in the western than in the eastern part of the area. The relative importance of buoyancy fluxes is highest for halosteric SSH, where amplitudes driven by momentum and buoyancy fluxes are comparable in magnitude (compare Fig 4.7f and i).

Our set of experiments specifically suggests that buoyancy-forced SSH variability in the tropical Pacific is relevant on interannual to decadal timescales (Fig. 4.2 and 4.5). Since the early 1990s, buoyancy-flux-driven SSH in the southwestern tropical Pacific is mostly controlled by halosteric effects, with the strongest signals emerging during El Niño or La Niña events (Fig. 4.6). In order to obtain insight into the mechanism by which halosteric SSH anomalies are triggered by buoyancy fluxes, how they spread zonally and how they interact with the wind driven SSH anomalies during ENSO events, we examine the particularly strong El Niño event in 1997/98.

4.5 Case study – 1997/98 El Niño

SSH anomalies (defined as the deviation from the seasonal climatology) from O025-HC during the El Niño event show the characteristic zonal dipole (Fig. 4.8a). In contrast to that, O025-B90 shows positive SSH anomalies centred in the central basin at the beginning of 1998 (Fig. 4.8b) which propagate westward with phase speeds of about 17 cm s^{-1} , which is in accordance with phase speeds of Rossby waves derived from linear theory (Killworth et al., 1997). Once they reach the western part of the basin by mid-1998, these positive anomalies tend to reduce the prevailing negative anomalies (compare fig. 4.8a and b). Anomalies in O025-B90 are mostly halosteric in nature (Fig. 4.8c). Areas of high precipitation start to propagate eastward at the beginning of 1997 and reach their easternmost position by the end of the same year where they trigger the SSH anomalies (Fig. 4.8d). There are only small precipitation anomalies east of 240° E, which explains the weak halosteric SSH anomalies in the eastern part of the basin described above. We note that the freshwater flux is controlled by precipitation at this latitude and evaporation is negligible (not shown). Thermosteric sea-level anomalies are smaller than their halosteric counterparts (Fig. 4.8e) and heat flux anomalies do not show a coherent

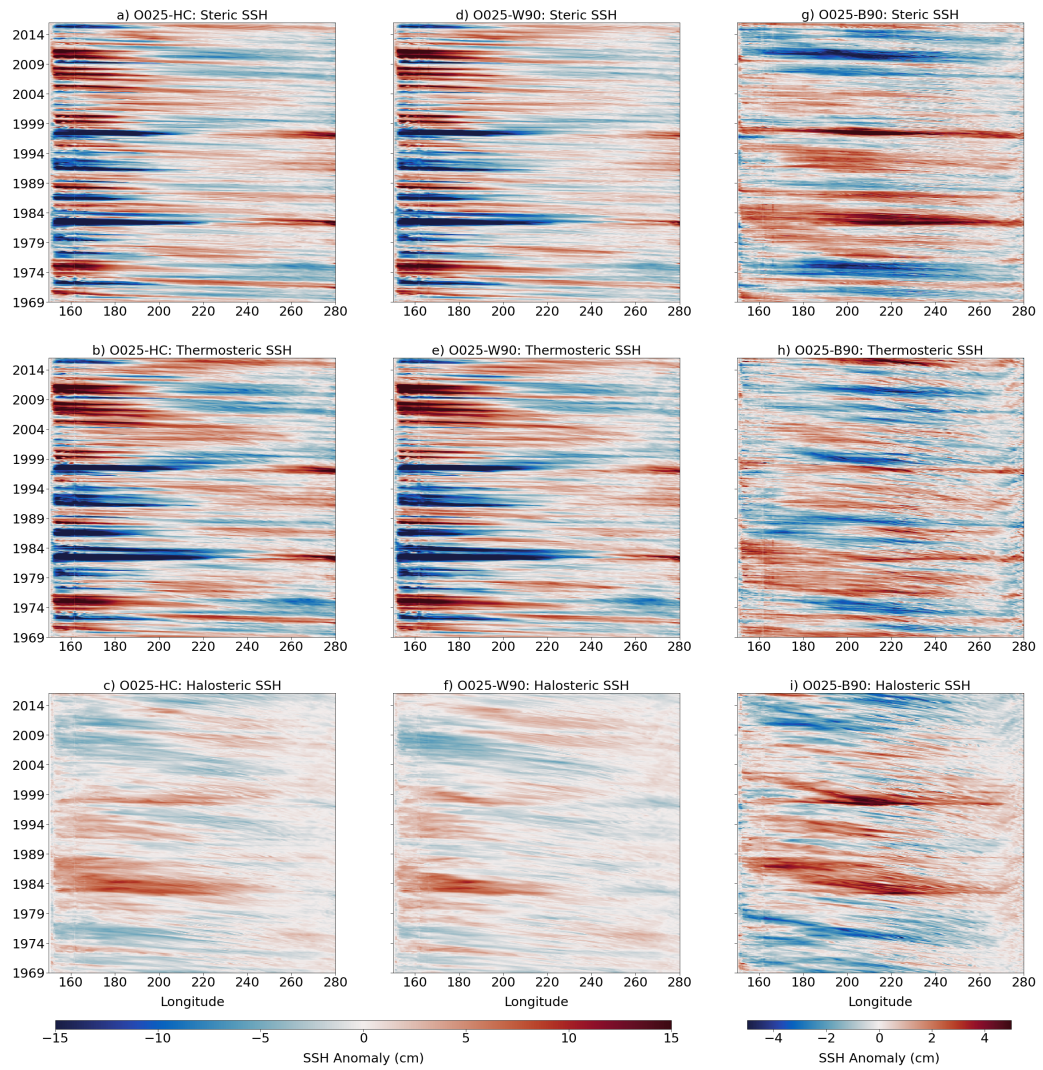


Fig. 4.7.: Hovmöller diagram of SSH anomalies at 10° S. Steric SSH (first row), thermosteric SSH (second row) and halosteric SSH (third row) from O025-HC (left), O025-W90 (middle) and O025-B90 (right). All data were smoothed with a 12-month running-mean.

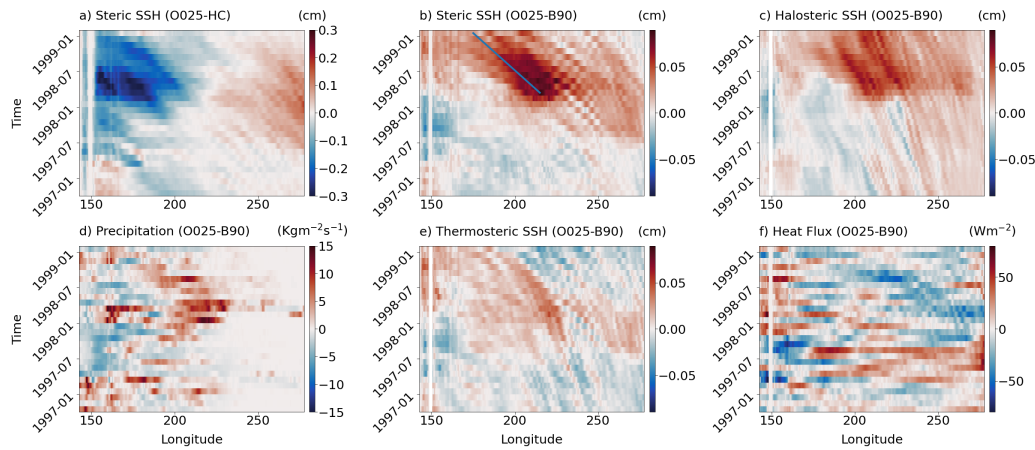


Fig. 4.8.: Hovmöller diagram at 10° S. (a) Anomalies of steric SSH from O025-HC and anomalies from O025-B90 of (b) steric SSH, (c) halosteric SSH, (d) precipitation, (e) thermosteric SSH and (f) net downward heat flux.

structure (Fig. 4.8f).

The co-occurrence in this example suggests that the halosteric SSH anomalies are at least partly driven by freshwater fluxes. However, buoyancy fluxes in general could also change the flow field and thereby cause adiabatic temperature and salinity anomalies, which would also result in corresponding SSH anomalies.

A different picture emerges along the equator. The zonal SSH dipole in O025-HC (Fig. 4.9a) is related to positive anomalies in the eastern basin, which are amplified by buoyancy fluxes (Fig. 4.9b). The steric anomalies are dominated by their thermosteric component (Fig. 4.9b,e), triggered by positive heat flux anomalies that evolve throughout the zonal extent of the basin between mid-1997 and early 1998 (Fig. 4.9f). Precipitation anomalies between mid-1997 and mid-1998 (Fig. 4.9d) are even stronger at the Equator than at 10° S but steric SSH anomalies in the central basin are weaker, and we do not find a pronounced zonal propagation of these anomalies. A possible reason for this is that sea level and thermocline depth expressions of Rossby waves are stronger off the equator, rendering signals of zonal propagation weaker on the equator. Another possible reason concerns the monthly resolution of the model output, which is insufficient to show the adjustment process associated with the eastward propagation of Kelvin waves. Given phase speeds of 2.8 m s^{-1} for the first baroclinic mode (Gill, 1982), Kelvin waves would take about 45 days to cross the distance between the International Date Line and the American west coast.

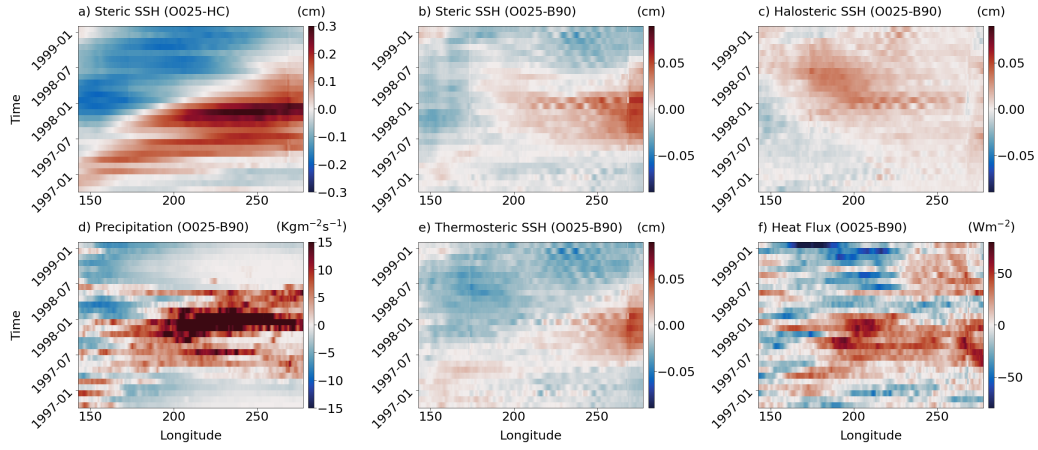


Fig. 4.9.: Hovmöller diagram at the equator. (a) Anomalies of steric SSH from O025-HC and anomalies from O025-B90 of (b) steric SSH, (c) halosteric SSH, (d) precipitation, (e) thermosteric SSH and (f) net downward heat flux.

In summary, positive SSH anomalies appear to be induced by buoyancy flux anomalies in the tropical Pacific during the peak of the El Niño event. Precipitation anomalies and collocated halosteric SSH anomalies suggest that freshwater fluxes play an important part in this mechanism. Off-equatorial SSH anomalies propagate westward as Rossby waves and counteract the negative SSH anomalies in the western tropical Pacific. Although, as pointed out with respect to Fig. 4.6, the relative contribution of halosteric and thermosteric anomalies varies over time, we find this mechanism to be relevant during most El Niño events and not only in the particular year shown here.

4.6 Summary and conclusion

We used a global ocean model to run a set of sensitivity experiments to determine the impact of ocean–atmosphere buoyancy fluxes on interannual to decadal SSH variability in the tropical Pacific. As expected, wind-stress variability, associated with the major basin-scale climate modes, is the most important driver of SSH variability in the region, causing the well known zonal dipole with opposing tendencies in the western and eastern parts of the tropical Pacific. We find that SSH variability due to buoyancy fluxes is generally small but not negligible, with the strongest contributions around 10° N and 10° S and a maximum in standard deviation of 2 cm in the central portion of the south Pacific.

Previous studies based on sensitivity experiments (Piecuch and Ponte, 2012; Forget and Ponte, 2015; Meyssignac et al., 2017) tend to agree with the results presented here in that they find a maximum of buoyancy flux forced interannual SSH variability on the order of 2–3 cm in the central tropical Pacific south of the equator. Studies using different methods, including budget analyses of ocean state estimates, have identified an impact of buoyancy flux forcing mostly in the western tropical Pacific (Piecuch and Ponte, 2011; Fukumori and Wang, 2013), with amplitudes of the related sea-level variability of up to 10 cm. However, all previous studies were limited to a period of 2–3 decades, i.e. the altimetric period since 1992.

By building on model simulations over the last six decades, the present study provides an extended perspective on the variability on interannual time scales and also allows a view of the decadal-scale changes. While previous studies mostly focus on heat fluxes, we also analysed the importance of freshwater fluxes for steric sea-level anomalies.

The results of the sensitivity experiments presented here suggest that, in contrast to the prevailing wind-stress-driven zonal dipole, buoyancy-flux-driven sea-level variability is zonally uniform across the extent of the basin but is correlated with the wind-stress-driven part. More specifically, buoyancy fluxes tend to dampen SSH variability in the western part of the basin but amplify it in the east. The eastern part of the domain is mostly dominated by interannual heat flux variability that increases during El Niño events, thereby increasing the thermosteric SSH and amplifying positive sea-level anomalies in the region. Here, buoyancy forcing has no impact on the variability on decadal timescales. Halosteric sea-level variability driven by buoyancy fluxes is negligible in this area, since its variability is largely confined to the central and western parts of the domain. In contrast, steric SSH variability due to surface buoyancy fluxes in the central and western Pacific is equally affected by thermosteric and halosteric contributions, with an increasing, relative importance of halosteric SSH in the last 3 decades due to a reduction in thermosteric SSH variability by more than 20%. Overall, buoyancy fluxes contribute to SSH variability on both interannual and decadal timescales, with a higher relative importance for the latter where they dampen the wind-stress-driven signal by 20%.

A source of uncertainty for the analysis presented here is intrinsic variability. We found it to be negligible in the tropical Pacific where it accounts for less than 5% of the interannual variability. This is in line with previous studies that showed that

intrinsic variability accounts for only a small fraction, mostly well below 10%, of the interannual (Penduff et al., 2011; Sérazin et al., 2015; Close et al., 2020; Carret et al., 2021) to decadal (Sérazin et al., 2016; Llovel et al., 2018) SSH variability in the tropical Pacific.

Yet another source of uncertainty is a possible non-linear response of the ocean to the atmospheric forcing. Indeed, based on a state-estimate analysis, Piecuch and Ponte (2012) showed that such effects might be relevant in the tropical Pacific, at least on a local scale. Although, with the methodology used here, it is difficult to quantify such effects, we found indications for non-linearities in particular in the western tropical Pacific.

The example of the 1997/98 El Niño event illustrates the oceanic response to buoyancy forcing. Halosteric SSH anomalies are induced in the central tropical Pacific by strong precipitation anomalies during El Niño events and propagate westward as off-equatorial Rossby waves where they act to dampen negative, thermosteric SSH anomalies. The oceanic response to buoyancy forcing can therefore be regarded as a dynamical signal that allows local buoyancy flux anomalies to remotely impact SSH. The mechanism appears to be similar to that described by Piecuch and Ponte (2012), suggesting a robust result of model sensitivity experiments to probe the relative importance of different forcing components. The contribution of both heat and freshwater fluxes identified here also emphasizes the need for an accurate representation of all components of the local air–sea buoyancy fluxes in model studies of regional sea-level projections in the tropical Pacific.

Decadal sea-level variability in the Australasian Mediterranean Sea

After analysing sea-level variability in the tropical Pacific and assessing the importance of buoyancy fluxes in this respect, the following chapter shifts the focus westward to the Australasian Mediterranean Sea (AMS). The chapter assesses the impact of Pacific climate modes on sea level in the AMS and also focuses on the role of buoyancy fluxes and intrinsic variability.

Because only a subset of the experiments introduced in chapter 2 is used here, the naming of the experiments is adapted:

HC-JRA: REF025

NUSA20: REF005

RYF90: CLIM

Markus Scheinert provided the model output of the experiment HC-JRA.

This chapter has been submitted for publication to the Journal "Ocean Science" and is currently under review. A previous version is published as a preprint:

Wagner, P. and Böning, C. W.: Decadal sea level variability in the Australasian Mediterranean Sea, Ocean Sci. Discuss. [preprint], <https://doi.org/10.5194/os-2021-63>, in review, 2021.

5.1 Abstract

Strong regional sea-level trends, mainly related to basin-wide wind-stress anomalies, have been observed in the western tropical Pacific over the last three decades. Analyses of regional sea level in the densely populated regions of the neighbouring Australasian Mediterranean Sea (AMS; also called tropical Asian Seas) are hindered by its complex topography and respective studies are sparse. We use a series of

global, eddy-permitting ocean models, including a high-resolution configuration that resolves the AMS with $\frac{1}{20}^\circ$ horizontal resolution, forced by a comprehensive atmospheric forcing product over 1958–2016, to characterize the patterns and magnitude of decadal sea-level variability in the AMS. The nature of this variability is elucidated further by sensitivity experiments with interannual variability restricted to either the momentum or buoyancy fluxes, building on an experiment employing a repeated year forcing without interannual variability in all forcing components. Our results suggest that decadal fluctuations of the El Niño-Southern Oscillation (ENSO) account for over 80 % of the variability in all deep basins of the region, except for the central South China Sea (SCS). Changes related to the Pacific Decadal Oscillation (PDO) are most pronounced in the shallow Arafura and Timor seas and in the central SCS. On average, buoyancy fluxes account for less than 10 % of decadal sea-level variability, but this ratio is highly variable over time and can reach values of up to 50 %. In particular, our results suggest that buoyancy flux forcing amplifies the dominant wind-stress-driven anomalies related to ENSO cycles. Intrinsic variability is mostly negligible except in the SCS, where it accounts for 25 % of the total decadal sea-level variability.

5.2 Introduction

Between the early 1990s and mid-2010s sea-level trends of up to 10 mm yr^{-1} , which exceeds 3 times the global mean rate, were observed in the western tropical Pacific and found to be related to an intensification of the Pacific trade wind regime (Timmermann et al., 2010; Merrifield, 2011; Merrifield and Maltrud, 2011; McGregor et al., 2012a; Merrifield et al., 2012; Moon and Song, 2013; Moon et al., 2013; Qiu and Chen, 2012). This strong sea-level rise had severe consequences for the population of the low-lying islands in the region (Becker et al., 2012), whose inhabitants are regularly referred to as the first climate refugees. Sea-level changes in the western tropical Pacific received a lot of scientific attention. Despite the exposed position of many densely populated, coastal communities, this is not true for the neighbouring areas of the Australasian Mediterranean Sea (AMS; see Fig. 5.1 for an overview map of the study domain). For the period 1993–2009 strong trends of up to 9 mm yr^{-1} were observed in the southwestern part of the region, but trends are not uniform across the many small seas of the region (Strassburg et al., 2015) and studies on regional sea-level variability in the region are sparse.

The best studied area in the region in terms of sea level is the South China Sea (SCS). It is the largest marginal sea of the region. The central and northeastern deep parts of the basin show the largest amplitudes of interannual and decadal variability (Cheng and Qi, 2007), with trends of up to 8 mm yr^{-1} for the period 1993–2012 (Cheng et al., 2016). There is a broad consensus that the El Niño–Southern Oscillation (ENSO) has a strong impact on interannual sea-level variability (Cheng and Qi, 2007; Cheng et al., 2016; Rong et al., 2007; Wu and Chang, 2005; Fang et al., 2006; Peng et al., 2013). Subsurface heat content anomalies are advected into the basin via the Luzon Strait (Cheng and Qi, 2007; Rong et al., 2007) and coastal Kelvin waves advect anomalies related to ENSO and possibly the Pacific Decadal Oscillation (PDO) from the tropical Pacific clockwise around the Philippines into the SCS (Liu et al., 2011; Zhuang et al., 2013; Cheng et al., 2016). Local wind-stress curl, also related to ENSO, might amplify these sea-level anomalies in the central SCS (Cheng et al., 2016). In contrast, Kleinherenbrink et al. (2017) did not find a strong impact of tropical wind-stress variability on sea-level changes in the SCS.

Sea-level variability in the southeastern part of the AMS, i.e. between Borneo and Australia, has received much less attention. However, the area has been of great interest since it represents the only low-latitude connection of ocean basins (Sprintall et al., 2014) and acts as an upper pathway of the global overturning circulation (Gordon, 1986). The main circulation feature is the Indonesian Throughflow (ITF) that transports heat and fresh water from the Pacific into the Indian Ocean (Gordon, 2005). The ITF variability on interannual timescales is mostly a response to variations of the Pacific trade winds and governed by large-scale climate modes. In particular, ENSO has a strong effect on ITF transport on interannual timescales (Meyers, 1996; Wijffels and Meyers, 2004; Liu et al., 2015). Decadal ITF variability is also linked to shifts of the Pacific trade wind regime (Wainwright et al., 2008; Liu et al., 2010; Zhuang et al., 2013; Feng et al., 2011, 2015), but other mechanisms, like deep Pacific upwelling (Feng et al., 2017), could also play a role. However, given the impact of Pacific easterlies on ITF variability, it is reasonable to assume that sea level along the ITF pathways is also remotely controlled by the Pacific trade wind regime. Indeed, sea-level variability along the Australian west coast is closely linked to variability in the western tropical Pacific (Feng et al., 2004; Lee and McPhaden, 2008; Merrifield et al., 2012). This requires a way for signals to cross the AMS. The theory of an equatorial waveguide that allows remote forcing of variability in the throughflow region was already proposed in 1994 (Clarke and Liu, 1994). Wijffels and Meyers (2004) show, based on XBT observations from 1984 to 2001, that sea-level anomalies propagate from the Pacific Ocean along the Papuan

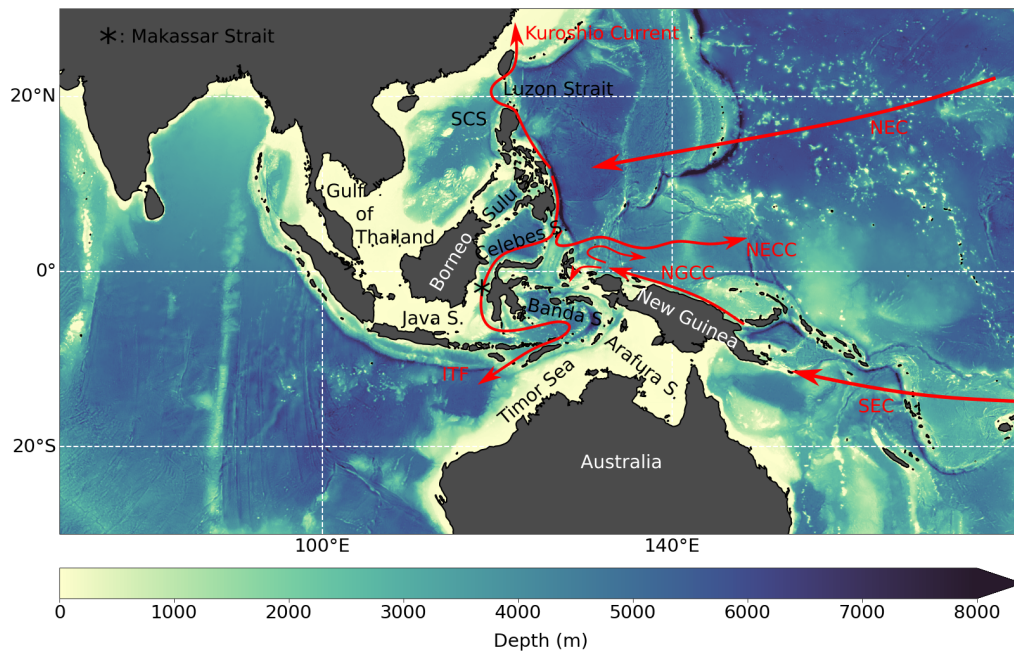


Fig. 5.1.: Overview map of study domain, depicting the marginal seas and schematic currents discussed in the text. Colour shading indicates depth. Marginal seas, islands, continents and schematic currents that are mentioned in the text are also marked. SCS: South China Sea, NEC: North Equatorial Current, SEC: South Equatorial Current, NECC: North Equatorial Countercurrent.

and Australian shelf break into the Indian Ocean and that interannual variability is driven by remote wind forcing from the Pacific.

In a more detailed analysis, Kleinherenbrink et al. (2017) separate observed sea-level changes between 2005 and 2012 into mass and steric components. They find mass changes to be relevant in the shelf regions, where a shallow water column is unable to expand due to density changes. Furthermore, they report that the deep basins of the Banda and Celebes Seas show large steric sea-level variability on interannual timescales which appear to be linked to wind stress anomalies over the tropical Pacific. Using the Dipole Mode Index (DMI; Saji et al. 1999) they also report an impact of the Indian Ocean that is however, limited to the Timor Sea. Strassburg et al. (2015) can also link observed and reconstructed decadal sea-level trends between 1950 and 2009 to PDO-related wind-stress changes over the tropical Pacific.

Comparatively little is known about the importance of local or remote buoyancy fluxes that have been proven to be relevant for sea level in other parts of the world's ocean, including the tropical Pacific (e.g. Piecuch and Ponte, 2011; Piecuch et al.,

2019; Wagner et al., 2021). Cheng and Qi (2007) suggest an influence of ocean–atmosphere freshwater fluxes on halosteric sea level in the SCS. In particular, the observed decrease between 2001 and 2005 is found to coincide with a salinification trend due to reduced freshwater fluxes. Rong et al. (2007) point out that local precipitation anomalies are the primary control of the SCS mass budget and thereby also influence sea level.

Using ocean and climate models to analyse sea level in this region is hindered by its complex topography that forms many small seas and narrow straits. For example, the Labani channel, the deep part of the Makassar Strait and the main pathway of the ITF, is only about 40 km wide, which is barely resolved in an $1/4^\circ$ ocean model, let alone in even coarser climate models. We therefore use a series of ocean model experiments that consists of two hindcast simulations that are subject to realistic atmospheric forcing covering the last 6 decades and providing horizontal resolution of $1/4^\circ$ and $1/20^\circ$, supplemented by a series of sensitivity experiments that allow an individual application of momentum and buoyancy flux forcing to the underlying ocean. The aim of this study is to examine the sea-level variability in the AMS in high-resolution ocean model simulations subject to atmospheric forcing over the last 6 decades. In particular, the objectives are the following:

- to elucidate the patterns and nature of the regional sea-level variability on decadal to multi-decadal timescales, including the impacts of the low-frequency ENSO and PDO changes which have been identified in previous studies as major drivers of sea-level variability on interannual to decadal timescales;
- to examine the possible contribution of intrinsic variability, internally generated by ocean dynamics, to the total sea-level variability in the region, and to determine the relative roles of momentum and buoyancy fluxes to the forced variability; and
- to analyse the individual contributions of temperature and salinity changes to steric sea-level variability.

Concerning the notation of the marginal seas between Australia and Asia, some deviating conventions have been used in the natural science community since international standards have not been officially updated since 1953 (International Hydrographic Organisation, 1953). Examples are "Tropical Asian Seas" (Kleinenbrink et al., 2017), "Southeastern Asian Seas" (Strassburg et al., 2015) and "Australasian Mediterranean Sea" (Tomczak and Godfrey, 2003). We adapted the latter for the purpose of this study and refer to all marginal seas in the region,

including the Timor and Arafura seas and also the SCS, as AMS. It will be useful to point to the SCS and the remaining part of the region individually. We use the term "Eastern Archipelagic Seas" (EAS) for this purpose.

5.3 Methods

5.3.1 Ocean general circulation model experiments

We use a global ocean model configuration of the "Nucleus for European Modelling of the Ocean" (NEMO) code version 3.6 (Madec and NEMO-team, 2016). The model employs a global tripolar ORCA grid and uses 46 vertical z-levels with varying layer thickness from 6 m at the surface to 250 m in the deepest levels. Bottom topography is represented by partial steps (Barnier et al., 2006) and is interpolated from 2-Minute and 1-Minute Gridded Global Relief Data ETOPO2v2¹ and ETOPO1² (Amante and Eakins, 2009) for the coarse- and high-resolution experiments, respectively. The atmospheric forcing for all experiments is JRA55-do v1.3 (Tsujino et al., 2018) which builds on the JRA-55 reanalysis product but is specifically designed to be used as a forcing dataset for OGCMs. Most importantly, surface fields are corrected towards observations and heat and freshwater fluxes are balanced with respect to a defined set of bulk formulae. Laplacian and bi-Laplacian operators are used to parameterize horizontal diffusion of tracers and momentum, respectively. The ocean model is coupled to the Louvain-La-Neuve sea-ice model version 2 (LIM2-VP; Fichefet and Maqueda 1997). To avoid spurious drifts of the global freshwater content, all models use a sea surface salinity restoring with piston velocities between 137 mm per day and 40 mm per day. The coarse-resolution experiments additionally use a freshwater budget correction that sets changes in the global budget to zero at each model time step.

In order to increase the horizontal resolution in the area of interest, a high-resolution "nest" is incorporated into the global base model. This approach allows a regional refinement of the horizontal resolution to $\frac{1}{20}^\circ$ in the area from 50°S to 25°N and 75°E to 180°E. The nesting technique is based on the "adaptive grid refinement

¹<http://www.ngdc.noaa.gov/mgg/global/relief/ETOP02/ETOP02v2-2006/ETOP02v2g/>, last access: 12 June 2018

²<https://www.ncei.noaa.gov/access/metadata/landing-page/bin/iso?id=gov.noaa.ngdc.mgg.dem:316>, last access: 11 October 2019

in fortran” (AGRIF; Debreu et al. 2008). A two-way communication is established between the high-resolution nest and the global ”coarse”-resolution model. The base model provides boundary conditions for the nest at every time step of the nest (the base model and the nest were integrated with a time step of 5 and 15 minutes, respectively). Due to the higher resolution of the nest in time and space, the boundary conditions are interpolated. The prognostic variables along the boundary of the nest are in turn updated after every time step of the base model by the calculations provided by the nest. Every three time steps, the full baroclinic state vector of the nest is averaged onto the base grid and fed back to the base model. This approach is well established, and the reader is referred, for example, to Schwarzkopf et al. (2019) for a detailed description of the procedure.

We integrate two reference configurations with interannually varying atmospheric forcing from 1958 to 2016:

- **REF005:** Reference run with $\frac{1}{4}^\circ$ horizontal resolution globally and $\frac{1}{20}^\circ$ in the nest area.
- **REF025:** Reference run with $\frac{1}{4}^\circ$ horizontal resolution globally.

In addition, we follow the approach of Stewart et al. (2020) to construct a repeated year forcing. More specifically, we extract the recommended 12-month subset from May 1990 to April 1991 from the full forcing dataset and apply its individual fields repeatedly to suppress the interannual variability entirely or only for the computation of momentum or buoyancy fluxes, respectively. This way, we obtain three additional sensitivity experiments with $\frac{1}{4}^\circ$ horizontal resolution globally, which were all integrated for 59 years to match the length of the reference configurations:

- **CLIM:** full repeated year forcing.
- **WIND:** repeated year forcing for buoyancy fluxes.
- **BUOY:** repeated year forcing for momentum fluxes.

The experiments WIND and BUOY are meant to isolate the momentum-flux-forced and buoyancy-flux-forced variability. The approach builds on the assumption that the total atmospherically forced variability can approximately be understood by a linear combination of these two contributions. Because we only suppress variability on interannual and longer timescales, this assumption is not valid for variability on shorter timescales. A possible deviation could also arise from non-linearities and intrinsic, i.e. unforced, variability: an estimate of the magnitude of the latter is

provided by the experiment CLIM. We note that the set of $\frac{1}{4}^\circ$ experiments (REF025, WIND, BUOY and CLIM) has been used previously for studies of the Indian Ocean heat content (Ummenhofer et al., 2020), marine heatwaves (Ryan et al., 2021) and tropical Pacific sea-level variability (Wagner et al., 2021).

5.3.2 Observational datasets

Two observational datasets are used to validate our model results. Satellite altimetry data are provided as a gridded product by the Copernicus Marine Environment Monitoring Service³ (CMEMS) with a resolution of $\frac{1}{4}^\circ$ that is available starting in 1993 (in contrast to the model simulations that start in 1958). Observations of temperature and salinity are taken from the World Ocean Atlas 18⁴ (WOA18; Locarnini et al. 2019; Zweng et al. 2019) that is also available with $\frac{1}{4}^\circ$ horizontal resolution and covers the period from 1958 to 2017.

5.3.3 Steric sea level

Sea-level changes are either due to changes in the total mass of the water column or due to density changes in seawater. The latter is referred to as steric sea level. Because seawater density is affected by temperature and salinity, steric sea level can be separated into thermosteric and halosteric components, respectively. We diagnosed steric sea-level changes from the stored model output:

$$\frac{\partial \eta^{steric}}{\partial t} = - \int_{-H}^{\eta} \frac{1}{\rho} \frac{\partial \rho}{\partial t} dz, \quad (5.1)$$

where (η) denotes sea level, ρ is seawater density and H is ocean depth. Thermosteric sea-level changes are given by:

$$\frac{\partial \eta^{thermosteric}}{\partial t} = \int_{-H}^{\eta} \left(\alpha \frac{\partial \Theta}{\partial t} \right) dz, \quad (5.2)$$

where α is the thermal expansion coefficient and Θ is potential temperature. In the same way, halosteric sea-level variations can be expressed as

$$\frac{\partial \eta^{halosteric}}{\partial t} = \int_{-H}^{\eta} \left(\beta \frac{\partial S}{\partial t} \right) dz, \quad (5.3)$$

³https://resources.marine.copernicus.eu/?option=com_csw&view=details&product_id=SEALEVEL_GLO_PHY_L4_REP_OBSERVATIONS_008_047, last access: 12 June 2018

⁴<https://www.ncei.noaa.gov/archive/accession/NCEI-WOA18>, last access: 16 February 2021

where β is the haline contraction coefficient and S is salinity.

5.4 Results

First, we compare our model results to observational products for validation and to point out some resolution-dependent biases. Sea-level observations from satellite altimetry show strong interannual sea surface height⁵ (SSH) variability in the western tropical Pacific, off the east coast of the Philippines islands. Within the AMS, variability is most pronounced in the deep basins of the SCS and the adjacent Sulu, Celebes and Banda seas as well as in the coastal regions of the Arafura and Timor seas (Fig. 5.1). Both hindcast simulations slightly underestimate the amplitude of standard deviation (SD), in particular in the western tropical Pacific by 1 to 2 cm (REF025 and REF005, respectively) but reproduce the spatial pattern well (Fig. 5.2 b, c). The spatial average of SSH over the AMS (see black contour in Fig. 5.2 c) reveals interannual to decadal variability. The latter is more pronounced in the high-resolution configuration (REF005) and agrees well with the observed positive trends since the early 90s (Fig. 5.2 d).

Figure 5.3 shows subsurface maps of mean fields and model biases of temperature and salinity with respect to observations from WOA18, averaged over the upper 400 m, from both hindcast simulations. Both hindcasts exhibit some temperature biases, in particular in the tropical Pacific, where opposite signs right on the Equator and at about 8°N (Fig. 5.3 a–c) indicate a large-scale southward displacement of the Intertropical Convergence Zone (ITCZ) in the Pacific that causes a southward shift of the equatorial upwelling regime. The coarse-resolution hindcast REF025 also shows positive temperature and salinity biases in the AMS, in particular in the northern part of the SCS, where values exceed 3° and 0.3 psu (Fig. 5.3 b, e). These biases are greatly reduced in the high-resolution setup to temperature biases well below 0.5°C and salinity biases below 0.1 psu.

5.4.1 Impact of buoyancy fluxes on SSH

We now turn to the forcing mechanism of decadal SSH variability and inspect the low-pass-filtered (cutoff period of 8 years) SSH time series. Figure 5.4 presents

⁵We will refer to the sea-level estimate of the OGCMs, which gives height above the geoid, as SSH.

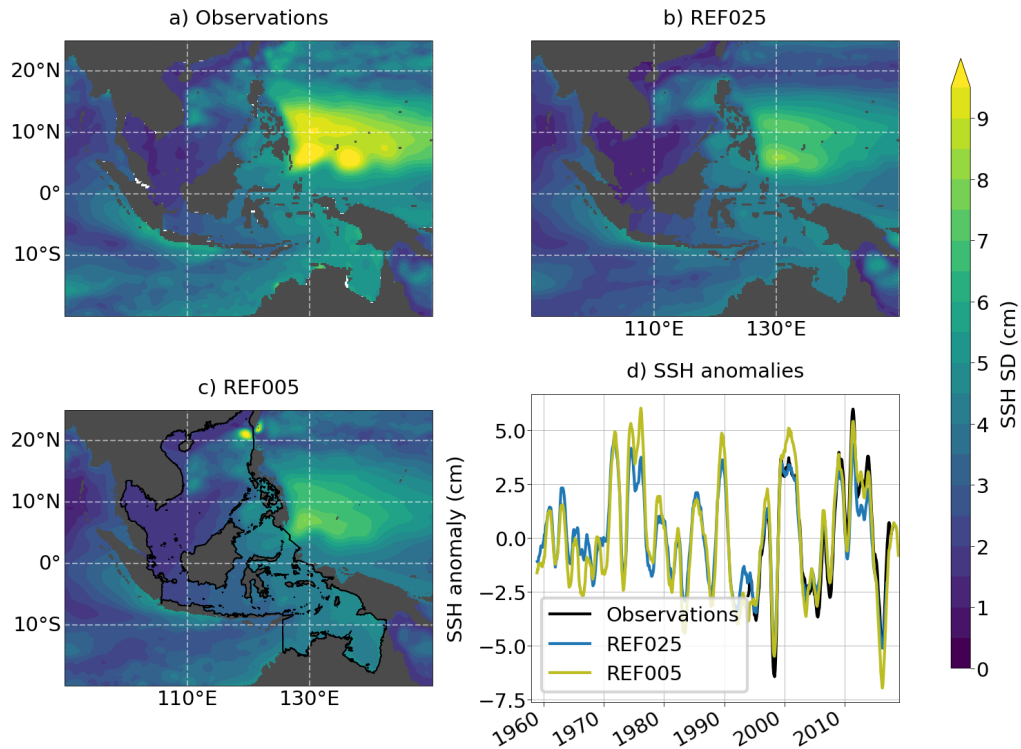


Fig. 5.2.: Standard deviation (SD) of sea surface height (SSH) from (a) observations and two hindcast experiments (b) REF025 and (c) REF005 over the period 1993 to 2016. d) SSH anomalies averaged over the region marked by black contours in panel c). The global mean trends over the integration period have been subtracted, and all data were smoothed with a 12-month running mean window.

maps of SDs for all five experiments, as well as SSH anomalies averaged over the AMS. The two hindcast simulations show a close resemblance in terms of amplitude and pattern, suggesting only a minor influence of the model resolution (Fig. 5.4 a, b). The pattern and amplitude of the WIND experiment (Fig. 5.4 c) closely match the signal in REF025, indicating that wind-stress variability is the most important driver of the variability. The SSH signal driven by the interannual variability of buoyancy fluxes shows much lower amplitudes and a different spatial pattern (Fig. 5.4 d; note the different colour bars): it is most pronounced outside the AMS in the Kuroshio region and the southeastern, tropical Indian Ocean and within the AMS in the SCS, whereas values in the EAS are relatively low (about 0.3–0.4 cm).

While in most areas the total variability in REF025 can be understood as a linear superposition of variability due to momentum and buoyancy fluxes, this is not the case in the Kuroshio region or the Gulf of Thailand. Possible reasons are cancelling effects of out-of-phase variations of momentum and buoyancy fluxes or, as pointed

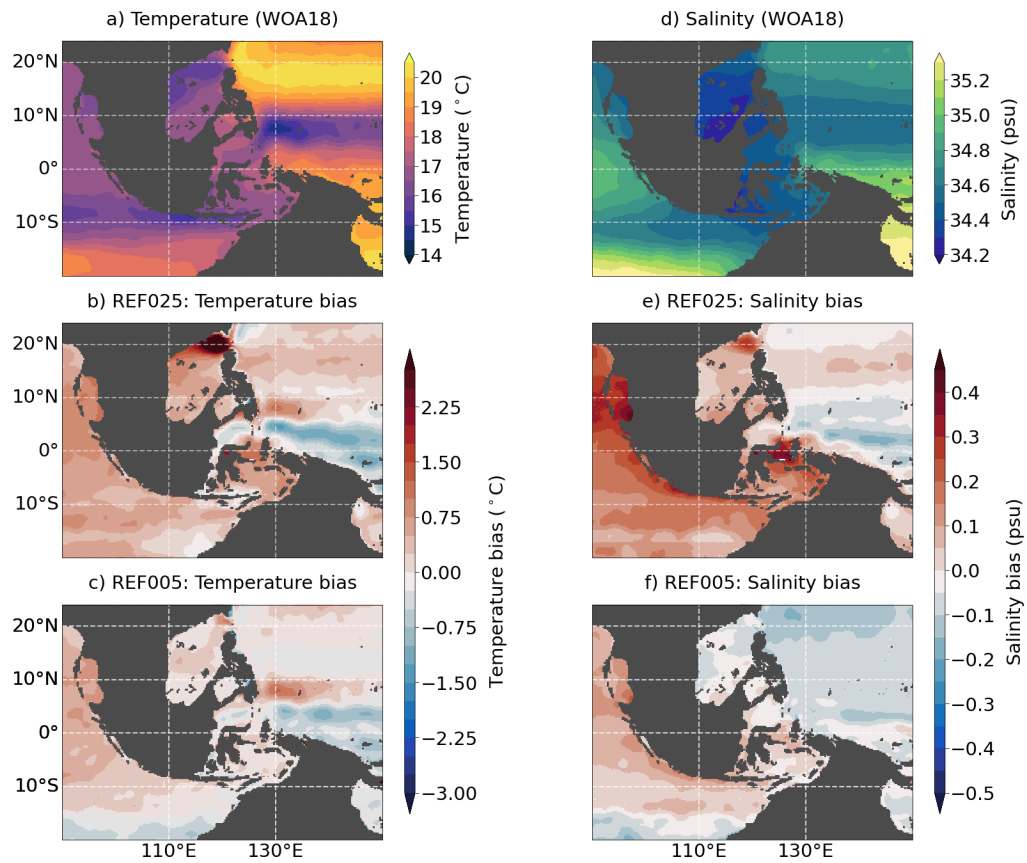


Fig. 5.3.: Mean fields (1955–2017; upper row) and model biases (1958–2016; middle and bottom row) averaged over the upper 400 m for (a-c) temperature and (d-f) salinity. Note that data are only shown where the water depth exceeds 400 m.

out above, intrinsic ocean variability and non-linear effects. As evident from Fig. 5.4 e), intrinsic variability in the AMS is below 0.2 cm everywhere except in the SCS. Amplitudes in the northern SCS reach values of up to 1 cm and are thereby comparable to the values of the buoyancy forcing experiment and account for about 25 % of the total variability in REF025.

Averaged over the AMS, buoyancy fluxes amplify the wind-stress-driven variability (Fig. 5.4 f). If we consider the change in variability between REF025 and WIND, rather than the variability in BUOY itself, to be the effect of buoyancy fluxes, we find a contribution of 9 % (SD of 1.54 cm in REF025 and 1.4 cm in WIND) by which buoyancy fluxes amplify the wind-stress-driven variability. This fraction is, however, variable over time and reaches values of up to 50 %, for example during the late 1990s. When estimating the effect of buoyancy fluxes from BUOY directly, we obtain a much larger contribution of 24 %. The reason for this is intrinsic variability that is included in all experiments and adds to the variability in BUOY. We find no indication that buoyancy fluxes contribute to the increase in sea level between roughly 1990 and 2010 that is visible in both hindcast simulation and WIND.

5.4.2 Linear regression of SSH on ENSO and PDO indices

A linear regression model is used to quantify the impact of low-frequency ENSO changes and PDO cycles on sea-level variability. We use a bandpass-filtered Niño3.4 index⁶ (8–13 years) and a low-pass-filtered PDO⁷ index (13 years) as predictors. Both indices are derived from REF025 and compare well with observational estimates^{8,9} (Fig. B.1). Both indices are not significantly correlated (at a confidence interval of 5 %) by construction because their variability is limited to timescales longer or shorter than 13 years. This allows a linear superposition of the responses and their respective coefficients of determination (R^2 gives the fraction of variance explained by a linear model; e.g. Thomson and Emery 2014). As before, SSH data has been low-pass filtered (8 years) prior to the regression. Note that the PDO can

⁶The Niño3.4 index is defined as the area-averaged sea surface temperature (SST) anomaly in the Niño3.4 region (5° N–5° S, 170° W–120° W) with respect to the monthly climatology and normalized by its SD.

⁷The PDO index is obtained via an empirical orthogonal function of monthly SST anomalies in the Pacific north of 20° N and defined as the leading mode of variability. The climatological annual cycle is subtracted to remove long-term trends.

⁸<http://research.jisao.washington.edu/pdo/PDO.latest>, last access: 08 Jun 2017

⁹https://psl.noaa.gov/gcos_wgsp/Timeseries/Data/nino34.long.data, last access: 07 June 2017

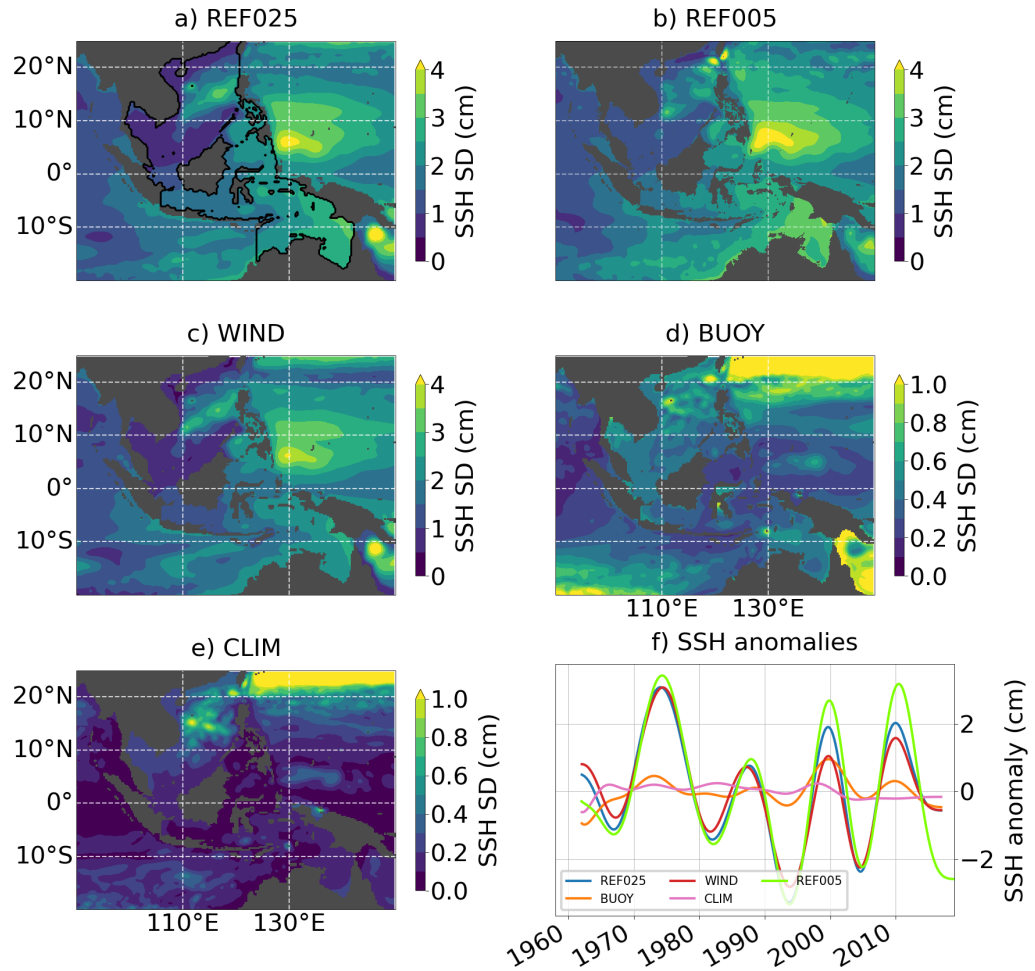


Fig. 5.4.: *SD of low-pass-filtered SSH time series (8 years) from (a) REF025, (b) REF005, (c) WIND, (d) BUOY, (e) CLIM as well as (f) lowpass-filtered SSH anomalies averaged over black contour lines shown in panel a). Note the different colour bars.*

be considered the low-frequency component of ENSO in this context to the extent that an alternative, and largely equivalent separation could be build on the low-pass filtered Niño3.4 index instead of the PDO index. We will get back to this point in section 5.5. The Indian Ocean Dipole Index (IOD; Saji et al. 1999) could account for possible impacts of the Indian Ocean. We do not include the IOD in our analysis because the index shows only very weak variability on the timescales considered here (not shown).

Figure 5.5 depicts the linear responses of SSH from three experiments to the Niño3.4 and PDO indices. Since its results are very similar to REF025, we omit the WIND case here but refer to it in the Appendix (Fig. B.2). REF025 and REF005 show a similar response to positive ENSO cycles (Fig. 5.5 a, b). Strong negative anomalies in the western tropical Pacific with amplitudes of 4 cm off the east coast of the Philippines islands leak into the northeastern part of the SCS and also follow the equatorial waveguide across the Celebes and Banda Seas as well as along the Australian shelf break into the Indian Ocean. Here, both hindcasts find amplitudes between 1 and 2 cm (Fig. 5.5 a, b). This pattern is mostly determined by wind-stress variability, as the wind-stress experiment shows similar results (Fig. B.2) and the pattern in BUOY differs strongly (Fig. 5.5 c). Here, SSH shows a weak but non-negligible, negative response to ENSO cycles which is uniform across the domain and thereby amplifies the wind-stress-driven response by about 0.2–0.3 cm in most parts of the region. Buoyancy fluxes counteract the wind-stress-driven variability off the northeastern coast of Australia, to the south of Papua New Guinea, such that the effective ENSO-related SSH variability is almost zero.

The linear response to the PDO index shows strong amplitudes of 3 and 4 cm (in REF005 and REF025 respectively; Fig. 5.5 d, e) to the east of Papua New Guinea in the region of the South Pacific Convergence Zone (SPCZ). Anomalies stretch northwestward along the shelf and into the EAS, in particular into the Arafura Sea, with values between 1 and 2 cm. Both hindcast experiments also suggest a PDO imprint in the Java Sea and the central SCS. Again, the variability is mostly driven by momentum fluxes (Fig. B.2). Buoyancy fluxes can not explain the dominant pattern and tend to dampen the variability regionally, in particular in the SPCZ, but also in the western tropical Pacific north of 10°N, in the northern part of the SCS and in the Sulu Sea. The response in the remaining regions is mostly below 0.1 cm.

In order to determine what fraction of the total variability can be explained by these two climate indices, Fig. 5.6 displays R^2 . Both hindcasts (and also the WIND experiment; Fig. B.2 a) agree that ENSO determines a large fraction of the low-frequency variability in the western tropical Pacific at around 5°N and in all deep basins of the AMS with values of over 80 % and, to a slightly lesser extent, also in the Timor Sea and along the Australian shelf break. This fraction is reduced to less than 50 % for the buoyancy-flux-related variability (Fig. 5.6 c).

Both hindcast simulations find that over 50 % of the total decadal SSH variability in the SPCZ and the Java Sea and over 30 % in the central SCS can be explained by PDO cycles. Both differ in their estimate of the quantitative importance of the PDO for the remaining region of the EAS, but still find 10–20 % of explained variance in the case of REF005 and even more in REF025. Note, however, that REF025 showed temperature and salinity biases in this region that might be the reasons for these discrepancies. The PDO does not drive any buoyancy-flux-driven SSH variability in the AMS (Fig. 5.6 f). The linear combination of the two indices (not shown) gives high scores of over 80 % throughout the domain except in the central and southern part of the SCS where intrinsic variability is relevant.

5.4.3 Decomposition of SSH variability into thermosteric and halosteric contributions

To further elucidate the mechanisms shaping the sea-level signal, it is useful to analyse the dynamical response and also decompose the sea-level signal into its steric components. We neglect sea-level anomalies due to mass fluctuations because their relative contributions are small everywhere except in shelf regions (not shown; e.g. Forget and Ponte, 2015) where the total variability is weakest.

As expected, the dynamical response to the ENSO cycles (Fig. 5.7 a-c) is governed by anomalies of the North Equatorial Countercurrent at 4°N and by thermosteric SSH anomalies of over 4 cm in the western tropical Pacific. The latter change the inter-basin pressure gradient between the Pacific and the Indian Ocean. Specifically, a positive ENSO cycle leads to a reduction in SSH, which causes a decreased pressure gradient across the AMS. Consequently, northward velocity anomalies in the Makassar Strait and Banda Sea indicate a reduction of ITF transport. Steric changes are consistent with this dynamical response of the upper ocean. The reduction

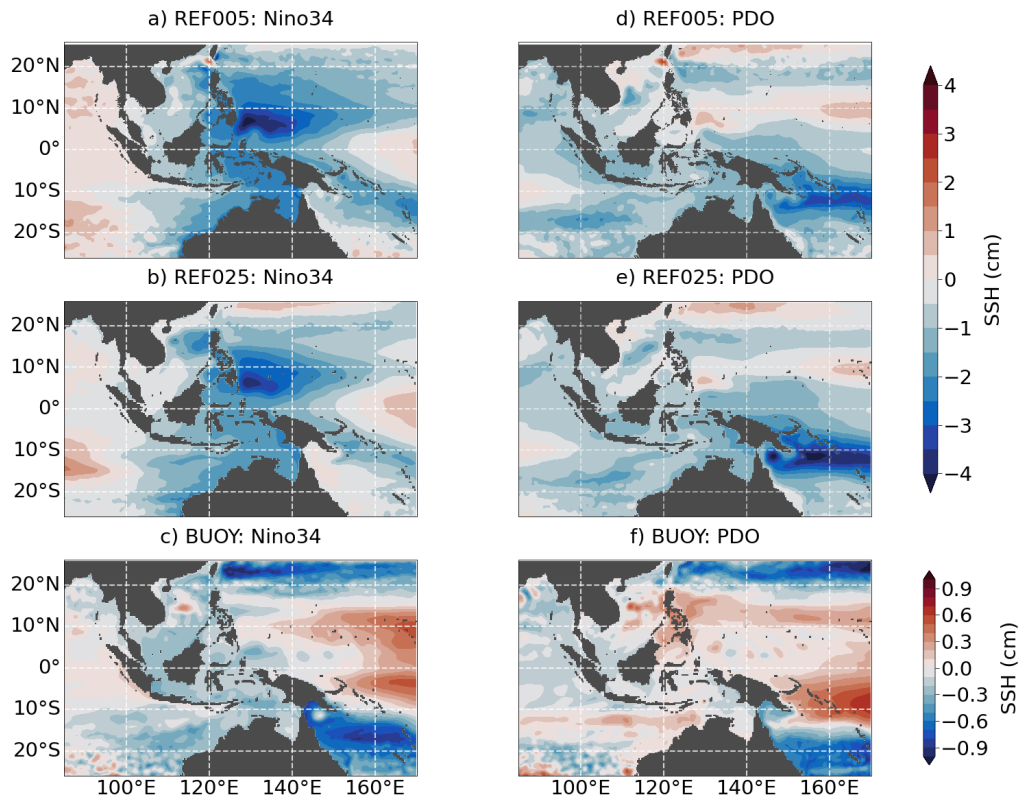


Fig. 5.5.: Linear regression of SSH with the (a-c) Niño3.4 index and (d-f) PDO index for two hindcast (REF025, REF005) and buoyancy forcing experiments (BUOY). Climate indices are derived from the base model in the case of REF005 and from REF025 for the other two experiments. All data have been filtered with an 8-year low-pass filter. Note the different colour bars.

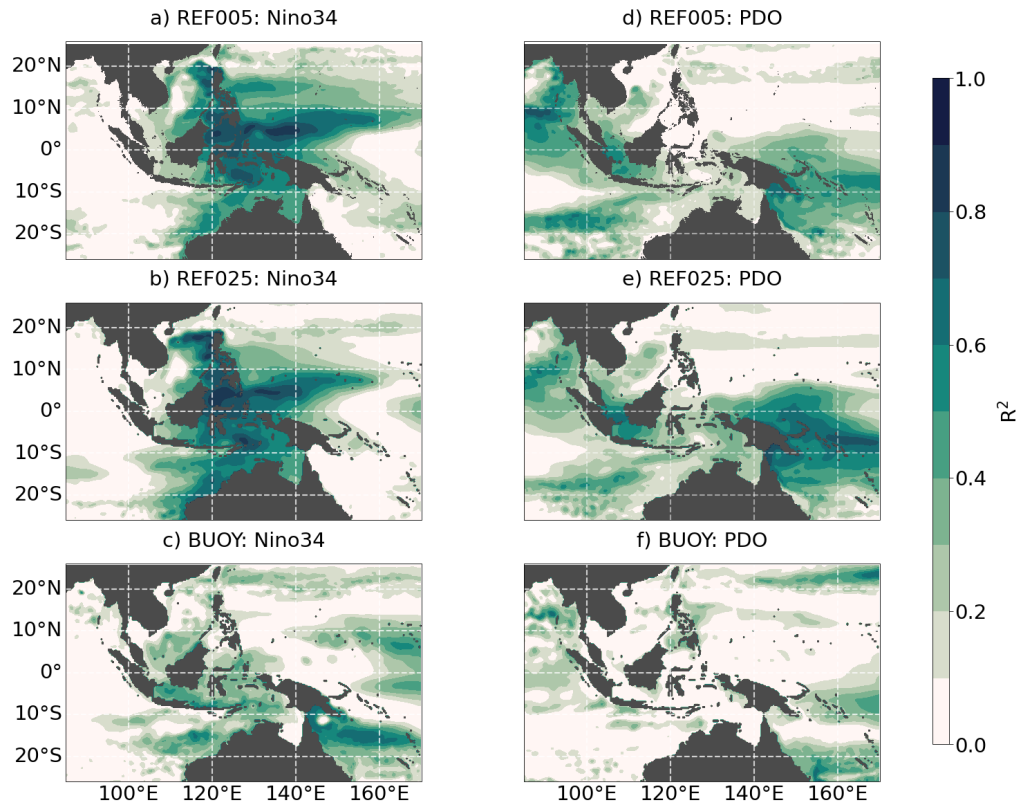


Fig. 5.6.: Coefficient of determination for the linear regression of SSH with the (a-c) Niño3.4 index and (d-f) PDO index for two hindcast (REF025, REF005) and buoyancy forcing experiments (BUOY). Climate indices are derived from the base model in the case of REF005 and from REF025 for the other two experiments. All data have been filtered with an 8-year low-pass filter.

of the ITF transport causes a reduction in heat and freshwater transport from the western tropical Pacific through the EAS, which causes negative thermosteric and halosteric SSH anomalies along the ITF pathway. In particular in the Banda Sea and Timor Sea, halosteric anomalies complement the thermosteric signal and make a relevant contribution (~ 1 cm) to the total signal of over 2 cm. Note, however, that thermosteric anomalies seem to originate from the warm pool region in the western tropical Pacific whereas halosteric anomalies are most pronounced in the EAS and the ITF outflow region in the Indian Ocean. This aspect is elaborated further two paragraphs below. Another question concerns the possibility of an asymmetric response to positive and negative ENSO phases. From an analysis of their individual contributions, we find that almost all regions with a non-negligible response to ENSO are characterized by similar amplitudes of SSH variability during both phases. Only the Arafura Sea responds more strongly to a negative cycle (not shown).

PDO-related changes are dominated by anomalies of the South Equatorial Current and the well-known SSH changes in the SPCZ region (Fig. 5.7 d-f). Negative SSH anomalies during a positive PDO cycle are due to thermosteric anomalies, which are partly compensated for by halosteric contributions. Negative anomalies change the pressure gradient along the coast of New Guinea and weaken the equatorward transport of warm and saline South Pacific waters via the New Guinea Coastal Current. This produces unfavourable conditions for South Pacific waters to enter the EAS, where we find negative thermosteric anomalies that are partly compensated for by positive halosteric anomalies, similar to the changes in the SPCZ.

The compensating effect of temperature (T) and salinity (S) changes during PDO cycles also manifests in the vertical profiles of temperature and salinity in the AMS. Figure 5.8 shows linear regressions of T and S averaged over the Banda Sea (7°S – 3°S , 125°E – 133°E ; see red box in Fig. 5.7). Both hindcast experiments (Fig. 5.4 a, b) indicate a strong, negative subsurface response (hence the density compensation) to positive PDO cycles. The ENSO response is dominated by a subsurface temperature anomaly causing negative SSH values. The subsurface temperature anomalies during both ENSO and PDO cycles are amplified by sea surface salinity (SSS) anomalies. The two sensitivity experiments allow some insight into the origin of these surface signals (Fig. 5.4 a, b). The momentum-flux experiment (WIND) reproduces the subsurface signals, highlighting the fact that they are due to wind-stress-driven advection, but shows no surface anomalies associated with ENSO and PDO cycles. These are instead driven by buoyancy fluxes. This fits the ENSO-related halosteric anomalies (Fig. 5.7 c) that do not seem to originate in the western tropical Pacific,

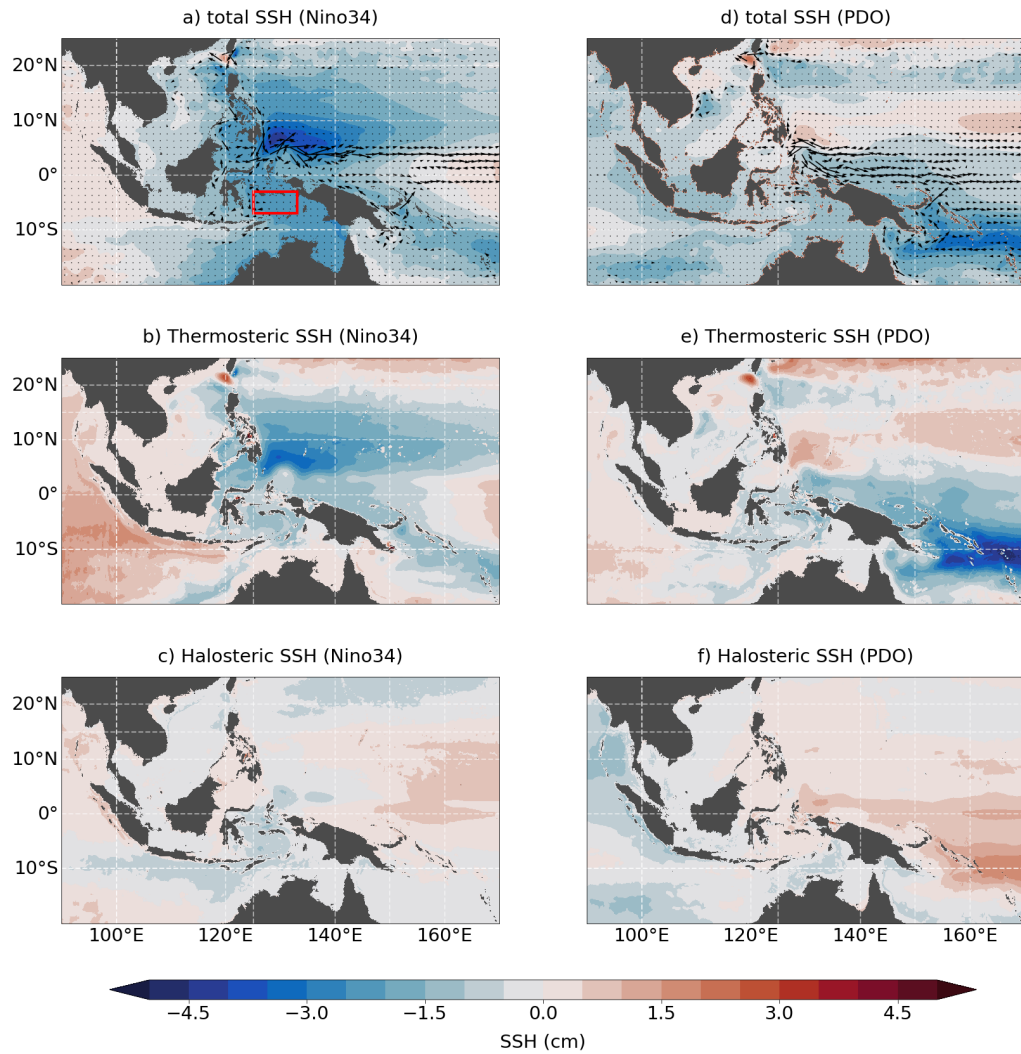


Fig. 5.7.: Linear regression with the (a-c) Niño3.4 and (d-f) PDO index of upper-ocean currents (arrows; 0–150 m) for total, thermosteric, and halosteric SSH. All data are taken from REF005 and were filtered with an 8-year low-pass filter. Note that the colour shading in panels a) and b) is the same as in Fig. 5.5a and b)

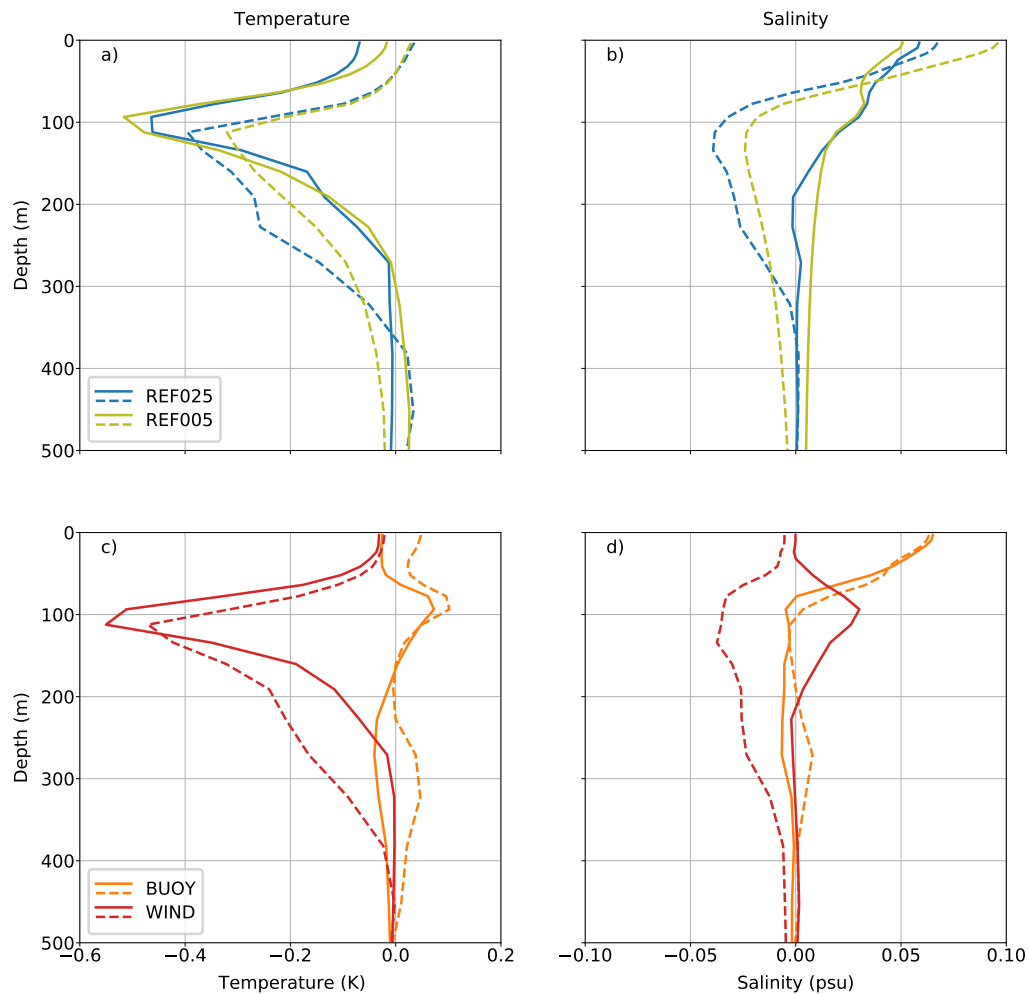


Fig. 5.8.: Linear regression of temperature and salinity with the Niño3.4 (solid) and PDO index (dashed) from (a, b) reference experiments and (c, d) sensitivity experiments. All data have been filtered with an 8-year low-pass filter.

but are instead forced by local buoyancy fluxes.

5.5 Summary and conclusion

5.5.1 Summary

We determine the characteristics of decadal sea-level variability in the Australasian Mediterranean Sea and their relation to large-scale climate modes of ENSO and PDO by using a series of global ocean model experiments. Two reference configurations

that resolve the area of interest with $\frac{1}{4}^\circ$ and $\frac{1}{20}^\circ$ horizontal resolution are set up and forced with the newly developed JRA55-do forcing (T sujino et al., 2018). Both simulations are able to reproduce observed sea-level variability in the western tropical Pacific and the AMS. We find minor resolution-dependent differences between both simulation in terms of SSH. However, the coarse-resolution configuration suffers from upper-ocean temperature and salinity biases, in particular in the northern part of the SCS and the Celebes Sea, which are alleviated in the high-resolution experiment.

We assess the regional fingerprints of ENSO and PDO on SSH in the region. Both climate modes produce strong sea-level signals in the western tropical Pacific. The ENSO-related signal is most pronounced just north of the Equator south of 10°N , which is in line with previous studies (e.g. Meng et al., 2019; Han et al., 2019). These strong SSH signals cause geostrophic flow anomalies as they change the inter-basin pressure gradient between the Pacific and the Indian Ocean and weaken the ITF (Hu et al., 2015). The imprint of the PDO in the northern part of the warm pool is weak and instead shifted southward. This confirms earlier reports which found the effect of the PDO (on multi-decadal timescales) in the western tropical Pacific to be most pronounced in the region of the SPCZ (Han et al., 2019; Moon et al., 2013; Becker et al., 2012). Our results suggest a partial compensation for thermosteric and halosteric PDO-related SSH anomalies. This is also in accordance with previous studies, which report a cooling and freshening of the southern part of the warm pool in response to a positive PDO cycle (Cravatte et al., 2009).

Within the AMS itself we find that, except for the central and northern SCS, over 80 % of the variability in the deep basins of the AMS is determined by low-frequency fluctuations of ENSO. The imprint of PDO cycles within the AMS is pronounced in the shallow Arafura, Timor and Java seas, where it explains 20 % and 50 % of the total variability, respectively. Analysing sea-level trends since the early 90s from altimetry, tide gauge observations and reconstructions, Strassburg et al. (2015) find similar results with respect to the PDO. Furthermore, our results suggest distinctly different patterns of variability related to ENSO and PDO in the SCS, where the ENSO pattern is limited to the northeastern part, off the west coast of Luzon, and the PDO causes anomalies in the central SCS. This confirms previous results of idealized model studies (Cheng et al., 2016).

It can be expected that a clarification of the spatial pattern of multi-decadal variability will aid future projections of sea level in the region. With the recent phase shift of the PDO, the affected regions should be primed for a weakening of the recent sea-level rise, as it is also observed in the western tropical Pacific (e.g. Hamlington et al., 2016; Piecuch et al., 2019).

In addition to two hindcast simulations, we set up a series of sensitivity experiments that use a repeated year forcing (Stewart et al., 2020) to remove interannual variability from the full forcing or only from the momentum or buoyancy fluxes. To our knowledge, the impact of buoyancy fluxes and intrinsic variability on regional sea level in the region has not been described in previous studies. Our results suggest that, even though momentum fluxes are the primary driver of variability, buoyancy fluxes are not negligible. According to our findings, they only contribute around 10 % on average to the total variability. However, this fraction is highly variable and can increase to up to 50 % during ENSO cycles when they amplify the wind-stress-driven sea-level anomalies. Indeed, buoyancy fluxes have been shown to be important for sea-level variability in other regions, including the tropical Pacific (Piecuch and Ponte, 2012; Ponte, 2012; Wagner et al., 2021). Intrinsic variability is relevant in the central SCS, where it accounts for 25 % of the low-frequency variability.

5.5.2 Discussion

We did not investigate the origin of the high levels of intrinsic variability in the SCS in detail and can only speculate at this point. A connection to mesoscale variability and the eddy-active Kuroshio region, which also shows high levels of intrinsic variability (Fig. 5.4 e), seems likely. Both regions are connected via the Luzon Strait between Taiwan and the Philippines, and both regions show high levels of eddy kinetic energy (EKE; e.g. Scharffenberg and Stammer 2010). Besides local (Wang et al., 2008) and remote (Chen et al., 2009; Cheng and Qi, 2010) wind forcing, the Luzon Strait transport (LST) has been identified in previous studies as driving interannual EKE variability in the SCS. An increased LST leads to a strengthening of the mean flow in the SCS, which creates favourable conditions for baroclinic instabilities that allow a downscale energy transfer (Sun et al., 2016). The strength of the LST is closely related to the Kuroshio current intrusion into the SCS (Qu et al., 2004; Wang and Fiedler, 2006) and the strength of the Kuroshio current itself. The Kuroshio current flows poleward along the western boundary, at which the Luzon Strait creates a gap through which the current can enter the SCS. The mechanisms

that control the pathways and strength of this intrusion are complex and remain controversial (Nan et al. 2015 and references therein), but also include mechanisms by which eddies, generated by intrinsic variability in the Kuroshio region, impact the LST. While eddies are unlikely to cross the Luzon Strait directly, they have been observed to modulate the strength of the Kuroshio current (Jie and De-Hai, 2010), which could be a means by which intrinsic variability from the Kuroshio region is indirectly communicated into the SCS. However, the viability of this hypothesis and the determination of the mechanism involved need to be addressed in future research.

The aim of this study is to identify the deterministic low-frequency pattern of variability associated with large-scale climate modes. Although the separation of climate indices along timescales (ENSO: 8–13 years; PDO: > 13 years) is somewhat arbitrary, the results are not overly sensitive to the choice of the separation frequency. In fact, using only a low-pass-filtered ENSO index (> 8 years) yields results that are similar to the combined effect of bandpass-filtered ENSO and low-pass-filtered PDO we presented here. As already mentioned above, the PDO can be understood as the low-frequency component of ENSO in this context, and separating the timescales allowed us to show that the spatial pattern of SSH variability in the AMS, and the mechanisms that drive it, differ over these timescales.

An uncertainty of this study is the atmospheric forcing product used to drive the OGCMs. McGregor et al. (2012a) demonstrated that most available atmospheric reanalyses, in conjunction with a linear shallow-water model, are able to reproduce the large-scale pattern of SSH variability in the Pacific and we can confirm this for the dataset used here. However, we find minor biases in both reference configurations that are most likely due to the forcing. Hsu et al. (2021) report a wind-stress curl bias in JRA55-do in the Pacific between 4 and 9° N that acts to diminish the meridional SSH gradient and flatten the SSH trough at this latitude. This is consistent with the warm bias we find at this latitudinal band. Also, consistent with the results found here, they further report an underestimation of SSH trends between 1993 and 2007 in the western tropical Pacific and relate it to an underestimation of the observed trade wind intensification.

A final point concerns the impact of model resolution in studies of variability patterns in this region. Although in our study we find only minor resolution-dependent differences between the $\frac{1}{4}^\circ$ and $\frac{1}{20}^\circ$ configurations with respect to SSH signals, the

stronger biases in the temperature and salinity distributions seen in the coarser simulation should be taken as a reminder that a realistic representation of the dynamics of the AMS area with its complex, small-scale bathymetry can require a very high model resolution. The importance of resolving the narrow straits and bathymetric details for capturing the ocean dynamics in the AMS was recently stressed in a review by Xue et al. (2020) of coupled ocean–atmosphere modelling for this region. In this context, it should be noted that the "coarse" $\frac{1}{4}^\circ$ -grid used in this study would rather be in the higher-resolution category of current climate simulations with coupled ocean-atmosphere models, suggesting that projections of regional trend patterns in this area need to be interpreted with due caution. Downscaled projections (e.g. Sun et al., 2012; Feng et al., 2017), in which an uncoupled high-resolution OGCM is forced with a long-term climate change signal obtained from a climate model, might be a way to address this issue.

Summary and conclusion

The overall aim of this thesis is to determine the driving mechanism of regional sea-level variability in the Indo-Pacific region. To achieve this, I developed a new modelling framework that includes a series of sensitivity experiments based on a so-called "repeated year forcing" (RYF; Stewart et al., 2020) and a high-resolution configuration. The first challenge, addressed in chapter 3, is to evaluate the RYF-approach as a way to conduct climatological experiments with the novel JRA55-do forcing (Tsujino et al., 2018). The RYF-approach allows to complement an existing interannually varying forcing dataset with a climatological forcing by selecting a single year that is used repeatedly for as many cycles as needed. This procedure bears the task of choosing an appropriate year. Based on work by Stewart et al. (2020), three different RYF-periods are tested (May 1st to April 31st of the years 1984-85, 1990-91, 2003-04 are denoted as RYF84, RYF90 and RYF03). All RYF-experiments allow for a successful integration of a 59-year-long experiment. The long-term behaviour of all analysed quantities is comparable, i.e. trend estimates agree in terms of trend direction and magnitude. RYF03 is identified as the least suitable candidate because it produces the largest discrepancies in terms of the trends and mean states of several quantities. In particular, the mixed layer depth in the North Atlantic is not representative of that of the hindcast simulation. Beyond that, the choice of a single RYF-period should be based on statistical and physical considerations specific to the research question, but RYF84 and RYF90 yield consistent trend estimates for the example provided here. A limitation of the approach concerns the uncertainty of the trend estimates that is not easily obtained. With regard to the first question stated in chapter 1 this leads to the following conclusion:

(C1) The RYF methodology in general, and two out of the three tested RYF-periods in particular, are suited to force climatological experiments. They allow for the analysis of the model drift and transients over a typical hindcast period of several decades that is representative for an accompanying hindcast experiment.

The results of chapter 3 serve as a basis for the following chapters in which the RYF-approach is used for sensitivity experiments that suppresses the interannual variability of ocean–atmosphere buoyancy and momentum fluxes to assess their individual importance for interannual to decadal sea-level variability. In chapter 4, I demonstrate how buoyancy fluxes modify the predominantly wind-stress-driven variability in the tropical Pacific on interannual to decadal timescales. While wind stress drives a zonal dipole with opposing changes in the western and eastern basin, buoyancy fluxes are centred in the central to eastern tropical Pacific where they trigger sea-level anomalies that propagate westward as equatorial Rossby waves. The variability of wind stress as well as of buoyancy fluxes is closely correlated to El Niño–Southern Oscillation (ENSO). Due to their different spatial pattern, the resulting sea-level anomalies are correlated in the eastern part of the basin and anti-correlated in the west. To conclude:

(C2) Sea-level changes in the tropical Pacific driven by wind-stress and buoyancy fluxes are both closely correlated to ENSO on interannual to decadal timescales. Buoyancy fluxes tend to counteract the wind-stress-driven changes in the western part of the basin, where heat and freshwater fluxes contribute to variability on interannual to decadal timescales, but complement it in the east, where heat fluxes drive interannual sea-level variability.

The analysis is extended westward into the marginal seas connecting the Indian and Pacific Oceans: the Australasian Mediterranean Sea (AMS). In order to facilitate long-term sea-level projections, decadal variability is emphasized since it potentially mask long-term trends and therefore needs to be accounted for in future sea-level projections. To cope with the small-scale bathymetry of the region, with its many small seas and straits, I set up a new high-resolution ocean model configuration named NUSA20. NUSA20 is able to improve the representation of sea-level variability in general, in particular in the region of the East Australian Current and the Tasman Front and the southeastern Indian Ocean. Moreover, it alleviates upper-ocean biases of temperature and salinity in the AMS, which are found in the coarse-resolution configuration. With respect to the initially stated third question, the results can be summarized as follows:

(C3) Decadal sea-level variability in the AMS is dominated by fluctuations of ENSO that account for over 80 % of the variability along the pathway of the Indonesian Throughflow (ITF) and in the northwestern South China Sea (SCS). Buoyancy fluxes contribute about 10 % to the total variability on average. In-

trinsic variability is relevant in the SCS where it accounts for 25 % of the variability but is negligible elsewhere.

Overall, with this thesis, I provide an assessment of the RYF-approach with JRA55-do forcing with respect to model drifts and transients in a global $\frac{1}{4}^\circ$ OGCM simulation. A practical application includes sensitivity experiments that utilize the RYF-approach, corresponding reference simulations and a newly developed high-resolution configuration. Using this comprehensive modelling framework, I demonstrate the importance of ocean–atmosphere buoyancy fluxes, explicitly including freshwater, for sea-level variability in the tropical Pacific. With respect to the AMS, I illustrate the importance of Pacific climate modes for sea-level variability in the AMS and of intrinsic variability in the SCS.

Nevertheless, open questions remain or emerged during this work to which the last section is reserved.

6.1 Open questions

6.1.1 Small-scale limit of sensitivity experiments

This thesis is concerned with wind and buoyancy forcing and their individual contribution to sea-level variability. Dedicated sensitivity experiments are used to isolate both. Two assumptions are vital in this respect. First, the total variability is a linear combination of variability driven by wind-stress and buoyancy fluxes. Second, sensitivity experiments are able to isolate both kinds of variability. The first requirement may be violated by non-linear effects, for example due to non-linearities in the equation of state. The second one (albeit not exclusively) by intrinsic variability, i.e. variability that is not directly forced by the atmosphere and that may be included in all sensitivity experiments. Both points are discussed in chapters 4 and 5 in an attempt to quantify the errors for the presented analysis. As mesoscale sea-level variability is largely of intrinsic origin (e.g. Sérazin et al., 2015) and ocean models resolve more and more of these small scales and non-linear processes, the question arises whether there is a small-scale limit to the methodology.

6.1.2 Effect of different El Niño types on tropical Pacific sea level

Another issue concerns the effect of different types of El Niño on the presented results regarding sea-level variability. In particular, two types can be distinguished: the Eastern Pacific (EP) type and the Central Pacific (CP) type. The EP type describes the classical El Niño with maximum sea-surface-temperature (SST) anomalies in the eastern Pacific. During a CP type El Niño, also called El Niño Modoki, Warm Pool El Niño or Date Line El Niño, these SST anomalies shift westward and are centred around the International Dateline (e.g. Ashok et al., 2007; Kao and Yu, 2009; Kug et al., 2009). As a consequence, anomalies in the eastern and western part of the basin are not as pronounced as during an EP type El Niño. The issue is relevant because the occurrence of CP type El Niño events increased in recent decades and is even the predominant type since 2000. The El Niños of 2002-03, 2004-05 and 2009-10 have all been CP type El Niños (e.g. Ashok et al., 2007; Lee and McPhaden, 2010; Wang et al., 2017). Some studies also report a projected increase of the CP type with global warming (Yeh et al., 2009). Considering the described differences in SST pattern between both El Niño types, a correspondingly different response in SSH variability and implications for the analyses on sea level in the tropical Pacific and the AMS seem likely. Figure 4.5 does indeed suggest a reduced sea-level response to positive ENSO cycles in the eastern and western tropical Pacific after 2000. Both El Niño types are also associated with different precipitation anomalies, rendering implications for buoyancy-flux-driven sea-level variability possible. The EP type is associated with strong, positive precipitation anomalies in the central Pacific (see section 4.5). The CP type shows much weaker anomalies that are shifted to the west and even negative anomalies in the east (Kao and Yu, 2009; Kug et al., 2009). This is consistent with the results presented here which show strong halosteric SSH anomalies in response to ENSO cycles and due to buoyancy fluxes in the central Pacific prior to 2000 but only weak anomalies after that year (Fig. 4.7). However, these hypotheses need to be thoroughly tested in future analyses.

6.1.3 The mechanism behind the ITF transport reduction

The ITF is projected to decrease under global warming (Sen Gupta et al., 2016; Feng et al., 2017; Ma et al., 2020). Besides the implication for the Pacific heat content, a reduced ITF transport might also be relevant for the sea-level variability in the AMS because it causes a reduced inflow of heat. The mechanism behind this trend are under debate. Based on coupled models and downscaled climate projections, Sen Gupta et al. (2016) and Feng et al. (2017) suggest that the decline is not forced by

wind-stress changes but is instead related to a reduction of deep Pacific upwelling and an associated reduction of Antarctic Bottom Water (AABW) inflow from the Southern Ocean into the Pacific. However, the driver of this remains elusive. An alternative hypothesis, supported by a hierarchy of models from shallow water to climate models, claims the ITF reduction to be part of a transient overturning compensation between the Atlantic and Indo-Pacific Oceans. Furthermore, it is stated that the reduction in deep upwelling is a consequence of the ITF decrease rather than its forcing mechanism (Sun et al., 2020; Sun and Thompson, 2020).

A robust ITF transport decline is found in all RYF-experiments (Fig. 3.10). These trends should be considered spurious. However, the associated mechanisms might still be realistic. The close linkage between the ITF trends and the deep Pacific upwelling is already discussed in section 3.4.3 (Fig. 3.10). Furthermore, respective changes in the vertical velocity appear to be distributed across the basin and are not associated with particular regions (Fig. 6.1 a) but the reduction in deep northward transport into the Pacific across 40°S is associated with AABW just east of New Zealand along the continental shelf (Fig. 6.1 b). These patterns are robust in all RYF-experiments (not shown) and similarly described by Sen Gupta et al. (2016) and Feng et al. (2017) for the projected ITF decline in the 21st century. Consequently, the RYF-experiments might be used to investigating the origin and the forcing mechanism of this declining ITF transport.

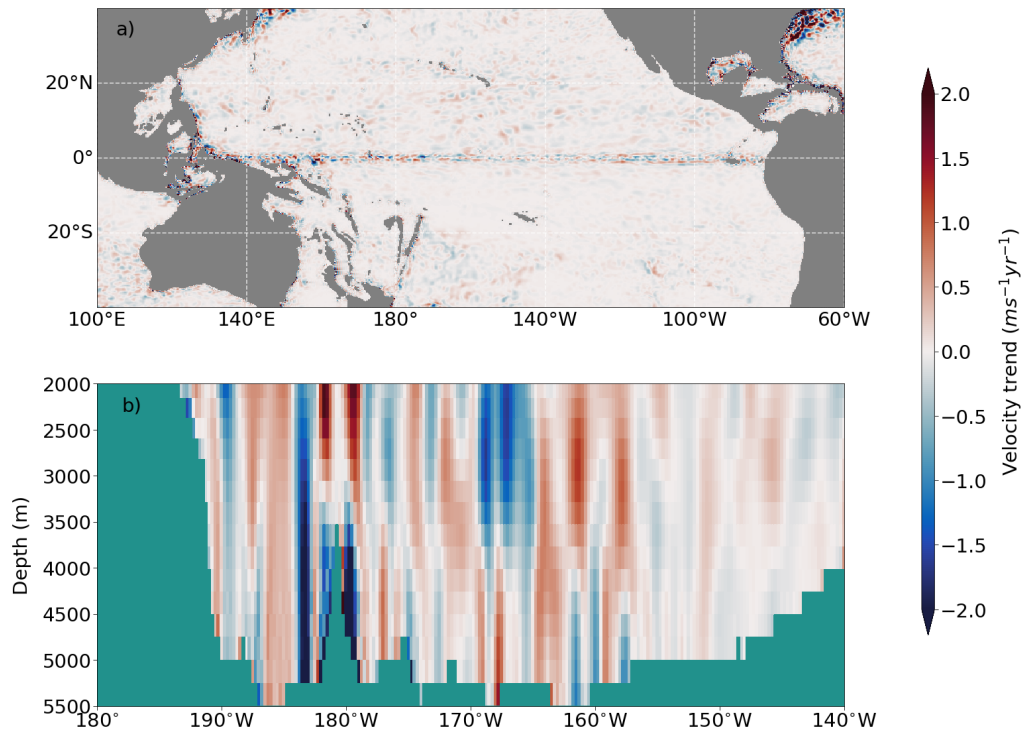


Fig. 6.1.: Trend of (a) vertical and (b) meridional velocities over the last 50 year of the experiment RYF84. Vertical and meridional velocities trends are scaled with factors 10^7 and 10^4 , respectively, to facilitate a common colourbar.

Bibliography

- Ablain, M., Cazenave, A., Larnicol, G., Balmaseda, M., Cipollini, P., Faugère, Y., Fernandes, M. J., Henry, O., Johannessen, J. A., Knudsen, P., Andersen, O., Legeais, J., Meyssignac, B., Picot, N., Roca, M., Rudenko, S., Scharffenberg, M. G., Stammer, D., Timms, G., and Benveniste, J. (2015). Improved sea level record over the satellite altimetry era (1993-2010) from the Climate Change Initiative project. *Ocean Science*, 11(1):67–82.
- Amante, C. and Eakins, B. (2009). ETOPO1 1 Arc-Minute Global Relief Model: Procedures, Data Sources and Analysis. NOAA Technical Memorandum NESDIS NGDC-24. Technical report, National Geophysical Data Center, NOAA.
- Arakawa, A. and Lamb, V. (1977). Computational Design of the Basic Dynamical Processes of the UCLA General Circulation Model. *Methods in Computational Physics: Advances in Research and Applications*, 17:173–265.
- Ashok, K., Behera, S. K., Rao, S. A., Weng, H., and Yamagata, T. (2007). El Niño Modoki and its possible teleconnection. *Journal of Geophysical Research: Oceans*, 112:C11007.
- Barnier, B., Brodeau, L., LeSommer, J., Molines, J. M., Penduff, T., Theetten, S., Treguier, A.-M., Madec, G., Biastoch, A., Böning, C. W., Dengg, J., Gulev, S., Bourdalle-Badié, R., Chanut, J., Garric, G., Alderson, S., Coward, A. C., De Cuevas, B., New, A., Haines, K., Smith, G., Drijfhout, S., Hazeleger, W., Severijns, C., and Myers, P. (2007). Eddy-permitting Ocean Circulation Hindcasts Of Past Decades. *CLIVAR exchanges*, 37(3):8–10.
- Barnier, B., Madec, G., Penduff, T., Molines, J. M., Treguier, A. M., Le Sommer, J., Beckmann, A., Biastoch, A., Böning, C., Dengg, J., Derval, C., Durand, E., Gulev, S., Remy, E., Talandier, C., Theetten, S., Maltrud, M., McClean, J., and De Cuevas, B. (2006). Impact of partial steps and momentum advection schemes in a global ocean circulation model at eddy-permitting resolution. *Ocean Dynamics*, 56(5-6):543–567.
- Becker, M., Meyssignac, B., Letetrel, C., Llovel, W., Cazenave, A., and Delcroix, T. (2012). Sea level variations at tropical Pacific islands since 1950. *Global and Planetary Change*, 80-81:85–98.

- Biastoch, A., Böning, C. W., Schwarzkopf, F. U., and Lutjeharms, J. (2009). Increase in Agulhas leakage due to poleward shift of Southern Hemisphere westerlies. *Nature*, 462:495–498.
- Bingham, R. J. and Hughes, C. W. (2012). Local diagnostics to estimate density-induced sea level variations over topography and along coastlines. *Journal of Geophysical Research: Oceans*, 117:C01013.
- Boyer, T. P., Antonov, J. I., Baranova, O. K., Coleman, C., Garcia, H. E., Grodsky, A., Johnson, D. R., Locarnini, R. a., Mishonov, A. V., O'Brien, T. D., Paver, C. R., Reagan, J. R., Seidov, D., Smolyar, I. V., Zweng, M. M., Brien, T. D. O., Paver, C. R., Reagan, J. R., Seidov, D., Smolyar, I. V., Zweng, M. M., and Sullivan, K. D. (2013). WORLD OCEAN DATABASE 2013, NOAA Atlas NESDIS 72. Technical report, National Oceanic and Atmospheric Administration.
- Boyer, T. P., García, H. E., Locarnini, R. A., Zweng, M. M., Mishonov, A. V., Reagan, J. R., Weathers, K. A., Baranova, O. K., Paver, C. R., Seidov, D., and Smolyar, I. V. (n.d.). World ocean atlas 2018. <https://www.ncei.noaa.gov/archive/accession/NCEI-WOA18>. Last access: 16 February 2021.
- Brunke, M. A., Wang, Z., Zeng, X., Bosilovich, M., and Shie, C. L. (2011). An assessment of the uncertainties in ocean surface turbulent fluxes in 11 reanalysis, satellite-derived, and combined global datasets. *Journal of Climate*, 24(21):5469–5493.
- Carret, A., Llovel, W., Penduff, T., and Molines, J. M. (2021). Atmospherically Forced and Chaotic Interannual Variability of Regional Sea Level and Its Components Over 1993–2015. *Journal of Geophysical Research: Oceans*, 126:e2020JC017123.
- Carson, M., Köhl, A., Stammer, D., Meyssignac, B., Church, J., Schröter, J., Wenzel, M., and Hamlington, B. (2017). Regional sea level variability and trends , 1960 – 2007 - A comparison of sea level reconstructions and ocean syntheses. *Journal of Geophysical Research: Oceans*, 122:1–24.
- Carton, J. A., Giese, B. S., and Grodsky, S. A. (2005). Sea level rise and the warming of the oceans in the Simple Ocean Data Assimilation (SODA) ocean reanalysis. *Journal of Geophysical Research: Oceans*, 110(9):1–8.
- Cazenave, A., Henry, O., Munier, S., Delcroix, T., Gordon, A. L., Meyssignac, B., Llovel, W., Palanisamy, H., and Becker, M. (2012). Estimating ENSO Influence on the Global Mean Sea Level, 1993-2010. *Marine Geodesy*, 35(sup1):82–97.

- Chen, G., Hou, Y., Chu, X., Qi, P., and Hu, P. (2009). The variability of eddy kinetic energy in the South China Sea deduced from satellite altimeter data. *Chinese Journal of Oceanology and Limnology*, 27(4):943–954.
- Cheng, X. and Qi, Y. (2007). Trends of sea level variations in the South China Sea from merged altimetry data. *Global and Planetary Change*, 57(3-4):371–382.
- Cheng, X. and Qi, Y. (2010). Variations of eddy kinetic energy in the South China Sea. *Journal of Oceanography*, 66(1):85–94.
- Cheng, X., Xie, S. P., Du, Y., Wang, J., Chen, X., and Wang, J. (2016). Interannual-to-decadal variability and trends of sea level in the South China Sea. *Climate Dynamics*, 46(9-10):3113–3126.
- Church, J. A. and White, N. J. (2011). Sea-Level Rise from the Late 19th to the Early 21st Century. *Surveys in Geophysics*, 32(4-5):585–602.
- Clarke, A. J. (2010). Analytical Theory for the Quasi-Steady and Low-Frequency Equatorial Ocean Response to Wind Forcing: The "Tilt" and "Warm Water Volume" Modes. *Journal of Physical Oceanography*, 40:121–137.
- Clarke, A. J. and Liu, X. (1994). Interannual Sea Level in the Northern and Eastern Indian Ocean. *Journal of Physical Oceanography*, 24(6):1224–1235.
- Close, S., Penduff, T., Speich, S., and Molines, J. M. (2020). A means of estimating the intrinsic and atmospherically-forced contributions to sea surface height variability applied to altimetric observations. *Progress in Oceanography*, 184:102314.
- CMEMS (n.d.). Global ocean gridded l4 sea surface heights and derived variables reprocessed. https://resources.marine.copernicus.eu/?option=com_csw&view=details&product_id=SEALEVEL_GLO_PHY_L4_REP_OBSERVATIONS_008_047. Last access: 12 June 2018.
- Cravatte, S., Delcroix, T., Zhang, D., McPhaden, M., and Leloup, J. (2009). Observed freshening and warming of the western Pacific Warm Pool. *Climate Dynamics*, 33(4):565–589.
- Danabasoglu, G., Yeager, S. G., Kim, W. M., Behrens, E., Bentsen, M., Bi, D., Biastoch, A., Bleck, R., Böning, C., Bozec, A., Canuto, V. M., Cassou, C., Chassignet, E., Coward, A. C., Danilov, S., Diansky, N., Drange, H., Farneti, R., Fernandez, E., Fogli, P. G., Forget, G., Fujii, Y., Griffies, S. M., Gusev, A., Heimbach, P., Howard, A., Ilicak, M., Jung, T., Karspeck, A. R., Kelley, M., Large, W. G., Leboissetier, A., Lu, J., Madec, G., Marsland, S. J., Masina, S., Navarra, A., Nurser, A. J., Pirani, A., Romanou, A., yMélia David, S., Samuels, B. L., Scheinert, M., Sidorenko, D.,

- Sun, S., Treguier, A. M., Tsujino, H., Uotila, P., Valcke, S., Voldoire, A., Wang, Q., and Yashayaev, I. (2016). North Atlantic simulations in Coordinated Ocean-ice Reference Experiments phase II (CORE-II). Part II: Inter-annual to decadal variability. *Ocean Modelling*, 97:65–90.
- Dangendorf, S., Marcos, M., Wöppelmann, G., Conrad, C. P., Frederikse, T., and Riva, R. (2017). Reassessment of 20th century global mean sea level rise. *Proceedings of the National Academy of Sciences of the United States of America*, 114(23):5946–5951.
- Debreu, L., Vouland, C., and Blayo, E. (2008). AGRIF: Adaptive grid refinement in Fortran. *Computers and Geosciences*, 34(1):8–13.
- Delcroix, T. (1998). Observed surface oceanic and atmospheric variability in the tropical Pacific at seasonal and ENSO timescales : A tentative overview. *Journal of Geophysical Research*, 103(C9):18611–18633.
- Duteil, O., Böning, C. W., and Oschlies, A. (2014). Variability in subtropical-tropical cells drives oxygen levels in the tropical Pacific Ocean. *Geophysical Research Letters*, 41(24):8926–8934.
- Fang, G., Chen, H., Wei, Z., Wang, Y., Wang, X., and Li, C. (2006). Trends and interannual variability of the South China Sea surface winds, surface height, and surface temperature in the recent decade. *Journal of Geophysical Research: Oceans*, 111:C11S16.
- Farneti, R., Downes, S. M., Griffies, S. M., Marsland, S. J., Behrens, E., Bentsen, M., Bi, D., Biastoch, A., Böning, C., Bozec, A., Canuto, V. M., Chassignet, E., Danabasoglu, G., Danilov, S., Diansky, N., Drange, H., Fogli, P. G., Gusev, A., Hallberg, R. W., Howard, A., Ilicak, M., Jung, T., Kelley, M., Large, W. G., Leboissetier, A., Long, M., Lu, J., Masina, S., Mishra, A., Navarra, A., George Nurser, A. J., Patara, L., Samuels, B. L., Sidorenko, D., Tsujino, H., Uotila, P., Wang, Q., and Yeager, S. G. (2015). An assessment of Antarctic Circumpolar Current and Southern Ocean meridional overturning circulation during 1958-2007 in a suite of interannual CORE-II simulations. *Ocean Modelling*, 93:84–120.
- Feng, M., Benthuisen, J., Zhang, N., and Slawinski, D. (2015). Freshening anomalies in the Indonesian throughflow and impacts on the Leeuwin Current during 2010-2011. *Geophysical Research Letters*, 42(20):8555–8562.
- Feng, M., Böning, C., Biastoch, A., Behrens, E., Weller, E., and Masumoto, Y. (2011). The reversal of the multi-decadal trends of the equatorial Pacific easterly winds,

- and the Indonesian Throughflow and Leeuwin Current transports. *Geophysical Research Letters*, 38:L11604.
- Feng, M., Li, Y., and Meyers, G. (2004). Multidecadal variations of Fremantle sea level: Footprint of climate variability in the tropical Pacific. *Geophysical Research Letters*, 31:L16302.
- Feng, M., Zhang, N., Liu, Q., and Wijffels, S. (2018). The Indonesian throughflow, its variability and centennial change. *Geoscience Letters*, 5(1).
- Feng, M., Zhang, X., Sloyan, B., and Chamberlain, M. (2017). Contribution of the deep ocean to the centennial changes of the Indonesian Throughflow. *Geophysical Research Letters*, 44:2859–2867.
- Fenoglio-Marc, L., Schöne, T., Illigner, J., Becker, M., Manurung, P., and Khafid (2012). Sea Level Change and Vertical Motion from Satellite Altimetry, Tide Gauges and GPS in the Indonesian Region. *Marine Geodesy*, 35(S1):137–150.
- Fichefet, T. and Maqueda, M. A. M. (1997). Sensitivity of a global sea ice model to the treatment of ice thermodynamics and dynamics. *Journal of Geophysical Research: Oceans*, 102(C6):12609–12646.
- Forget, G. and Ponte, R. M. (2015). The partition of regional sea level variability. *Progress in Oceanography*, 137:173–195.
- Fukumori, I. and Wang, O. (2013). Origins of heat and freshwater anomalies underlying regional decadal sea level trends. *Geophysical Research Letters*, 40(3):563–567.
- Gill, A. E. (1982). *Atmosphere-ocean dynamics*. Academic Press, New York.
- Godfrey, J. S. (1989). A Sverdrup model of the depth-integrated flow for the world ocean allowing for island circulations. *Geophysical & Astrophysical Fluid Dynamics*, 45(1-2):89–112.
- Gordon, A. L. (1986). Interocean exchange of thermocline water. *Journal of Geophysical Research*, 91(C4):5037–5046.
- Gordon, A. L. (2005). Oceanography of the Indonesian seas and their throughflow. *Oceanography*, 18(4):15–27.
- Gordon, A. L., Huber, B. A., Metzger, E. J., Susanto, R. D., Hurlburt, H. E., and Adi, T. R. (2012). South China Sea throughflow impact on the Indonesian throughflow. *Geophysical Research Letters*, 39:L11602.

- Gordon, A. L., Napitu, A., Huber, B. A., Gruenburg, L. K., Pujiana, K., Agustiad, T., Kuswardani, A., Mbay, N., and Setiawan, A. (2019). Makassar Strait Through-flow Seasonal and Interannual Variability: An Overview. *Journal of Geophysical Research: Oceans*, 124:3724–3736.
- Greatbatch, R. J. (1994). A note on the representation of steric sea level in models that conserve volume rather than mass. *Journal of Geophysical Research*, 99(C6):12767.
- Greatbatch, R. J., Zhu, X., and Claus, M. (2018). Reconstructing Tropical Pacific Sea Level Variability for the Period 1961–2002 Using a Linear Multimode Model. *Journal of Geophysical Research: Oceans*, 123:2037–2048.
- Griffies, S. M., Biastoch, A., Böning, C., Bryan, F., Danabasoglu, G., Chassignet, E. P., England, M. H., Gerdes, R., Haak, H., Hallberg, R. W., Hazeleger, W., Jungclaus, J., Large, W. G., Madec, G., Pirani, A., Samuels, B. L., Scheinert, M., Gupta, A. S., Severijns, C. A., Simmons, H. L., Treguier, A. M., Winton, M., Yeager, S., and Yin, J. (2009). Coordinated Ocean-ice Reference Experiments (COREs). *Ocean Modelling*, 26(1-2):1–46.
- Griffies, S. M., Winton, M., Samuels, B., Danabasoglu, G., Yeager, S., Marsland, S., Drange, H., and Bentsen, M. (2012). Datasets and protocol for the CLIVAR WGOMD Coordinated Ocean-sea ice Reference Experiments (COREs). Technical report, Clivar.
- Griffies, S. M., Yin, J., Durack, P. J., Goddard, P., Bates, S. C., Behrens, E., Bentsen, M., Bi, D., Biastoch, A., Böning, C. W., Bozec, A., Chassignet, E., Danabasoglu, G., Danilov, S., Domingues, C. M., Drange, H., Farneti, R., Fernandez, E., Greatbatch, R. J., Holland, D. M., Ilicak, M., Large, W. G., Lorbacher, K., Lu, J., Marsland, S. J., Mishra, A., George Nurser, A. J., Salas y Méliá, D., Palter, J. B., Samuels, B. L., Schröter, J., Schwarzkopf, F. U., Sidorenko, D., Treguier, A. M., heng Tseng, Y., Tsujino, H., Uotila, P., Valcke, S., Voldoire, A., Wang, Q., Winton, M., and Zhang, X. (2014). An assessment of global and regional sea level for years 1993-2007 in a suite of interannual core-II simulations. *Ocean Modelling*, 78:35–89.
- Gulev, S. K. (1994). Influence of Space-Time Averaging on the Ocean-Atmosphere Exchange Estimates in the North Atlantic Midlatitudes. *Journal of Physical Oceanography*, 24(6):1236–1255.
- Hamlington, B. D., Cheon, S., Thompson, P. R., Merrifield, M. A., Nerem, R. S., Leben, R. R., and Kim, K.-Y. (2016). An ongoing shift in Pacific Ocean sea level. *Journal of Geophysical Research: Oceans*, 121:5084–5097.

- Hammond, W. C., Burgette, R. J., Johnson, K. M., and Blewitt, G. (2018). Uplift of the Western Transverse Ranges and Ventura Area of Southern California: A Four-Technique Geodetic Study Combining GPS, InSAR, Leveling, and Tide Gauges. *Journal of Geophysical Research: Solid Earth*, 123:836–858.
- Han, W., Meehl, G. a., Rajagopalan, B., Fasullo, J. T., Hu, A., Lin, J., Large, W. G., Wang, J.-w., Quan, X.-W., Trenary, L. L., Wallcraft, A., Shinoda, T., and Yeager, S. (2010). Patterns of Indian Ocean sea-level change in a warming climate. *Nature Geoscience*, 3(8):546–550.
- Han, W., Meehl, G. A., Stammer, D., Hu, A., Hamlington, B., Kenigson, J., Palanisamy, H., and Thompson, P. (2017). Spatial Patterns of Sea Level Variability Associated with Natural Internal Climate Modes. *Surveys in Geophysics*, 38:217–250.
- Han, W., Stammer, D., Thompson, P., Ezer, T., Palanisamy, H., Zhang, X., Domingues, C. M., Zhang, L., and Yuan, D. (2019). Impacts of Basin-Scale Climate Modes on Coastal Sea Level: a Review. *Surveys in Geophysics*, 40(6):1493–1541.
- Holgate, S. J., Matthews, A., Woodworth, P. L., Rickards, L. J., Tamisiea, M. E., Bradshaw, E., Foden, P. R., Gordon, K. M., Jevrejeva, S., and Pugh, J. (2012). New Data Systems and Products at the Permanent Service for Mean Sea Level. *Journal of Coastal Research*, 29(3):493–504.
- Hsu, C.-W., Yin, J., Griffies, S., and Dussin, R. (2021). A Mechanistic Analysis of Tropical Pacific Dynamic Sea Level in GFDL-OM4 under OMIP-I and OMIP-II Forcings. *Geoscientific Model Development Discussions*, 14:2471–2502.
- Hu, D., Wu, L., Cai, W., Gupta, A. S., Ganachaud, A., Qiu, B., Gordon, A. L., Lin, X., Chen, Z., Hu, S., Wang, G., Wang, Q., Sprintall, J., Qu, T., Kashino, Y., Wang, F., and Kessler, W. S. (2015). Pacific western boundary currents and their roles in climate. *Nature*, 522:299–308.
- Huber, B. A. (2019). Data from: Makassar strait throughflow seasonal and interannual variability: An overview. <https://doi.org/10.7916/d8-p78a-zm51>. Last access: 27 January 2021.
- Hughes, P. J., Bourassa, M. A., Rolph, J. J., and Smith, S. R. (2012). Averaging-related biases in monthly latent heat fluxes. *Journal of Atmospheric and Oceanic Technology*, 29(7):974–986.
- International Hydrographic Organisation (1953). *Limits of Oceans and Seas*. IMP, Monte-Carlo, 3 edition.

- Jevrejeva, S., Moore, J. C., Grinsted, A., Matthews, A. P., and Spada, G. (2014). Trends and acceleration in global and regional sea levels since 1807. *Global and Planetary Change*, 113:11–22.
- Jie, Z. and De-Hai, L. (2010). Response of the Kuroshio Current to Eddies in the Luzon Strait. *Atmospheric and Oceanic Science Letters*, 3(3):160–164.
- Jin, X., Kwon, Y.-O., Ummenhofer, C. C., Seo, H., Schwarzkopf, F. U., Biastoch, A., Böning, C. W., and Wright, J. S. (2018). Influences of Pacific Climate Variability on Decadal Subsurface Ocean Heat Content Variations in the Indian Ocean. *Journal of Climate*, 31(10):4157–4174.
- Kalnay, E., Kanamitsu, M., Kistler, R., Collins, W., Deaven, D., Gandin, L., Iredell, M., Saha, S., White, G., Woollen, J., Zhu, Y., Chelliah, M., Ebisuzaki, W., Higgins, W., Janowiak, J., Mo, K., Ropelweski, C., Wang, J., Leetmaa, A., Reynolds, R., Jenne, R., and Joseph, D. (1996). The NCEP / NCAR 40-Year Reanalysis Project. *Bulletin of the American Meteorological Society*, 77(3):437–472.
- Kao, H. Y. and Yu, J. Y. (2009). Contrasting Eastern-Pacific and Central-Pacific types of ENSO. *Journal of Climate*, 22(3):615–632.
- Killworth, P. D., Chelton, D. B., and De Szoeke, R. A. (1997). The speed of observed and theoretical long extratropical planetary waves. *Journal of Physical Oceanography*, 27(9):1946–1966.
- Kleinherenbrink, M., Riva, R., Frederikse, T., Merrifield, M., and Wada, Y. (2017). Trends and interannual variability of mass and steric sea level in the Tropical Asian Seas. *Journal of Geophysical Research: Oceans*, 122(8):6254–6276.
- Kobayashi, S., Ota, Y., Harada, Y., Ebata, A., Moriya, M., Onoda, H., Onogi, K., Kamahori, H., Kobayashi, C., Endo, H., Miyaoka, K., and Takahashi, K. (2015). The JRA-55 Reanalysis: General Specifications and Basic Characteristics. *Journal of the Meteorological Society of Japan. Ser. II*, 93(1):5–48.
- Köhl, A. and Stammer, D. (2008). Decadal Sea Level Changes in the 50-Year GECCO Ocean Synthesis. *Journal of Climate*, 21:1876–1890.
- Kug, J. S., Jin, F. F., and An, S. I. (2009). Two types of El Niño events: Cold tongue El Niño and warm pool El Niño. *Journal of Climate*, 22(6):1499–1515.
- Large, W. G. and Yeager, S. G. (2004). Diurnal to decadal global forcing for oceans and sea-ice models : the data sets and flux climatologies. Technical report, NCAR, Boulder.

- Large, W. G. and Yeager, S. G. (2009). The global climatology of an interannually varying air-sea flux data set. *Climate Dynamics*, 33:341–364.
- Lee, T. and McPhaden, M. J. (2008). Decadal phase change in large-scale sea level and winds in the Indo-Pacific region at the end of the 20th century. *Geophysical Research Letters*, 35:L01605.
- Lee, T. and McPhaden, M. J. (2010). Increasing intensity of El Niño in the central-equatorial Pacific. *Geophysical Research Letters*, 37:L14603.
- Lidberg, M., Johansson, J. M., Scherneck, H. G., and Davis, J. L. (2007). An improved and extended GPS-derived 3D velocity field of the glacial isostatic adjustment (GIA) in Fennoscandia. *Journal of Geodesy*, 81(3):213–230.
- Liu, Q., Feng, M., and Wang, D. (2011). ENSO-induced interannual variability in the southeastern South China Sea. *Journal of Physical Oceanography*, 67:127–133.
- Liu, Q., Wang, D., Zhou, W., Xie, Q., and Zhang, Y. (2010). Covariation of the Indonesian Throughflow and South China Sea Throughflow Associated with the 1976/77 Regime Shift. *Advances in Atmospheric Sciences*, 27(1):87–94.
- Liu, Q.-Y., Feng, M., Wang, D., and Wijffels, S. (2015). Interannual variability of the Indonesian Throughflow transport: A revisit based on 30 year expendable bathythermograph data. *Journal of Geophysical Research: Oceans*, 120:6405–6418.
- Llovel, W., Becker, M., Cazenave, A., Jevrejeva, S., Alkama, R., Decharme, B., Douville, H., Ablain, M., and Beckley, B. (2011). Terrestrial waters and sea level variations on interannual time scale. *Global and Planetary Change*, 75:76–82.
- Llovel, W., Penduff, T., Meyssignac, B., Molines, J. M., Terray, L., Bessi eres, L., and Barnier, B. (2018). Contributions of Atmospheric Forcing and Chaotic Ocean Variability to Regional Sea Level Trends Over 1993–2015. *Geophysical Research Letters*, 45(24):13,405–13,413.
- Locarnini, R. A., Mishonov, A. V., Baranova, O. K., Boyer, T. P., Zweng, M. M., Garcia, H. E., Reagan, J. R., Seidov, D., Weathers, K. W., Paver, C. R., and Smolyar, I. V. (2019). World Ocean Atlas 2018, Volume 1: Temperature. Technical report, NOAA, Silver Spring.
- Lombard, A., Garric, G., and Penduff, T. (2009). Regional patterns of observed sea level change: Insights from a 1/4° global ocean/sea-ice hindcast. *Ocean Dynamics*, 59(3):433–449.

- Lorbacher, K., Marsland, S. J., Church, J. A., Griffies, S. M., and Stammer, D. (2012). Rapid barotropic sea level rise from ice sheet melting. *Journal of Geophysical Research: Oceans*, 117:C06003.
- Lu, Q., Zuo, J., Li, Y., and Chen, M. (2013). Interannual sea level variability in the tropical Pacific Ocean from 1993 to 2006. *Global and Planetary Change*, 107:70–81.
- Ma, J., Feng, M., Lan, J., and Hu, D. (2020). Projected Future Changes of Meridional Heat Transport and Heat Balance of the Indian Ocean. *Geophysical Research Letters*, 47:e2019GL086803.
- Madec, G., Delecluse, P., Imbard, M., and Levy, C. (1998). OPA 8.1 Ocean General Circulation Model Reference Manual. Technical report.
- Madec, G. and NEMO-team (2016). NEMO Ocean Engine. Technical Report 27, Institut Pierre-Simon Laplace (IPSL), Paris.
- Mantua, N. J. (n.d.). PDO Index. <http://research.jisao.washington.edu/pdo/PDO.latest>. Last access: 08 June 2017.
- McGregor, S., Gupta, A. S., and England, M. H. (2012a). Constraining wind stress products with sea surface height observations and implications for Pacific Ocean sea level trend attribution. *Journal of Climate*, 25(23):8164–9176.
- McGregor, S., Timmermann, A., Schneider, N., Stuecker, M. F., and England, M. H. (2012b). The effect of the south pacific convergence zone on the termination of El Niño events and the meridional asymmetry of ENSO. *Journal of Climate*, 25(16):5566–5586.
- Meng, L., Zhuang, W., Zhang, W., Ditri, A., and Yan, X. H. (2019). Decadal sea level variability in the Pacific Ocean: Origins and climate mode contributions. *Journal of Atmospheric and Oceanic Technology*, 36(4):689–698.
- Merrifield, M. A. (2011). A shift in western tropical Pacific sea level trends during the 1990s. *Journal of Climate*, 24(15):4126–4138.
- Merrifield, M. A. and Maltrud, M. E. (2011). Regional sea level trends due to a Pacific trade wind intensification. *Geophysical Research Letters*, 38:L21605.
- Merrifield, M. A., Thompson, P. R., and Lander, M. (2012). Multidecadal sea level anomalies and trends in the western tropical Pacific. *Geophysical Research Letters*, 39:L3602.

- Meyers, G. (1996). Variation of Indonesian Throughflow and the El Nino-Southern Oscillation. *J. Geophys. Res*, 101(C5):12255–12263.
- Meyssignac, B., Piecuch, C. G., Merchant, C. J., Racault, M., Palanisamy, H., McIntosh, C., Sathyendranath, S., and Brewin, R. (2017). Causes of the Regional Variability in Observed Sea Level, Sea Surface Temperature and Ocean Colour Over the Period 1993 – 2011. *Surveys in Geophysics*, 38:187–215.
- Milne, G. A., Gehrels, W. R., Hughes, C. W., and Tamisiea, M. E. (2009). Identifying the causes of sea-level change. *Nature Geoscience*, 2(7):471–478.
- Mitrovica, J. X., Tamisiea, M. E., Davis, J. L., and Milne, G. A. (2001). Recent mass balance of polar ice sheets inferred from patterns of global sea-level change. *Letters to Nature*, 409:1026–1029.
- Moon, J. H. and Song, Y. T. (2013). Sea level and heat content changes in the western North Pacific. *Journal of Geophysical Research: Oceans*, 118:2014–2022.
- Moon, J. H., Song, Y. T., Bromirski, P. D., and Miller, A. J. (2013). Multidecadal regional sea level shifts in the Pacific over 1958–2008. *Journal of Geophysical Research: Oceans*, 118(12):7024–7035.
- Nan, F., Xue, H., and Yu, F. (2015). Kuroshio intrusion into the South China Sea: A review. *Progress in Oceanography*, 137:314–333.
- Nerem, R. S., Chambers, D. P., Choe, C., and Mitchum, G. T. (2010). Estimating Mean Sea Level Change from the TOPEX and Jason Altimeter Missions. *Marine Geodesy*, 33:435–446.
- NOAA National Geophysical Data Center (n.d.a). Etopo1 1 arc-minute global relief model. <https://www.ncei.noaa.gov/access/metadata/landing-page/bin/iso?id=gov.noaa.ngdc.mgg.dem:316>. Last access: 11 November 2019.
- NOAA National Geophysical Data Center (n.d.b). Etopo2v2 2 arc-minute global relief model. <https://www.ngdc.noaa.gov/mgg/global/relief/ETOP02/ETOP02v2-2006/ETOP02v2g/netCDF/>. Last access: 12 June 2018.
- NOAA/PSL (n.d.). Nino34 index. https://psl.noaa.gov/gcos_wgsp/Timeseries/Data/nino34.long.data. Last access: 07 June 2017.
- Patara, L. and Böning, C. W. (2014). Abyssal ocean warming around Antarctica strengthens the Atlantic overturning circulation. *Geophysical Research Letters*, 41:3972–3978.

- Patara, L., Böning, C. W., and Biastoch, A. (2016). Variability and trends in Southern Ocean eddy activity in 1/12° ocean model simulations. *Geophysical Research Letters*, 43(9):4517–4523.
- Patara, L., Böning, C. W., and Tanhua, T. (2021). Multidecadal changes in southern ocean ventilation since the 1960s driven by wind and buoyancy forcing. *Journal of Climate*, 34(4):1485–1502.
- Pedlosky, J., Pratt, L. J., Spall, M. A., and Helfrich, K. R. (1997). Circulation around islands and ridges. *Journal of Marine Research*, 55(6):1199–1251.
- Peltier, W. (2004). Global Glacial Isostasy and the Surface of the Ice-Age Earth: The ICE-5G (VM2) Model and Grace. *Annual Review of Earth Planet Science*, 32:111–149.
- Penduff, T., Juza, M., Barnier, B., Zika, J., Dewar, W. K., Treguier, A. M., Molines, J. M., and Audiffren, N. (2011). Sea level expression of intrinsic and forced ocean variabilities at interannual time scales. *Journal of Climate*, 24(21):5652–5670.
- Penduff, T., Llovel, W., Close, S., Garcia-Gomez, I., and Leroux, S. (2019). Trends of Coastal Sea Level Between 1993 and 2015: Imprints of Atmospheric Forcing and Oceanic Chaos. *Surveys in Geophysics*, 40(6):1543–1562.
- Peng, D., Palanisamy, H., Cazenave, A., and Meyssignac, B. (2013). Interannual Sea Level Variations in the South China Sea Over 1950–2009. *Marine Geodesy*, 36(2):164–182.
- Permanent Service for Mean Sea Level (n.d.). Revised local reference dataset. <https://psmsl.org/data/obtaining>. Last access: 16 December 2020.
- Piecuch, C. G. and Ponte, R. M. (2011). Mechanisms of interannual steric sea level variability. *Geophysical Research Letters*, 38:L15605.
- Piecuch, C. G. and Ponte, R. M. (2012). Buoyancy-driven interannual sea level changes in the southeast tropical Pacific. *Geophysical Research Letters*, 39:L05607.
- Piecuch, C. G., Thompson, P. R., and Hamlington, B. D. (2019). What Caused Recent Shifts in Tropical Pacific Decadal Sea-Level Trends ? *Journal of Geophysical Research: Oceans*, 124:7575–7590.
- Pohlmann, H., Kröger, J., Greatbatch, R. J., and Müller, W. A. (2017). Initialization shock in decadal hindcasts due to errors in wind stress over the tropical Pacific. *Climate Dynamics*, 49(7):2685–2693.

- Ponte, R. M. (2006). Low-frequency sea level variability and the inverted barometer effect. *Journal of Atmospheric and Oceanic Technology*, 23(4):619–629.
- Ponte, R. M. (2012). An assessment of deep steric height variability over the global ocean. *Geophysical Research Letters*, 39:L04601.
- Ponte, R. M. and Rosen, R. D. (2004). Nonlinear effects of variable winds on ocean stress climatologies. *J. Climate*, 17(6):1283–1293.
- Pugh, D. and Woodworth, P. (2014). *Sea-Level Science: Understanding Tides, Surges, Tsunamis and Mean Sea-Level Changes*. Cambridge University Press.
- Qiu, B. and Chen, S. (2012). Multidecadal Sea Level and Gyre Circulation Variability in the Northwestern Tropical Pacific Ocean. *Journal of Physical Oceanography*, 42(1):193–206.
- Qu, T., Kim, Y. Y., Yaremchuk, M., Tuzuka, T., Ishida, A., and Yamagata, T. (2004). Can Luzon Strait transport play a role in conveying the impact of ENSO to the South China Sea? *Journal of Climate*, 17(18):3644–3657.
- Ray, R. D. and Douglas, B. C. (2011). Experiments in reconstructing twentieth-century sea levels. *Progress in Oceanography*, 91(4):496–515.
- Rieck, J. K., Böning, C. W., and Greatbatch, R. J. (2018). Decadal variability of eddy kinetic energy in the South Pacific subtropical countercurrent in an Ocean General circulation model. *Journal of Physical Oceanography*, 48(4):757–771.
- Rong, Z., Liu, Y., Zong, H., and Cheng, Y. (2007). Interannual sea level variability in the South China Sea and its response to ENSO. *Global and Planetary Change*, 55(4):257–272.
- Roullet, G. and Madec, G. (2000). Salt conservation, free surface, and varying levels: A new formulation for ocean general circulation models. *Journal of Geophysical Research: Oceans*, 105(C10):23927–23942.
- Ryan, S., Ummenhofer, C. C., Gawarkiewicz, G., Wagner, P., Scheinert, M., Biastoch, A., and Böning, C. W. (2021). Depth structure of Ningaloo Niño/Niña events and associated drivers. *Journal of Climate*, 34(5):1767–1788.
- Saji, N. H., Goswami, B. N., Vinayachandran, P. N., and Yamagata, T. (1999). A dipole mode in the tropical Indian Ocean. *Nature*, 401(6751):360–363.
- Scharffenberg, M. G. and Stammer, D. (2010). Seasonal variations of the large-scale geostrophic flow field and eddy kinetic energy inferred from the TOPEX/Poseidon

- and Jason-1 tandem mission data. *Journal of Geophysical Research: Oceans*, 115(2):1–29.
- Schwarzkopf, F. U. (2016). *Ventilation pathways in the tropical Atlantic and Pacific Oceans with a focus on the Oxygen Minimum Zones: development and application of a nested high-resolution global model system*. Dissertation, Christian-Albrechts-Universität zu Kiel.
- Schwarzkopf, F. U., Biastoch, A., Böning, C. W., Chanut, J., Durgadoo, J. V., Getzlaff, K., Harlaß, J., Rieck, J. K., Roth, C., Scheinert, M. M., and Schubert, R. (2019). The INALT family - a set of high-resolution nests for the Agulhas Current system within global NEMO ocean/sea-ice configurations. *Geoscientific Model Development Discussions*, 12(7):3329—3355.
- Schwarzkopf, F. U. and Böning, C. W. (2011). Contribution of Pacific wind stress to multi-decadal variations in upper-ocean heat content and sea level in the tropical south Indian Ocean. *Geophysical Research Letters*, 38:L12602.
- Sen Gupta, A., McGregor, S., Van Sebille, E., Ganachaud, A., Brown, J. N., and Santoso, A. (2016). Future changes to the Indonesian Throughflow and Pacific circulation: The differing role of wind and deep circulation changes. *Geophysical Research Letters*, 43:1669–1678.
- Sérazin, G., Meyssignac, B., Penduff, T., Terray, L., Barnier, B., and Molines, J. M. (2016). Quantifying uncertainties on regional sea level change induced by multi-decadal intrinsic oceanic variability. *Geophysical Research Letters*, 43:8151–8159.
- Sérazin, G., Penduff, T., Grégorio, S., Barnier, B., Molines, J.-M., and Terray, L. (2015). Intrinsic Variability of Sea Level from Global Ocean Simulations: Spatiotemporal Scales. *Journal of Climate*, 28(10):4279–4292.
- Siedler, G., Church, J., and Gould, J. (2001). *Ocean Circulation & Climate*. Academic Press, London.
- Smith-Konter, B. R., Thornton, G. M., and Sandwell, D. T. (2014). Vertical crustal displacement due to interseismic deformation along the San Andreas fault: Constraints from tide gauges. *Geophysical Research Letters*, 41:3793–3801.
- Sprintall, J., Gordon, A. L., Koch-Larrouy, A., Lee, T., Potemra, J. T., Pujiana, K., Wijffels, S. E., and Wij, S. E. (2014). The Indonesian seas and their role in the coupled ocean–climate system. *Nature Geoscience*, 7(7):487–492.
- Stammer, D., Cazenave, A., Ponte, R. M., and Tamisiea, M. E. (2013). Causes for Contemporary Regional Sea Level Changes. *Annual Review of Marine Science*, 5:21–46.

- Stewart, K. D., Kim, W. M., Urakawa, S., Hogg, A. M. C., Yeager, S., Tsujino, H., Nakano, H., Kiss, A. E., and Danabasoglu, G. (2020). JRA55-do-based repeat year forcing datasets for driving ocean–sea-ice models. *Ocean Modelling*, 147:101557.
- Stocker, T., Qin, D., Plattner, G.-K., Tignor, M., Allen, S., Boschung, J., Nauels, A., Xia, Y., Bex, V., and Midgley, P. (2013). IPCC, 2013: Climate Change 2013: The Physical Science Basis. Contribution of Working Group I to the Fifth Assessment Report of the Intergovernmental Panel on Climate Change. Technical report, IPCC, Cambridge, UK and New York, NY.
- Storto, A., Masina, S., Balmaseda, M., Guinehut, S., Xue, Y., Szekely, T., Fukumori, I., Forget, G., Chang, Y. S., Good, S. A., Köhl, A., Vernieres, G., Ferry, N., Peterson, K. A., Behringer, D., Ishii, M., Masuda, S., Fujii, Y., Toyoda, T., Yin, Y., Valdivieso, M., Barnier, B., Boyer, T., Lee, T., Goussien, J., Wang, O., Heimbach, P., Rosati, A., Kovach, R., Hernandez, F., Martin, M. J., Kamachi, M., Kuragano, T., Mogensen, K., Alves, O., Haines, K., and Wang, X. (2017). Steric sea level variability (1993–2010) in an ensemble of ocean reanalyses and objective analyses. *Climate Dynamics*, 49(3):709–729.
- Strassburg, M. W., Hamlington, B. D., Leben, R. R., Manurung, P., Gaol, J. L., Nababan, B., Vignudelli, S., and Kim, K. Y. (2015). Sea level trends in Southeast Asian seas. *Climate of the Past*, 11(5):743–750.
- Sun, C., Feng, M., Matear, R. J., Chamberlain, M. A., Craig, P., Ridgway, K. R., and Schiller, A. (2012). Marine downscaling of a future climate scenario for Australian boundary currents. *Journal of Climate*, 25(8):2947–2962.
- Sun, S. and Thompson, A. F. (2020). Centennial Changes in the Indonesian Through-flow Connected to the Atlantic Meridional Overturning Circulation: The Ocean’s Transient Conveyor Belt. *Geophysical Research Letters*, 47(21):1–9.
- Sun, S., Thompson, A. F., and Eisenman, I. (2020). Transient overturning compensation between Atlantic and Indo-Pacific basins. *Journal of Physical Oceanography*, 50(8):2151–2172.
- Sun, Z., Zhang, Z., Zhao, W., and Tian, J. (2016). Interannual modulation of eddy kinetic energy in the northeastern South China Sea as revealed by an eddy-resolving OGCM. *Journal of Geophysical Research: Oceans*, 121:3190–3201.
- Susanto, R. D. and Tony Song, Y. (2015). Indonesian throughflow proxy from satellite altimeters and gravimeters. *Journal of Geophysical Research: Oceans*, 120:2844–2855.

- Syvitski, J. P., Kettner, A. J., Overeem, I., Hutton, E. W., Hannon, M. T., Brakenridge, G. R., Day, J., Vörösmarty, C., Saito, Y., Giosan, L., and Nicholls, R. J. (2009). Sinking deltas due to human activities. *Nature Geoscience*, 2(10):681–686.
- Tamisiea, M. E. (2011). The Moving boundaries of Sea Level Change. *Oceanography*, 24(2):24–39.
- Thomson, R. and Emery, W. (2014). *Data Analysis Methods in Physical Oceanography*. Elsevier Science, 3 edition.
- Timmermann, A., McGregor, S., and Jin, F. F. (2010). Wind effects on past and future regional sea level trends in the southern Indo-Pacific. *Journal of Climate*, 23(16):4429–4437.
- Tokinaga, H., Xie, S.-P., Timmermann, A., Mcgregor, S., Ogata, T., Kubota, H., and Okumura, Y. M. (2012). Regional Patterns of Tropical Indo-Pacific Climate Change: Evidence of the Walker Circulation Weakening. *Journal of Climate*, 25(5):1689–1710.
- Tomczak, M. and Godfrey, J. S. (2003). *Regional Oceanography: an Introduction*. Daya Publishing House, Delhi, 2 edition.
- Tseng, Y.-h., Lin, H., ching Chen, H., Thompson, K., Bentsen, M., Böning, C. W., Bozec, A., Cassou, C., Chassignet, E., Chow, C. H., Danabasoglu, G., Danilov, S., Farneti, R., Fogli, P. G., Fujii, Y., Griffies, S. M., Ilicak, M., Jung, T., Masina, S., Navarra, A., Patara, L., Samuels, B. L., Scheinert, M., Sidorenko, D., Sui, C. H., Tsujino, H., Valcke, S., Voldoire, A., Wang, Q., and Yeager, S. G. (2016). North and equatorial Pacific Ocean circulation in the CORE-II hindcast simulations. *Ocean Modelling*, 104:143–170.
- Tsujino, H., Urakawa, S., Nakano, H., Small, R. J., Kim, W. M., Yeager, S. G., Danabasoglu, G., Suzuki, T., Bamber, J. L., Bentsen, M., Böning, C. W., Bozec, A., Chassignet, E. P., Curchitser, E., Boeira Dias, F., Durack, P. J., Griffies, S. M., Harada, Y., Ilicak, M., Josey, S. A., Kobayashi, C., Kobayashi, S., Komuro, Y., Large, W. G., Le Sommer, J., Marsland, S. J., Masina, S., Scheinert, M., Tomita, H., Valdivieso, M., and Yamazaki, D. (2018). JRA-55 based surface dataset for driving ocean–sea-ice models (JRA55-do). *Ocean Modelling*, 130:79–139.
- Ummenhofer, C. C., Biastoch, A., and Böning, C. W. (2017). Multidecadal Indian Ocean Variability Linked to the Pacific and Implications for Preconditioning Indian Ocean Dipole Events. *Journal of Climate*, 30(5):1739–1751.

- Ummenhofer, C. C., Ryan, S., England, M. H., Scheinert, M., Wagner, P., Biastoch, A., and Böning, C. W. (2020). Late 20th Century Indian Ocean Heat Content Gain Masked by Wind Forcing. *Geophysical Research Letters*, 47(22):e2020GL088692.
- Ummenhofer, C. C., Schwarzkopf, F. U., Meyers, G., Behrens, E., Biastoch, A., and Böning, C. W. (2013). Pacific ocean contribution to the asymmetry in eastern indian ocean variability. *Journal of Climate*, 26(4):1152–1171.
- Wagner, P. and Böning, C. W. (2021). Decadal sea level variability in the Australasian Mediterranean Sea. *Ocean Science Discussions [preprint]*, in review:1–25.
- Wagner, P., Scheinert, M., and Böning, C. (2021). Contribution of buoyancy fluxes to tropical Pacific sea level variability. *Ocean Science*, 17:1103–1113.
- Wainwright, L., Meyers, G., Wijffels, S., and Pigot, L. (2008). Change in the Indonesian Throughflow with the climatic shift of 1976/77. *Geophysical Research Letters*, 35:L03604.
- Wajsowicz, R. C. (1993). The Circulation of the Depth-integrated Flow around an Island with Application to the Indonesian Throughflow. *Journal of Physical Oceanography*, 23(7):1470–1484.
- Wajsowicz, R. C. (1996). Flow of a western boundary current through multiple straits: an electrical circuit analogy for the Indonesian throughflow and archipelago. *Journal of Geophysical Research*, 101(C5):12295–12300.
- Wang, C., Deser, C., Yu, J.-Y., DiNezio, P., and Clement, A. (2017). El Niño and Southern Oscillation (ENSO): A Review. *Coral Reefs of the Eastern Pacific*, 8:203–250.
- Wang, C. and Fiedler, P. C. (2006). ENSO variability and the eastern tropical Pacific: A review. *Progress in Oceanography*, 69(2-4):239–266.
- Wang, G., Chen, D., and Su, J. (2008). Winter eddy genesis in the eastern South China Sea due to orographic wind jets. *Journal of Physical Oceanography*, 38(3):726–732.
- Wijffels, S. and Meyers, G. (2004). An Intersection of Oceanic Waveguides: Variability in the Indonesian Throughflow Region. *Journal of Physical Oceanography*, 34(5):1232–1253.
- Wild, M., Folini, D., Hakuba, M. Z., Schär, C., Seneviratne, S. I., Kato, S., Rutan, D., Ammann, C., Wood, E. F., and König-Langlo, G. (2015). The energy balance over land and oceans: an assessment based on direct observations and CMIP5 climate models. *Climate Dynamics*, 44:3393–3429.

- Wu, C. R. and Chang, C. W. (2005). Interannual variability of the South China Sea in a data assimilation model. *Geophysical Research Letters*, 32:L17611.
- Xue, P., Malanotte-Rizzoli, P., Wei, J., and Eltahir, E. A. (2020). Coupled Ocean-Atmosphere Modeling Over the Maritime Continent: A Review. *Journal of Geophysical Research: Oceans*, 125:e2019JC014978.
- Yeager, S. and Danabasoglu, G. (2014). The Origins of Late-Twentieth-Century Variations in the Large-Scale North Atlantic Circulation. *Journal of Climate*, 27(9):3222–3247.
- Yeh, S. W., Kug, J. S., Dewitte, B., Kwon, M. H., Kirtman, B. P., and Jin, F. F. (2009). El Nino in a changing climate. *Nature*, 461(7263):511–514.
- Zanna, L., Khatiwala, S., Gregory, J. M., Ison, J., and Heimbach, P. (2019). Global reconstruction of historical ocean heat storage and transport. *Proceedings of the National Academy of Sciences*, 116(4):1126–1131.
- Zhai, X., Johnson, H. L., Marshall, D. P., and Wunsch, C. (2012). On the wind power input to the ocean general circulation. *Journal of Physical Oceanography*, 42(8):1357–1365.
- Zhu, X., Greatbatch, R. J., and Claus, M. (2017). Interannual variability of tropical Pacific sea level from 1993 to 2014. *Journal of Geophysical Research: Oceans*, 122:602–616.
- Zhuang, W., Qiu, B., and Du, Y. (2013). Low-frequency western Pacific Ocean sea level and circulation changes due to the connectivity of the Philippine archipelago. *Journal of Geophysical Research: Oceans*, 118:6759–6773.
- Zweng, M. M., Reagan, J. R., Seidov, D., Boyer, T. P., Antonov, J. I., Locarnini, R. A., Garcia, H. E., Mishonov, A. V., Baranova, O. K., Weathers, K. W., Paver, C. R., and Smolyar, I. V. (2019). World Ocean Atlas 2018, Volume 2: Salinity. Technical Report 82, NOAA, Silver Spring.

Appendix Chapter 3

A

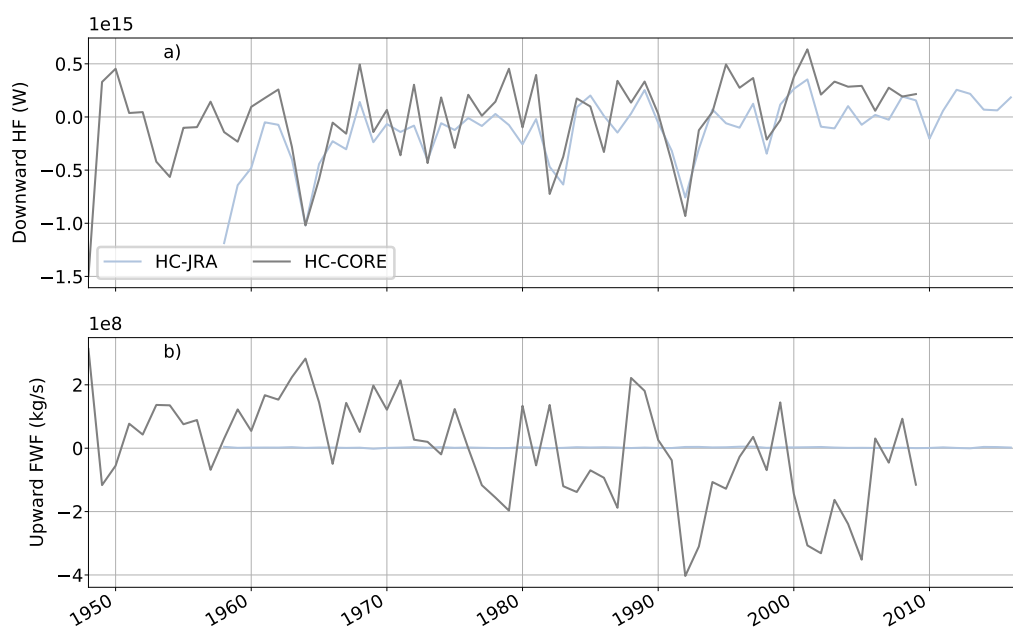


Fig. A.1.: Timeseries of global sum of (a) downward ocean–atmosphere heat flux (HF) and (b) of upward ocean–atmosphere freshwater flux (FWF). All quantities are given for two hindcast experiments.

Appendix Chapter 5

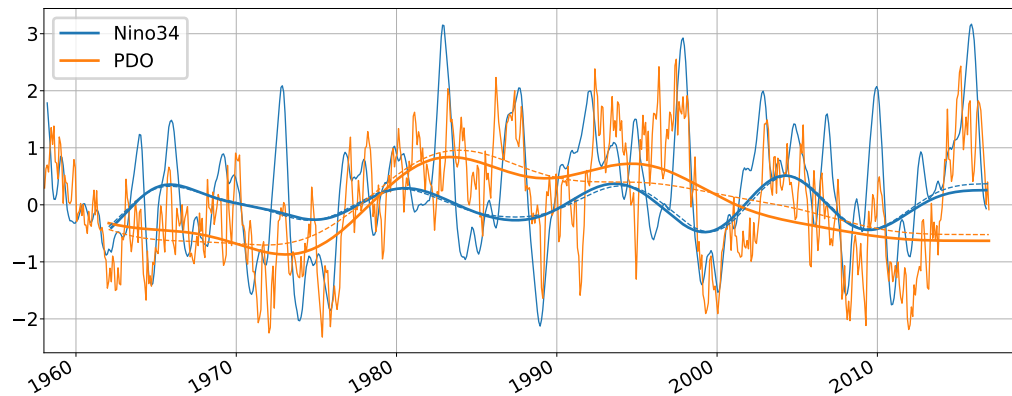


Fig. B.1.: *Niño3.4 and PDO index, both calculated from REF025. Smoothed lines are band pass filtered with cutoff periods of 8 and 13 years (Niño3.4) and low-pass filtered with cutoff periods of 13 years (PDO). Dashed lines show observational estimates.*

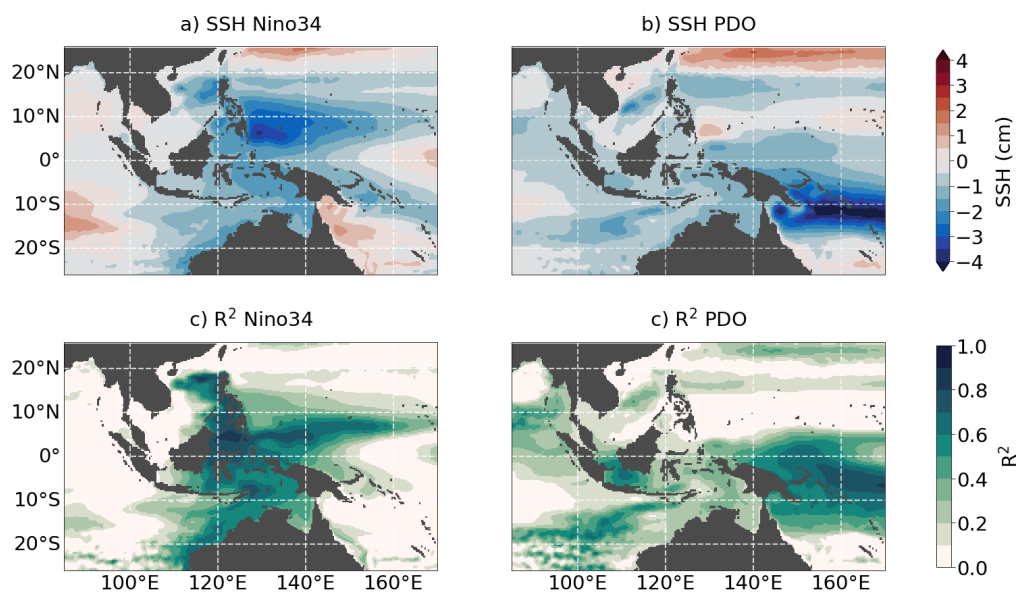


Fig. B.2.: Linear regression of SSH from WIND on (a) Niño3.4 and (b) PDO index and (c, d) respective coefficients of determination. Both climate indices are derived from REF025. All data were filtered with an 8-year low-pass filter.

Acknowledgement

This thesis benefited from the support of many people, whose contribution I gratefully acknowledge. I thank my supervisor Claus W. Böning for giving me the opportunity to be a part of this project, his continued support and many helpful sketches. I thank Arne Biastoch for his guidance and supervision not only during the doctorate. As a member of my ISOS-committee, Johannes Karstensen contributed to this thesis with many helpful remarks during our many meetings that improved my work. Markus Scheinert and Lavinia Patara provided model output from their simulations. I benefitted from the scientific, technical and administrative skills of Franziska Schwarzkopf, Willi Rath, René Schubert, Siren Rühs, Jan-Klaus Rieck, Klaus Getzlaff, Rafael Abel, Torge Martin, Christina Roth, Ioana Ivanciu, Sabine Niewels and Nikole Lorenz. The OD-department at GEOMAR deserves recognition for creating a productive and supportive work environment - even during a global pandemic. I also acknowledge the ISOS program. I am grateful to my family and friends, and especially to Johanna Geritz, for their continued support.

Erklärung

Hiermit erkläre ich, dass ich die vorliegende Dissertation, abgesehen von der Betreuung durch Prof. Dr. Claus W. Böning, Prof. Dr. Arne Biastoch und Dr. Johannes Karstensen nach Inhalt und Form eigenständig und unter Einhaltung der Regeln guter wissenschaftlicher Praxis der Deutschen Forschungsgemeinschaft verfasst habe. Ich habe keine anderen als die angegebenen Hilfsmittel und Quellen verwendet. Diese Dissertation hat weder ganz noch in Teilen an einer anderen Stelle im Rahmen eines Prüfungsverfahrens vorgelegen. Die Dissertation ist eine Mischform zwischen Monografie und kumulativer Dissertation. Kapitel 4 wurde im Ocean Science Journal veröffentlicht. Kapitel 5 wurde im gleichen Journal zur Veröffentlichung eingereicht. Beiträge anderer WissenschaftlerInnen zu diesen beiden Kapiteln habe ich kenntlich gemacht. Mir wurde kein akademischer Grad entzogen.

Kiel, 21.09.2021

Patrick Wagner